Analytical and Numerical Studies of Neutrino Oscillations in Supernovae

A DISSERTATION

SUBMITTED TO THE FACULTY OF THE GRADUATE SCHOOL

OF THE UNIVERSITY OF MINNESOTA

BY

Meng-Ru Wu

IN PARTIAL FULFILLMENT OF THE REQUIREMENTS

FOR THE DEGREE OF

Doctor of Philosophy

Professor Yong-Zhong Qian, Advisor

October, 2012

Acknowledgements

I would like to express my gratitude and acknowledgement to many people who helped and supported me during my PhD study such that this thesis can be accomplished.

Firstly, I would like to thank my advisor Prof. Yong-Zhong Qian, who led me into this field and helped me gradually understand the physical importance of this subject. He could always provide helpful suggestions and advice when I encountered any difficulty or problem, regardless of whether it is research-related or not.

Secondly, I am very grateful to all of my collaborators, Dr. Joe Carlson, Dr. John Cherry, Prof. Huaiyu Duan, Dr. Tobias Fischer, Prof. George Fuller, Lutz Huther, and Prof. Gabriel Martinez-Pinedo, for many fruitful discussions and contributions to the researches that form this thesis.

I would also like to thank Prof. Alexander Heger, Dr. Projjwal Banerjee, Jin Chen, Ken Chen, Chen Hou, Sener Ozonder, and Zhen Yuan for discussing various topics in physics related to this thesis with me. I would also like to thank Prof. Joe Kapusta, Prof. Marvin Marshak, and Prof. Liliya Williams for being my committee members.

Lastly, I would give my deepest gratitude to all of my friend, my parents, and my wife for all the spiritual and physical support they gave me during these years.

Dedication

To my parents, Wen-Yung Wu and Bao-Chu Lee, and my lovely wife, Ya-Iz Jau.

Abstract

Neutrinos are one of the central ingredients in core-collapse supernova explosion and their flavor oscillations in supernovae might affect many processes that occur in this explosive environment. In this thesis, we study neutrino flavor oscillations in supernovae both analytically and numerically. Analytically, we propose a simple model to explain the flavor evolution history in the region of collective neutrino oscillations during the neutronization neutrino burst and accretion phase of neutrino emission with low matter density. We show that the formation of spectral splits induced by collective neutrino oscillations can be well-understood using this model. We also apply this model to discuss the flavor instability of neutrino oscillations that occurs in the cooling phase. Numerically, we simulate neutrino flavor evolution history using the neutrino emission data from a state-of-the-art 18 $M_{\odot}$ supernova model. We discuss the time-dependence of neutrino oscillations on neutrino emission characteristics and the supernova environment. We then study the effect of neutrino oscillations on the nucleosynthesis that occurs in the neutrino-driven wind. At last, we calculate the expected neutrino signals in the IceCube detector and discuss the consequences.

Contents

List of Tables

List of Figures

Chapter 1

Introduction

Stars in the universe shine as a result of burning nuclear fuels in the center to balance the gravity. It starts from burning hydrogen into helium as currently happening in our Sun. After central hydrogen is used up, the star then contracts such that the density and temperature arise accordingly. At some point, the central helium would be ignited to start another nuclear burning stage. This will halt the contraction and the star will continue to shine for another millions of years until the central helium is exhausted. This kind of burning-contraction cycle (see Fig. 1.1) supports the life of the star. How far this cycle can continue depends on the initial mass and metallicity of the star [1, 2]. Typically, a star with mass between roughly 1 $M_\odot$ and 8 $M_\odot$ ends up with a carbon-oxygen core without further carbon ignition. The core will then continuously cool down as a white dwarf supported by the electron degeneracy pressure.

For a star with mass between 8 $M_\odot$ and 10 $M_\odot$, the central temperature will be high enough for carbon burning such that an oxygen-neon-magnesium core is formed. However, the temperature will not be high enough to ignite the neon burning and the core will contract and grow. When the core mass exceeds the Chandrasekhar mass

$$M_{\rm ch} = 5.83 Y_e^2 \left[1 + \left(\frac{s_e}{\pi Y_e}\right)\right] M_\odot, \tag{1.1}$$

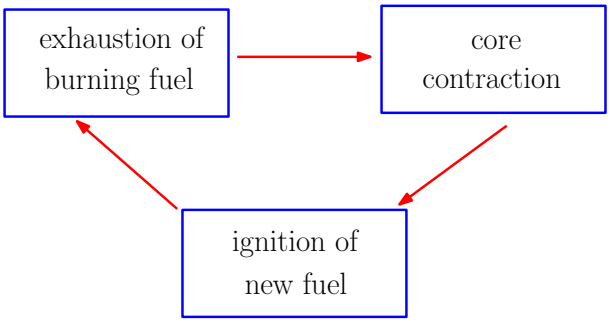

Figure 1.1: Schematic plot of stellar evolution cycle.

where Y_e and s_e are the electron fraction and the entropy of electrons per baryon, the instability triggered by the electron capture on heavy nuclei

$$e^- + (Z, A) \rightarrow (Z - 1, A) + \nu_e, \tag{1.2}$$

where Z and A are ^{24}Mg and ^{22}Ne in this case will result in the gravitational collapse of the core and the subsequent supernova explosion. Stars end up with this type of explosion are the so-called O-Ne-Mg core-collapse supernovae (O-Ne-Mg CCSNe) or electron capture core-collapse supernovae (EC-CCSNe).

For a star with mass between 10 $M_\odot$ and 25 $M_\odot$, the nuclear burning can continue until an iron core is formed. Since iron is the most stable nuclei and no further nuclear energy can be extracted by burning, the iron core will collapse once the core mass grows larger than the corresponding Chandrasekhar mass. For a star with larger mass, the instability is mainly triggered by the photo-disintegration of iron nuclei

$$^{56}\mathrm{Fe} + \gamma \rightarrow 13\,^4\mathrm{He} + 4\mathrm{n} - 124.4\mathrm{MeV}. \tag{1.3}$$

This kind of supernovae is typically called the iron core-collapse supernovae (Fe-CCSNe).

One major difference between the EC-CCSNe and Fe-CCSNe is the thickness of the envelope above the core. For EC-CCSNe, there are only very thin layers of carbon, oxygen and helium shells above the core such that the density drops very quickly around

the radius of $r \sim 10^3$ km. For Fe-CCSNe, there are extended layers above the core and the density gradients are much shallower compared with the O-Ne-Mg CCSNe. This difference leads to very different consequences of the supernova dynamics and explosion mechanism. As seen in most recent numerical simulations [3–5], EC-CCSNe can be successfully exploded in 1D simulation with the "delayed neutrino-heating mechanism" (see Chap. 2) and the results in 1D and multi-D basically agree with each other. However, in the case of the Fe-CCSNe, successful explosions are only derived in the case of multi-dimensional simulations with the aids of fluid-instability and convection (see [6] for a most recent review and the references therein). Asides from that, the large difference of density profiles also results in very different behaviors of neutrino oscillations in these two types of supernovae as will be discussed in Chap. 4 and 5.

Other than the study of the mysterious death of the star itself, supernova explosions play very important roles in many other aspects in astro-physics and cosmology such as the production of heavy elements after the Big Bang, the formation of the first galaxy and the galactic chemical evolution. However, to fully understand the details of supernova explosion, we have to understand the most important ingredient of this process – neutrinos. Why are neutrinos so important in supernova explosion? This is because during the collapse, nearly all ($> 99\%$) the gravitational binding energy,

$$E_G \approx \frac{3GM_{\rm PNS}^2}{5R_{\rm PNS}} \approx 3 \times 10^{53}{\rm ergs}, \tag{1.4}$$

is carried away by different flavors of neutrinos and antineutrinos in the time scale of 10 seconds or so. For comparison, the energy of the photon emitted during the explosion is about $10^{49} - 10^{50}$ ergs and the kinetic energy of the ejecta is about 10^{51} ergs. As we will see in Chap. 2, those neutrinos and antineutrinos have energy about 10 MeV. Thus, one could easily estimate that the total number of neutrinos being emitted is about :

$$N_\nu \approx \frac{E_G}{10{\rm MeV}} \approx 10^{58}. \tag{1.5}$$

This huge numbers of neutrinos can greatly affect the physics of supernovae although they can only weakly interact with surrounding matters. For example, to deliver a

successful explosion, it only requires less than 1% of the neutrino energy being dumped to the material above the proto-neutron star (PNS)!

In addition to exploding the star, those neutrinos and antineutrinos will drive a continuous matter outflow by depositing the energy to the atmosphere of the PNS. This so-called "neutrino-driven wind" has been considered to be one of the possible sites for forming the elements heavier than iron by the rapid-neutron capture process (r-process). Although current supernova simulation do not produce the preferable environment for r-process to occur in the neutrino-driven wind, it remains to be a major source for producing lighter elements, such as Sr, Y, Zr, by other nucleosynthesis processes (see [7] for a review). Furthermore, neutrinos will interact with matters in the outer shells to also induce some other nucleosynthesis processes [8, 9].

As we will see in Chap. 2, neutrinos emitted from PNS have all kinds of flavors : ν_e, ν_μ, ν_τ and their antineutrinos $\bar{\nu}_e$, $\bar{\nu}_\mu$, $\bar{\nu}_\tau$. Based on the recent experiments and observation of reactor, accelerator, solar, and atmospheric neutrinos, it is evident that neutrinos have different mass and flavor eigenstates [10]. The direct consequence is that neutrino oscillations would occur such that neutrinos produced in one flavor can oscillate to other flavors. The detail formalism of neutrino oscillations will be discussed later in Chap. 3. Why would neutrino oscillations be important in supernovae? This is due to two factors. First, neutrinos with different flavors from PNS have different energy spectra :

$$\langle E_{\nu_e} \rangle < \langle E_{\bar{\nu}_e} \rangle < \left\langle E_{\nu_\mu} \right\rangle \approx \langle E_{\bar{\nu}_\nu} \rangle \approx \langle E_{\nu_\tau} \rangle \approx \langle E_{\bar{\nu}_\tau} \rangle \,. \tag{1.6}$$

Second, neutrinos could interact with matters through the weak charge-current (CC) and neutral-current (NC) channels. In the supernova environment, because the temperature is not high enough to have muons and tauons around, ν_μ, ν_τ and their antineutrinos can only interact with matters via NC. For ν_e and $\bar{\nu}_e$, they can interact with matters via both CC and NC. Thus, if any neutrino-induced process aforementioned is sensitive to the CC, then flavor oscillations which change the energy spectra of ν_e and $\bar{\nu}_e$ will

have direct effects on that process.

Aside from the effects on supernova processes and nucleosynthesis, the detection of galactic supernova neutrinos serves as an unique probe for both understanding supernova physics and the unknown neutrino mass hierarchy from the observational point of view [11–13]. However, to decipher the rich underlying physics, we need to understand clearly how neutrino oscillations would affect the signals.

Because its potential importance, neutrino oscillations in supernova has been studied for about thirty years since late 1980's after more evidences of the solar neutrino disappearance [14] and the detection of neutrinos from SN1987A [15, 16]. Although it was realized that both neutrino-electron forward scattering (the so-called Mikheyev-Smirnov-Wolfenstein (MSW) effect [17, 18]) and neutrino-neutrino forward scattering [19–21] along with the vacuum mixing are important in shaping the oscillations, due to the smallness of the 1-3 squared mass difference, most of the focus were paid to mainly the MSW effect. Until the important works [22–24] in 2004 and 2005, people start to realize that the so-called "collective neutrino oscillations" could happen very close to the surface of the PNS due to the non-linear coupling between neutrinos. This novel phenomenon is both analytically and computationally challenging and it leads to a series of subsequent studies (see [25] for a review and [26–46] for recent developments). However, due to the non-linearity of the neutrino-neutrino coupling and the anisotropic nature of neutrino emission, coupled with the dynamically evolving environment of supernovae, it still requires more efforts to fully understand collective neutrino oscillations and its effects on supernova physics.

In this thesis, I will discuss our recent analytical and numerical developments on this topic. The thesis is organized as follows :

- In Chapter 2, I will review the dynamics of supernova explosion and the characteristics of neutrino emission from supernovae.
- In Chapter 3, I will introduce the detailed formalism of neutrino oscillations and

the model that we used to study neutrino oscillations in supernovae.

- In Chapter 4, I will discuss a simple analytical model that we developed to help us understand the physics of collective oscillations in supernovae in different neutrino emission phases.
- In Chapter 5, I will discuss the results of a detailed numerical study of neutrinos oscillations based on the numerical output of a state-of-the-art supernova model.
- In Chapter 6, I will give my conclusion.

Chapter 2

Core-Collapse Supernovae and Neutrinos

From the last seconds of the life of the massive star to the birth of the proto-neutron star, neutrinos play extremely important roles during the evolution and are crucial in many physical processes. In this chapter, we first describe the supernova dynamics very briefly in Sec. 2.1 (please refer to [47] for analytical details and [6] for an updated review). We then discuss the characteristics of neutrino emission for different phases in Sec. 2.2.

2.1 Dynamics of Core-Collapse Supernovae

2.1.1 Gravitational Collapse

After the star uses up its nuclear fuel in the core, the core mass will grow due to the burning in the outer shell. Once the core mass exceeds the Chandrasekhar mass (see equation (1.1)), the electron degenerate pressure can no longer support the gravity such that the gravitational collapse starts. Since the density arises with the contraction, the electron Fermi energy $\mu_e = (3\pi^2 n_e)\hbar c$ increases accordingly such that the electron

capture on nuclei (see equation (1.2)) could occur. Furthermore, the increase of temperature allows the photo-disintegration (see equation (1.3)) to occur when $T \gtrsim 5 \times 10^9$ K. These two processes decrease the electron degenerate pressure and the internal energy very efficiently such that the gravitational collapse is greatly accelerated.

During the collapse, the core can be approximately divided by a boundary where the local infall velocity equals to the sound speed. For the inner core, $v_{\rm infall} \propto r < v_s$ such that it collapse homologously. For the supersonically outer core, it collapses as a quasi-free fall with $v_{\rm infall} \propto 1/\sqrt{r}$.

2.1.2 Neutrino Trapping

During the course of collapse, because of the increase of the density, even neutrinos cannot freely escape when the density reaches $\rho \sim 10^{11} - 10^{12}$ g/cc. This is realized because the neutrino diffusion time scale becomes smaller than the dynamical time scale of the collapse such that an effective neutrino "trapping" occurs. As a result, neutrinos can only slowly diffuse out and one can thus define a neutrino sphere to be where the optical depth equals to 2/3 as a radiation surface for neutrinos. Note that since the cross-section of neutrinos interacting with matters is energy and flavor dependent, the neutrino sphere should also be energy and flavor dependent.

2.1.3 Bounce and Shock

When the inner core reaches the nuclear matter density at the order of 10^{14} g/cc, it bounces as an unit due to the sudden stiffening of the equation of state. The pressure waves pile up at the sonic point between the inner core and outer core. As a result, a discontinuity in density, pressure and velocity is formed as a shockwave. As the shock becomes more and more energetic, it propagates toward the outer part of the core in a very short time scale.

If this shock is energetic enough, it may revert the infall of the outer envelope of the star and successfully deliver the so-called "prompt explosion" firstly proposed in [48].

However, the energy of the shock is generally not high enough such that it is used up by dissociating nuclei to free nucleons and by neutrinos escaping. The shock will thus stall at typically a few hundred kilometers and a standing shock is formed.

2.1.4 Shock Revival and Explosion

Although the shock is temporarily stalled, matter continues to fall on to the newly-formed proton neutron star and release the gravitational energy in the form of neutrinos. Since the neutrino heating efficiency above the neutrino sphere $\dot{q}_{\rm H} \propto r^{-2}$ drops much slower than the neutrino cooling efficiency $\dot{q}_{\rm C} \propto T^6$. Those neutrinos emitted from the neutrino sphere can deposit part of their energy to the region right below the shock. This energy deposition may be able to revive the shock and further explode the entire envelopes of the star as firstly proposed in [49]. This so-called "delayed neutrino-heating" mechanism then remains as the main interest of study of core-collapse supernova explosion for more than four decades. However, due to the numerical difficulties of treating the neutrino transport coupled with the multi-dimensional (multi-D) hydrodynamics, the results have not reached a definite conclusion yet.

In most recent simulations, this mechanism can explode the O-Ne-Mg supernovae without other help [3–5]. For the more massive iron-core supernovae, some groups but not all can successfully blow up the stars by the aids of different mechanisms such as the convection and the fluid instability in multi-D. Beside the neutrino-heating mechanism, other methods such as the inclusion of magneto-hydrodynamics, the development of the acoustic modes, or the QCD phase transition have all recently been considered (see [6] for an updated review).

2.2 Supernova Neutrinos

The neutrino emission during supernova explosion can be roughly divided into four phases : the pre-bounce phase, the neutronization burst, the accretion phase, and the

cooling phase. The time evolution of the energy luminosity L_ν and average energy $\langle E_\nu \rangle$ of neutrinos are shown in Fig. 2.1 for an 18 $M_\odot$ model [5] as an example. It can be summarized as the follows,

- During the pre-bounce and the neutronization phase, the electron capture (equation (1.2)) is the main source of neutrino emission such that $L_{\nu_e} \gg L_{\bar{\nu}_e}, L_{\nu_x}$.
- During the accretion phase, $L_{\nu_e} \approx L_{\bar{\nu}_e} \approx 2 - 3L_{\nu_x}$ due to the separation of the neutrino spheres and the continuous accretion of matters. For the energy, a hierarchy is formed as $\langle E_{\nu_e}(\rangle < \langle E_{\bar{\nu}_e} \rangle < \langle E_{\nu_x} \rangle$.
- During the cooling phase, $L_{\nu_e} \approx L_{\bar{\nu}_e} \lesssim L_{\nu_x}$ and $\langle E_{\nu_e} \rangle < \langle E_{\bar{\nu}_e} \rangle < \langle E_{\nu_x} \rangle$. However, the differences in the average energies of different flavors are gradually decreasing as the PNS cools.

2.2.1 Pre-bounce

During the collapse, the only significant source for producing neutrinos is through the electron capture on nuclei (see Eq. 1.2). The ν_e luminosity and the average energy gradually increase in this period. Neutrinos that are produced before the trapping occurs can basically freely leave the star such that the net lepton number keeps decreasing. However, after trapping, they can only slowly diffuse out and the net lepton number inside the core becomes nearly constant.

2.2.2 Neutronization Burst

When the inner core bounces, a shock is launched such that a high entropy "hot bubble" region in which the nuclei are dissociated into free protons and neutrons is formed behind the shock. In that region, electrons are quickly captured by free protons and produce ν_e. However, before the shock reaches the neutrino sphere, those neutrinos are still trapped and thus trail the shock. Once the shock breaks through the neutrino sphere, those ν_e

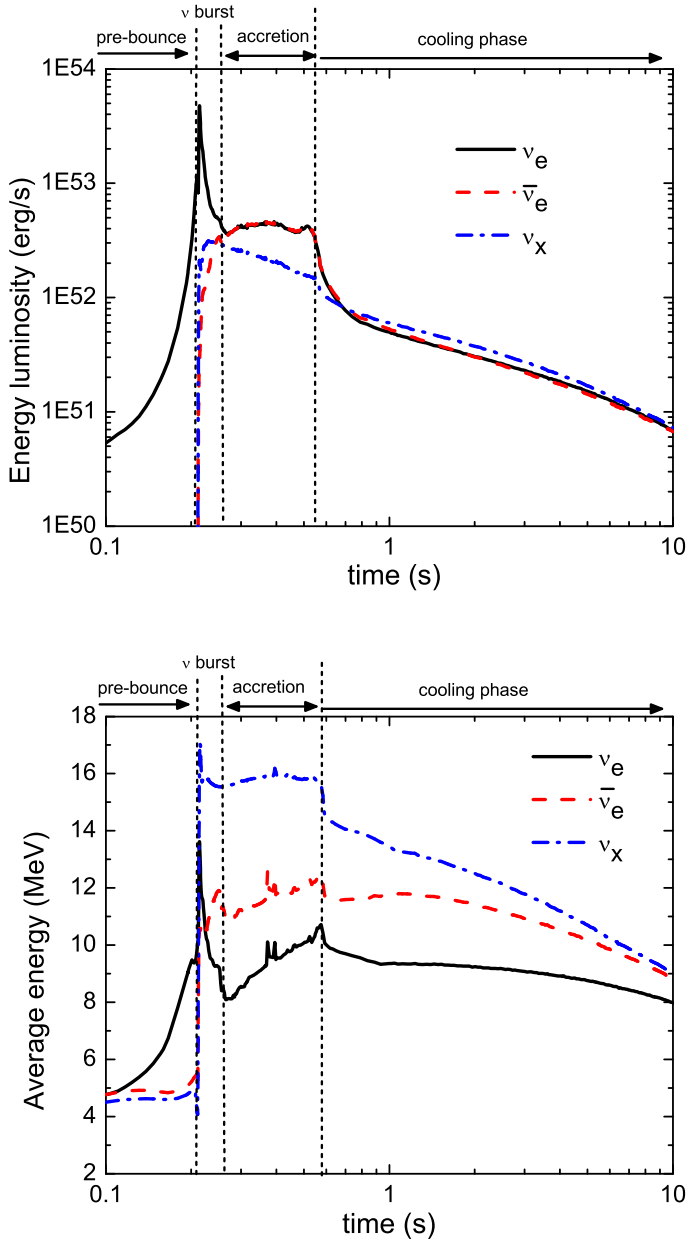

Figure 2.1: Time evolution of neutrino energy luminosity and average energy in an 18 $M_\odot$ supernova model from [5].

which pile up behind the shock can finally freely-escape and produce a ν_e burst. This ν_e burst can reach a peak luminosity of 10^{53} erg/s and can last about the order of several tens milliseconds as shown in Fig. 2.1.

Other than ν_e, other neutrinos species are also produced via the pair annihilation

$$e^+ + e^- \rightarrow \nu + \bar{\nu}, \tag{2.1}$$

and the nucleon-nucleon bremsstrahlung

$$N + N \rightarrow N + N + \nu + \bar{\nu}, \tag{2.2}$$

during this time due to the high temperature caused by the shock. However, their luminosities are much smaller compared to the ν_e luminosity. Besides, since ν_e basically form a degenerate fermi-sea behind the shock before they reach the neutrino sphere, the $\bar{\nu}_e$ production is more suppressed compared to ν_x such that $\bar{\nu}_e$ luminosity arise much slower than ν_x as also shown in Fig. 2.1. We show in Fig. 2.2 the neutrino spectra as an example at $t_{\rm pb} = 0.0047$ millisecond from the 18 $M_\odot$ model in [5].

2.2.3 Accretion Phase

During this period, since the outer layers continue to fall on to the PNS, they supply the gravitational energy for the neutrino emission. The neutrino luminosity here can be estimated by

$$L_\nu \sim \frac{GM_{\rm PNS}\dot{M}}{R_\nu} \sim 40 \times 10^{51} erg/s \left(\frac{M_{PNS}}{1.4M_\odot}\right)\left(\frac{\dot{M}}{0.5M_\odot/s}\right)\left(\frac{50{\rm km}}{R_\nu}\right), \tag{2.3}$$

where $\dot{M}$ is the mass accretion rate, $M_{\rm PNS}$ is the mass of the proto-neutron star, and R_ν is the radius of the neutrino sphere. Also, due to the accretion, the region between the PNS and the shock is in a quasi-stationary state, although the PNS continues to contract slowly.

In this phase, the main sources of producing all different flavors of neutrinos are through the pair-annihilation in equation (2.1) and the nucleon-nucleon bremsstrahlung

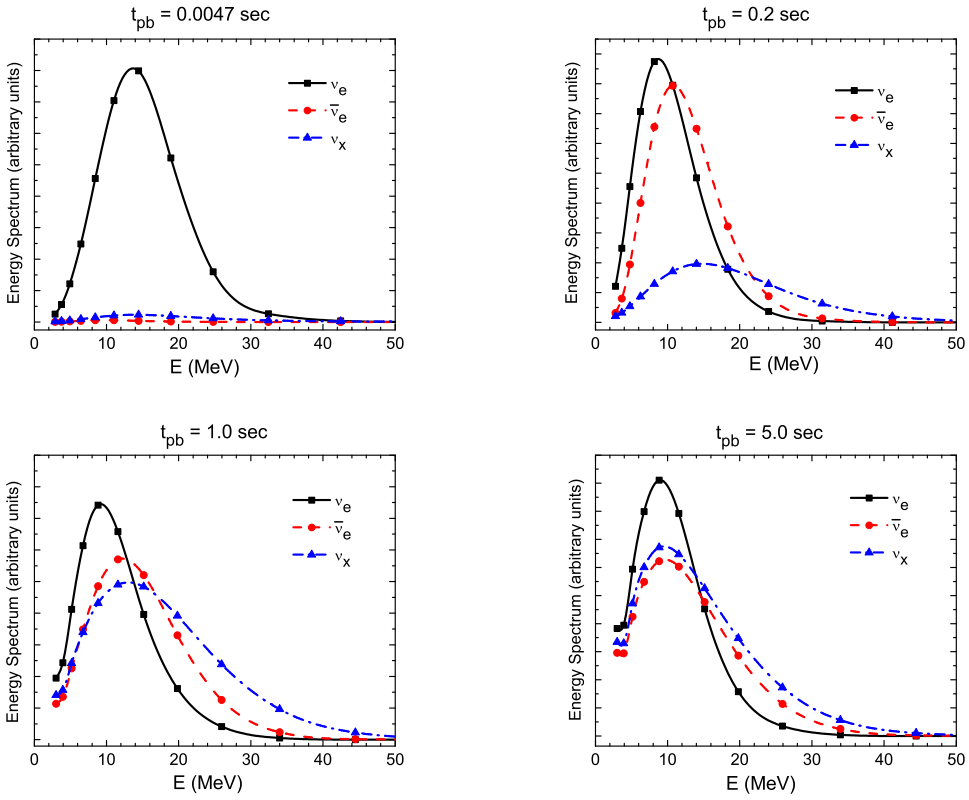

Figure 2.2: Neutrino energy spectra for different emission phases in an 18 $M_\odot$ supernova model from [5].

in equation (2.2). Because of the additional charge current interaction of ν_e and $\bar{\nu}_e$ with the nucleons :

$$\nu_e + n \rightleftharpoons e^- + p, \tag{2.4}$$

$$\bar{\nu}_e + p \rightleftharpoons e^+ + n, \tag{2.5}$$

combined with the flat and quasi-stationary density and temperature profiles above the PNS, the ν_e and $\bar{\nu}_e$ decouple far outside from the ν_x sphere as shown in Fig. 2.3. Also, since the environment is neutron-rich from the electron capture processes happened earlier such that there are more "targets" for ν_e compared to $\bar{\nu}_e$, ν_e decouple further outside compared to $\bar{\nu}_e$. As a result, we have $R_{\nu_e} > R_{\bar{\nu}_e} \gg R_{\nu_x}$ and $T_{R_{\nu_e}} < T_{R_{\bar{\nu}_e}} < T_{R_{\nu_x}}$. Since $\langle E \rangle \propto T$ and $L \propto R^2 T^4$, the energy hierarchy $\langle E_{\nu_e} \rangle < \langle E_{\bar{\nu}_e} \rangle < \langle E_{\nu_x} \rangle$ and the luminosity $L_{\nu_e} \approx L_{\bar{\nu}_e} \approx 2 - 3 L_{\nu_x}$ are derived. Again, We show in Fig. 2.2 the neutrino spectra as an example at $t_{\rm pb} = 0.2$ second.

2.2.4 Cooling Phase

After the shock is revived, the proto-neutron star then cools by itself as neutrinos continue to bring away the energy. Thus, both the neutrino luminosity and average energy decrease with time as shown in Fig. 2.1. During this phase, the density and temperature are much steeper compared to the accretion phase as shown in Fig. 2.3. Thus, the neutrino spheres of different flavors are very close to each other but remain the same ordering $R_{\nu_e} \gtrsim R_{\bar{\nu}_e} \gtrsim R_{\nu_x}$, such that $\langle E_{\nu_e} \rangle < \langle E_{\bar{\nu}_e} \rangle < \langle E_{\nu_x} \rangle$ and $L_{\nu_e} \approx L_{\bar{\nu}_e} \lesssim L_{\nu_x}$.

As the PNS cools off, we see that $\langle E_{\bar{\nu}_e} \rangle$ and $\langle E_{\bar{\nu}_x} \rangle$ become almost the same. This is because at late time, the charge-current interaction is suppressed due to Pauli blocking as the neutrino decoupling shifts to the region with higher density. A detailed analysis can be found in [50]. Once again, we show in Fig. 2.2 the neutrino spectra of both early and late cooling phase at $t_{\rm pb} = 1.0$ and 5.0 seconds for comparison.

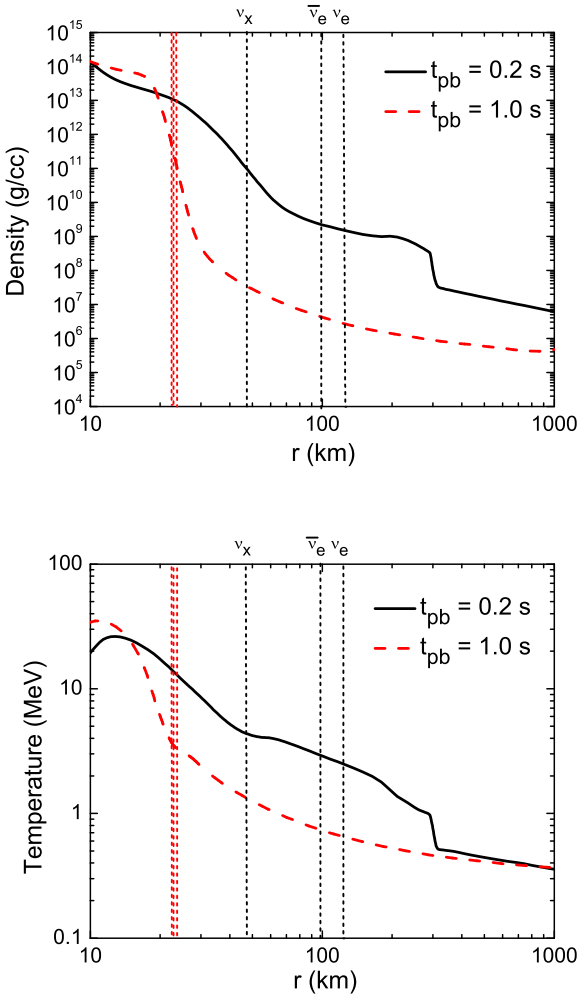

Figure 2.3: Comparison of the density ρ and the temperature T for the accretion phase (black solid lines) and the cooling phase (red dash line) in the 18 $M_\odot$ supernova model from [5]. The vertical dotted lines indicate the neutrino spheres for different flavors.

Chapter 3

Neutrino Oscillations

Recent experiments on solar, atmospheric, reactor and accelerator neutrinos have found strong evidence for neutrino oscillations. Up to date, nearly all mixing parameters for three generations of active neutrinos and antineutrinos have been measured, except for the sign of the atmospheric mass-squared difference and the CP-violating phase [10]. The neutrino mixing matrix can be written as :

$$U = \begin{bmatrix} c_{12}c_{13} & s_{12}c_{13} & s_{13}e^{-i\delta} \\ -s_{12}c_{23} - c_{12}s_{23}s_{13}e^{i\delta} & c_{12}c_{23} - s_{12}s_{23}s_{13}e^{i\delta} & s_{23}c_{13} \\ s_{12}s_{23} - c_{12}c_{23}s_{13}e^{i\delta} & -c_{12}s_{23} - s_{12}c_{23}s_{13}e^{i\delta} & c_{23}c_{13} \end{bmatrix} \times \mathrm{diag}(1, e^{i\frac{\alpha_{21}}{2}}, e^{i\frac{\alpha_{31}}{2}}), \tag{3.1}$$

where $c_{ij} = \cos\theta_{ij}$, $s_{ij} = \sin\theta_{ij}$, the mixing angle $\sin^2 2\theta_{12} = 0.857 \pm 0.024$, $\sin^2 2\theta_{13} = 0.098 \pm 0.013$, $\sin^2 2\theta_{23} > 0.95$ at 90% confidence level. The CP-violating phase δ and two Majorana phases α_{21} and α_{31} are not measured yet. Note that the Majorana phases do not have any physical effect on oscillations because the phases can be absorbed away. The mixing between the neutrino mass eigenstates and flavor eigenstates then follows

$$|\nu_\alpha\rangle = \sum_k U_{\alpha k}|\nu_k\rangle, \tag{3.2}$$

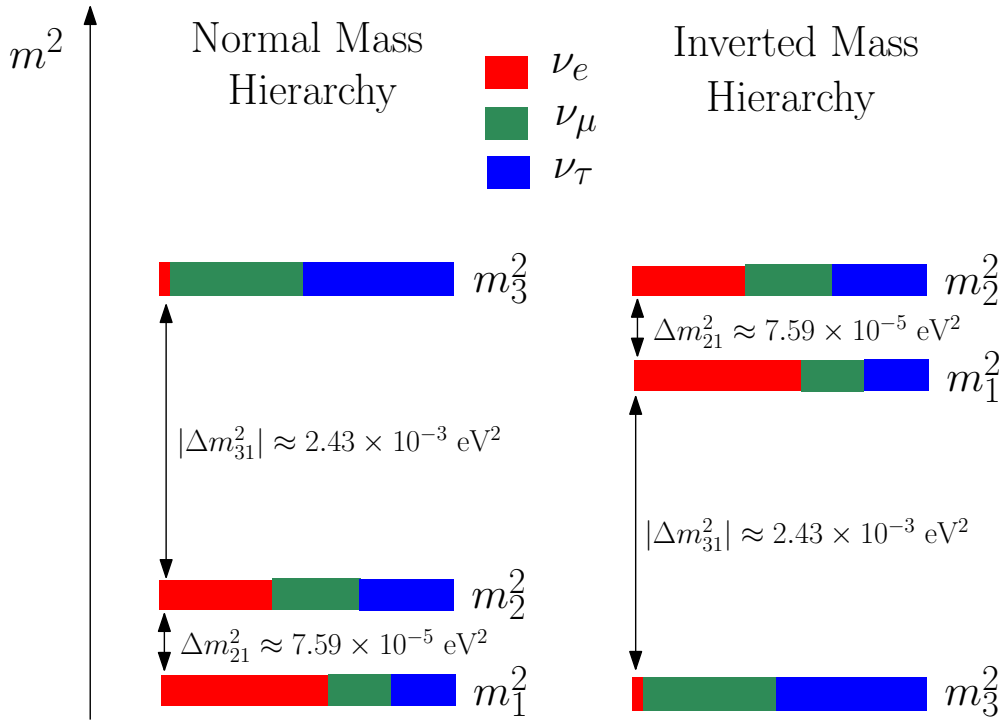

Figure 3.1: Schematic plot for the neutrino mixing. The length of the band of a flavor eigenstate ($|\nu_e\rangle$, $|\nu_\mu\rangle$, or $|\mu_\tau\rangle$) in different mass eigenstates ($|\nu_1\rangle$, $|\nu_2\rangle$, or $|\nu_3\rangle$) indicates the probability of finding it in the corresponding mass eigenstates.

where $\alpha = e, \mu, \tau$ and $k = 1, 2, 3$ for the corresponding flavor and mass eigenstates. The different neutrino mass eigenstates $|\nu_k\rangle$ have different mass eigenvalues m_k. We will see later that the relevant quantities for oscillations are the mass-squared differences $\Delta m^2_{21} = m^2_2 - m^2_1 = (7.50 \pm 0.20) \times 10^{-5}$ eV^2 and $|\Delta m^2_{31}| = |m^2_3 - m^2_1| \approx |\Delta m^2_{32}| = (2.32^{+0.12}_{-0.08}) \times 10^{-3}$ eV^2. The sign of Δm^2_{31} has not been experimentally decided yet. It is thus called the normal mass hierarchy (NH) if $\Delta m^2_{31} > 0$ and inverted mass hierarchy (IH) if $\Delta m^2_{31} < 0$. The pictorial representation of the neutrino mixing is shown in Fig. 3.1.

3.1 Vacuum Oscillations

When neutrinos with momentum p travel in vacuum, the time evolution of a mass eigenstate $|\nu_i\rangle$ simply follow the Schrodinger equation :

$$|\nu_i\rangle_t = e^{-iE_i t}|\nu_i\rangle_0 = e^{-i\sqrt{p^2+m_i^2}t}|\nu_i\rangle_0. \tag{3.3}$$

However, neutrinos are produced through the weak interaction and will be in the flavor eigenstate at the production, which is a linear combination of the mass eigenstates. Since different mass eigenstates evolves differently in time as shown in equation (3.3), a neutrino will thus oscillate among different flavors!

Writing the neutrino flavor wavefunction $|\nu\rangle = \sum_\alpha a^*_\alpha |\nu_\alpha\rangle$ and using equation (3.1) and (3.3), it is straightforward to show that the evolution of the neutrino flavor wavefunction is governed by

$$i\frac{d}{dt}\begin{bmatrix} a_e \\ a_\mu \\ a_\tau \end{bmatrix} = U \begin{bmatrix} \frac{m_1^2}{2p} & 0 & 0 \\ 0 & \frac{m_2^2}{2p} & 0 \\ 0 & 0 & \frac{m_3^2}{2p} \end{bmatrix} U^\dagger \begin{bmatrix} a_e \\ a_\mu \\ a_\tau \end{bmatrix}. \tag{3.4}$$

Note that in the above equation, we omit the terms proportional to the identity matrix because they only add an overall phase to the flavor wavefunction and will not have any observational effect.

In supernova environment, since the energy spectra of ν_μ, ν_τ and their antineutrinos are almost the same. We can thus rotate away the 2-3 mixing by defining the flavor eigenstates

$$\begin{bmatrix} |\nu_e\rangle \\ |\nu_x\rangle \\ |\nu_y\rangle \end{bmatrix} = \begin{bmatrix} 1 & 0 & 0 \\ 0 & \cos\theta_{23} & \sin\theta_{23} \\ 0 & -\sin\theta_{23} & \cos\theta_{23} \end{bmatrix} \begin{bmatrix} |\nu_e\rangle \\ |\nu_\mu\rangle \\ |\nu_\tau\rangle \end{bmatrix}. \tag{3.5}$$

Combining equation (3.4) and equation (3.5), it is straightforward to show that the vacuum Hamiltonian in the e, x, y space is approximately

$$H_{\rm v} \approx \frac{\Delta m^2_{31}}{4E} \begin{bmatrix} -\cos 2\theta_{13} & 0 & \sin 2\theta_{13} \\ 0 & 1 & 0 \\ \sin 2\theta_{13} & 0 & \cos 2\theta_{13} \end{bmatrix} + \frac{\Delta m^2_{21}}{4E} \begin{bmatrix} -\cos 2\theta_{12} & \sin 2\theta_{12} & 0 \\ \sin 2\theta_{12} & \cos 2\theta_{12} & 0 \\ 0 & 0 & 1 \end{bmatrix}, \tag{3.6}$$

where we disregard the terms in the order of $O(\sin 2\theta_{13} \times \frac{\Delta m^2_{21}}{\Delta m^2_{31}})$. It is thus obvious to see that due to the mass hierarchy, the neutrino oscillations can be treated by two subsequent effective two-flavor mixing that occurs in the atmosphere and solar scale respectively!

Assuming the two-flavor mixing scenario, one can easily show that for a neutrino as an electron flavor initially, the probability for it to be detected as an electron neutrino (survival probability) is

$$P_{ee} = |a_{ee}|^2 = 1 - \sin^2\theta_{\rm v} \sin^2\left(\frac{\Delta m^2}{4E} t\right), \tag{3.7}$$

and the probability for it to be detected as another type of neutrino with flavor x (conversion probability) is

$$P_{ex} = |a_{ex}|^2 = \sin^2\theta_{\rm v} \sin^2\left(\frac{\Delta m^2}{4E} t\right), \tag{3.8}$$

where $\theta_{\rm v}$ and Δm^2 are the vacuum mixing angle and the mass-squared difference in the two-flavor mixing scenario.

Other than the above algebraic form of vacuum oscillations, it has been shown that neutrino oscillations in two-flavor mixing scenario can be understood geometrically by

projecting the 2D complex flavor basis to the corresponding 3D real space [51, 52]. It is achieved by expanding the vacuum Hamiltonian matrix in terms of the Pauli matrices :

$$H_{\rm v} = \frac{\Delta m^2}{4E} \begin{bmatrix} -\cos 2\theta_{\rm v} & \sin 2\theta_{\rm v} \\ \sin 2\theta_{\rm v} & \cos 2\theta_{\rm v} \end{bmatrix} = -\omega \frac{\boldsymbol{\sigma}}{2} \cdot \mathbf{H}_{\rm v}, \tag{3.9}$$

where $\omega = \frac{\Delta m^2}{2E}$, $\boldsymbol{\sigma} = (\sigma_x, \sigma_y, \sigma_z)$ and $\mathbf{H}_{\rm v} = (-\sin 2\theta_{\rm v}, 0, \cos 2\theta_{\rm v})$ in the flavor basis. The Hamiltonian written in this form clearly represents the "energy" of a spin in an "external magnetic field". We can thus further define the neutrino flavor isospin (NFIS)[1] [24] as

$$\mathbf{s}_\nu = \langle \nu | \frac{\boldsymbol{\sigma}}{2} | \nu \rangle = \frac{1}{2} \begin{bmatrix} 2{\rm Re}(a_e^* a_x) \\ 2{\rm Im}(a_e^* a_x) \\ |a_e|^2 - |a_x|^2 \end{bmatrix}. \tag{3.10}$$

The time evolution of the NFIS $\mathbf{s}_\nu$ is then given by

$$\frac{d\mathbf{s}_\nu}{dt} = \omega \mathbf{s}_\nu \times \mathbf{H}_{\rm v}. \tag{3.11}$$

This geometric representation tells us that the neutrino NFIS $\mathbf{s}_\nu$ will precess around the vacuum field $\mathbf{H}_{\rm v}$ with the frequency ω, which represents the characteristic frequency of vacuum neutrino oscillations. The survival/conversion probability can be easily derived by projecting the NFIS $\mathbf{s}_\nu$ back to the flavor z-axis as shown in Fig. 3.2.

For antineutrinos, we can similarly define the NFIS as

$$\mathbf{s}_{\bar\nu} = \langle \bar\nu | \frac{\sigma_y \boldsymbol{\sigma} \sigma_y}{2} | \bar\nu \rangle = -\frac{1}{2} \begin{bmatrix} 2{\rm Re}(a_{\bar e} a_{\bar x}^*) \\ 2{\rm Im}(a_{\bar e} a_{\bar x}^*) \\ |a_{\bar e}|^2 - |a_{\bar x}|^2 \end{bmatrix}, \tag{3.12}$$

which is then governed by

$$\frac{d\mathbf{s}_{\bar\nu}}{dt} = -\omega \mathbf{s}_{\bar\nu} \times \mathbf{H}_{\rm v} \tag{3.13}$$

[1] The NFIS defined in [24] and the polarization vectors that are more commonly seen in the literature as in [52] are essentially the same physical quantity. For a detailed discussion, please see the review paper [25].

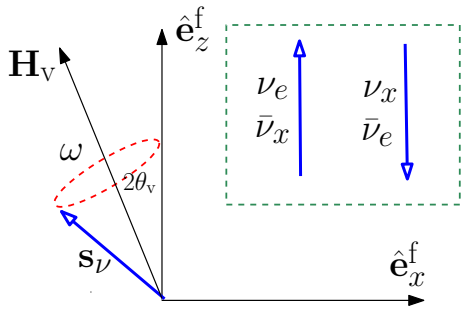

Figure 3.2: Geometric representation of vacuum oscillations in NFIS notation. The direction of a neutrino $\mathbf{s}_\nu$ in the pure flavor eigenstates is parallel to the flavor axis $\hat{\mathbf{e}}_z^{\rm f}$ as indicated in the green box. A neutrino $\mathbf{s}_\nu$ generally rotates around the vacuum Hamiltonian $\mathbf{H}_{\rm v}$ with the frequency $\omega = \Delta m^2/2E$. The projection in the $\hat{\mathbf{e}}_z^{\rm f}$ represents the probability of finding this neutrino in the flavor eigenstates.

in vacuum. In section 3.3, we will see that this definition allows us to treat the neutrinos and antineutrinos in equal footing when we discuss the neutrino-neutrino self-interaction term. Also, for the sake of simplicity, we re-define $\omega = -\frac{\Delta m^2}{2E}$ for antineutrinos to absorb the minus sign in equation (3.12) and drop the subscript ν and $\bar{\nu}$ for $\mathbf{s}$.

Furthermore, in the case of 1-3 mixing, we follow the convention in [24] to re-define the basis such that $\Delta m^2 = |\Delta m^2_{13}| > 0$ is always positive for both NH and IH. In this definition, the mixing angle $0 < \theta_{\rm v} < \pi/4$ remains for the NH. However, we extend $\pi/4 < \theta_{\rm v} < \pi/2$ for the IH, in which the experimental measured value corresponds to $\tilde{\theta}_{\rm v} \equiv \pi/2 - \theta_{\rm v}$.

3.2 MSW Oscillations

In the interior of stars, neutrinos travel through medium which contains nuclei, nucleons and electrons. Although in most of the environment, neutrinos free-stream without any collision and absorption with the medium, the flavor evolution history of neutrinos are affected by the coherent forward scattering of neutrinos with matters [17, 18]. For example, the effective Hamiltonian that is due to the charge current interaction between

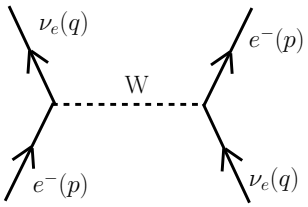

Figure 3.3: Feynman diagram for the MSW Hamiltonian. Note that only this charge current interaction have physical effects on neutrino oscillations because the neutral current interaction contribute equally to ν_e and ν_x.

ν_e and electrons is (see Fig. 3.3 for the corresponding Feynman diagram) :

$$H_{\text{eff}}^{\text{CC}} = \frac{G_F}{\sqrt{2}}[\bar{\nu}_{e,L}\gamma_\mu e_L][\bar{e}_L\gamma^\mu \nu_{e,L}], \tag{3.14}$$

where $\nu_{e,L}$ and e_L here are the corresponding field operators for electron neutrinos and electrons. One can then derive the energy shift from this Hamiltonian by averaging over the initial and final states of neutrinos and electrons to be :

$$V_{\text{MSW}} = \sqrt{2}G_F n_e, \tag{3.15}$$

where n_e is the number density of the electrons that is assumed at rest.

One can similarly calculate the energy shifts caused by the forwarding scattering of neutrinos with electrons, protons and neutrons by the neutral current. However, the energy shifts caused by the neutral current are the same for all flavors and have no observable effect for neutrino oscillations among active neutrinos. Thus, the Hamiltonian matrix for neutrinos from the medium in the two-flavor mixing scenario is :

$$H_e = \frac{\sqrt{2}G_F n_e}{2}\begin{bmatrix} 1 & 0 \\ 0 & -1 \end{bmatrix} = -\frac{\boldsymbol{\sigma}}{2}\cdot \mathbf{H}_e, \tag{3.16}$$

where $\mathbf{H}_e = (0, 0, -\sqrt{2}G_F n_e)$ in the flavor basis. For antineutrinos, it can be shown that $H_e \to -H_e$ but $\mathbf{H}_e$ remains the same under the definition of (3.12).

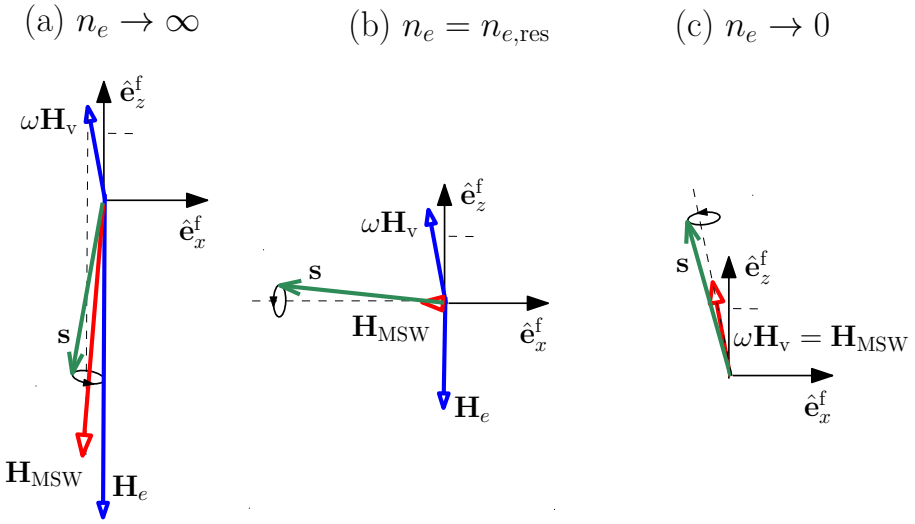

Figure 3.4: Schematic plots for adiabatic MSW flavor conversion. The direction of an NFIS s_ν would follow the change of the direction of $\mathbf{H}_\mathrm{MSW}$ as the electron number density n_e slowly decreases from high density limit (panel (a)), through the MSW resonance (panel (b)), to the vacuum limit (panel (c)).

The flavor evolution of neutrinos and antineutrinos in the presence of electrons in the NFIS representation is thus governed by :

$$\frac{d\mathbf{s}}{dt} = \mathbf{s} \times (\omega\mathbf{H}_\mathrm{v} + \mathbf{H}_e) = \mathbf{s} \times \mathbf{H}_\mathrm{MSW}. \tag{3.17}$$

The MSW flavor transformation can be understood very easily under the geometrical representation as follows.

Assuming in NH with a tiny mixing angle $\theta_\mathrm{v} \ll 1$, $\mathbf{H}_\mathrm{v} \approx \hat{\mathbf{e}}_z^\mathrm{f}$ and $\mathbf{H}_e = -\sqrt{2}G_F n_e \hat{\mathbf{e}}_z^\mathrm{f}$. When the neutrinos are produced deep inside the star where the density is very large such that $|\mathbf{H}_e| \gg |\omega\mathbf{H}_\mathrm{v}|$, $\mathbf{H}_\mathrm{MSW} \approx \mathbf{H}_e$. Thus, an initial $\mathbf{s}$ (ν_e or ν_x) will be almost anti-aligned or aligned with $\mathbf{H}_\mathrm{MSW}$ as shown in Fig. 3.4-(a). At vacuum region or when $\mathbf{H}_e \ll \omega\mathbf{H}_\mathrm{v}$, $\mathbf{H}_\mathrm{MSW} \approx \mathbf{H}_\mathrm{v}$ which points opposite to its initial direction (see Fig. 3.4-(c)). Thus, if n_e decreases slow enough such that $\mathbf{s}$ remains its alignment with $\mathbf{H}_\mathrm{MSW}$, an initial ν_e or ν_x will then be completely converted to another flavor!

But how slow is "slow"? Since $\mathbf{s}$ precesses around $\mathbf{H}_{\rm MSW}$ with the frequency $|\mathbf{H}_{\rm MSW}|$ while $\mathbf{H}_{\rm MSW}$ is changing, the "slowness" or "adiabaticity" can be quantitatively defined by :

$$\left|\frac{d(\mathbf{H}_{\rm MSW}/|\mathbf{H}_{\rm MSW}|)}{dt}\right| = \frac{|\dot{\mathbf{H}}_{\rm MSW}\times\mathbf{H}_{\rm MSW}|}{|\mathbf{H}_{\rm MSW}|^2} \ll |\mathbf{H}_{\rm MSW}|. \tag{3.18}$$

This means that the flavor evolution is adiabatic if the time scale of the density changing is much longer than the period for $\mathbf{s}$ to precess around $\mathbf{H}_{\rm MSW}$. This criterion is typically most stringent when $|\mathbf{H}_{\rm MSW}|$ is smallest. This happens when the flavor eigenstates and the local mass eigenstates are maximally mixed, i.e. $\hat{\mathbf{e}}^{\rm f}_z$ is perpendicular to $\mathbf{H}_{\rm MSW}$ (see Fig. 3.4-(b)) such that

$$\omega\cos\theta_{\rm v} = \sqrt{2}G_F n_e. \tag{3.19}$$

When this condition occurs, it is called the MSW resonance. It is also straightforward to verify that equations (3.18) and (3.19) give the adiabaticity condition that is typically seen when discussing the MSW resonance.

Note that the MSW resonance will never occur for $\bar{\nu}_e$ in NH and for ν_e in IH because the z-component of the $\mathbf{H}_{\rm MSW}$ never vanishes. Thus, for adiabatic evolution, it is always either the entire ν_e or $\bar{\nu}_e$ spectrum is swapped with the other flavor if they are produced in the region with very high n_e such as in the case of supernovae. However, we will see in the next section that the inclusion of neutrino-neutrino coupling will greatly change this consequence.

3.3 Collective Oscillations

In the presence of high neutrino fluxes such as in the early universe or in supernovae, coherent forward scattering between neutrinos also contribute to the oscillations similarly to the MSW effect via the Hamiltonian :

$$H^{\rm NC}_{\nu\nu} = \frac{G_F}{\sqrt{2}}\left[\sum_\alpha \bar{\nu}_{\alpha,L}\gamma_\mu\nu_{\alpha,L}\right]\left[\sum_\beta \bar{\nu}_{\beta,L}\gamma^\mu\nu_{\beta,L}\right], \tag{3.20}$$

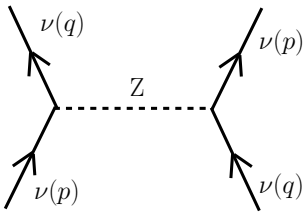

Figure 3.5: Feynman diagram for the Hamiltonian of neutrino-neutrino interaction.

where the subscript α and β stand for different neutrino flavors. It can be shown that the contribution of neutrinos with momentum $\mathbf{q}$ to the Hamiltonian seen by neutrinos with momentum $\mathbf{p}$ in the flavor evolution equation is :

$$H_{\nu\nu}(\mathbf{q}) = \sqrt{2}G_F(1-\cos\theta_{\mathbf{pq}})n_\nu(\mathbf{q})\left\{|a_e(\mathbf{q})|^2 + |a_x(\mathbf{q})|^2 + \begin{bmatrix} |a_e(\mathbf{q})|^2 & a_e(\mathbf{q})a_x^*(\mathbf{q}) \\ a_e^*(\mathbf{q})a_x(\mathbf{q}) & |a_x(\mathbf{q})|^2 \end{bmatrix}\right\}, \tag{3.21}$$

where $\theta_{\mathbf{pq}}$ is the angle between neutrinos with momentum $\mathbf{p}$ and $\mathbf{q}$. Both the diagonal and off-diagonal terms in equation (3.21) come from the Feynman diagrams shown in Fig. 3.5 mediated by Z-boson exchange which is flavor blind. Disregarding the terms proportional to the identity matrix, in NFIS notation,

$$H_{\nu\nu}(\mathbf{q}) = \frac{\boldsymbol{\sigma}}{2}\cdot 2\sqrt{2}G_F(1-\cos\theta_{\mathbf{pq}})n_\nu(\mathbf{q})\mathbf{s}(\mathbf{q}). \tag{3.22}$$

One can similarly show that antineutrinos contribute in exactly the same form as neutrinos in this NFIS notation. Thus, the evolution of $\mathbf{s_p}$ in the supernova environment is then governed by :

$$\frac{d\mathbf{s_p}}{dt} = \mathbf{s_p}\times\left[\omega\mathbf{H}_{\rm v} + \mathbf{H}_e - 2\sqrt{2}G_F\int dn_\nu(\mathbf{q})(1-\cos\theta_{\mathbf{pq}})\mathbf{s_q}\right]. \tag{3.23}$$

For our study of neutrino oscillations in supernovae, we use the so-called "bulb" model [53] which assumes :

1. Supernova environment is spherically symmetric.

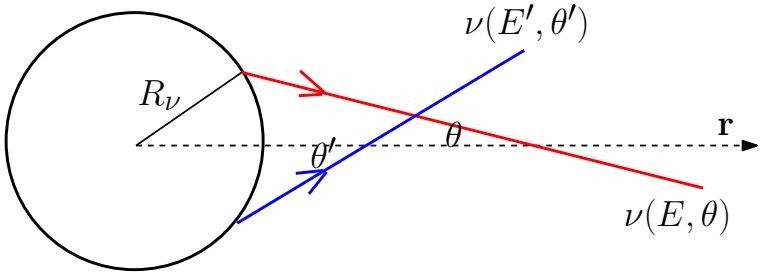

Figure 3.6: The "bulb" model for supernova neutrinos. The flavor evolution history of a neutrino $\mathbf{s}(E, \theta)$ couples to the flavor evolution history of other neutrinos $\mathbf{s}(E', \theta')$, where θ is the angle between the radial direction and the direction of neutrino propagation.

2. All neutrinos are emitted from a sharp neutrino sphere at a radius R_ν.

3. All neutrinos are in pure flavor eigenstates at the neutrino sphere.

4. No absorption, emission and scattering other than the coherent forward scattering outside the neutrino sphere.

In this "bulb" model with two-flavor mixing scenario, we can re-write equation (3.23) for neutrinos/antineutrinos with initial flavor $\nu_\alpha \in \{\nu_e, \bar{\nu}_e, \nu_x, \bar{\nu}_x\}$ as a function of the neutrino energy E and the propagation angle θ with respect to the radial direction (see Fig. 3.6) as :

$$\frac{d\mathbf{s}_{\nu_\alpha}(E, \theta, t)}{dt} = \mathbf{s}_{\nu_\alpha}(E, \theta, t) \times [\omega(E)\mathbf{H}_{\rm v} + \mathbf{H}_e(t) + \mathbf{H}_{\nu\nu}(\theta, t)]\,, \tag{3.24}$$

with

$$\mathbf{H}_{\nu\nu} = -2\sqrt{2}G_F \sum_\beta \frac{L_{\nu_\beta}}{2\pi R_\nu^2 \langle E_{\nu_\beta}\rangle} \int d\cos\theta' dE' (1 - \cos\theta\cos\theta') f_{\nu_\beta}(E', \theta')\mathbf{s}_{\nu_\beta}(E', \theta'), \tag{3.25}$$

where L_{ν_β} is the energy luminosity, $\langle E_{\nu_\beta}\rangle$ is the average energy, and f_{ν_β} is the normalized neutrino number distribution function.

Numerically, we solve equation (3.24) that evolves in terms of the radius r instead of time t. We also write $\mathbf{s}$ as a function of E and $u = \cos^2\theta_0$, where θ_0 is the zenith

angle at the neutrino sphere for emitted neutrinos. One can show that equation (3.24) becomes :

$$\frac{d\mathbf{s}_{\nu_\alpha}(E,u,r)}{dr} = \mathbf{s}_{\nu_\alpha}(E,u,r) \times \left[\frac{\omega(E)\mathbf{H}_{\rm v} + \mathbf{H}_e(r)}{D(u,r)} + \mathbf{H}'_{\nu\nu}(u,r)\right], \tag{3.26}$$

with

$$\mathbf{H}'_{\nu\nu}(u,r) = -\sqrt{2}G_F \sum_\beta \frac{L_{\nu_\beta}}{2\pi r^2 \langle E_{\nu_\beta}\rangle} \int du' dE' \left(\frac{1}{D(u,r)D(u',r)} - 1\right) f_{\nu_\beta}(E',u')\mathbf{s}_{\nu_\beta}(E',u',r), \tag{3.27}$$

where $D(u,r) = \sqrt{1 - \frac{R_\nu^2}{r^2}(1-u)}$.

Since the flavor evolution history of neutrinos with different emission angles is different, solving equation (3.26) has traditionally been called the "multi-angle" simulation/approximation. Due to the non-linear neutrino-neutrino coupling term and the strong angle dependence in $\mathbf{H}_{\nu\nu}(u,r)$, it can only be solved exactly by supercomputing.

However, as we will see in the next chapter, in some cases where multi-angle effect is small or secondary, we can approximately assume that the flavor evolution history is independent of the angle u, i.e. $\mathbf{s}_{\nu_\alpha}(E,u,r) = \mathbf{s}_{\nu_\alpha}(E,r)|_{u=u_0}$, where u_0 is usually taken to be 1 or 1/2. Using this so-called "single-angle" approximation with $u_0 = 1$ and integrating over u', equation (3.24) can be simplified to be :

$$\frac{d\mathbf{s}_{\nu_\alpha}(E,r)}{dr} = \mathbf{s}_{\nu_\alpha}(E,r) \times \left[\omega(E)\mathbf{H}_{\rm v} + \mathbf{H}_e(r) - \sum_\beta \mu_{\nu_\beta}(r) \int dE' \bar{f}_{\nu_\beta}(E')\mathbf{s}_{\nu_\beta}(E',r)\right], \tag{3.28}$$

where $\mu_{\nu_\alpha}(r) = \frac{2\sqrt{2}G_F L_{\nu_\alpha}}{4\pi R_\nu^2 \langle E_{\nu_\alpha}\rangle}[1 - \sqrt{1-(R_\nu/r)^2}]^2$.

From equation (3.28), it is easy to see that the initial ν_e and ν_x (also for $\bar{\nu}_e$ and $\bar{\nu}_x$) have exactly the same Hamiltonian except for that they initially point at opposite direction. Thus, we further define the effective neutrino spectra:

$$g(\omega) = \frac{\delta m^2}{2\omega^2} \times \begin{cases} c_e \bar{f}_{\nu_e}(E) - c_x \bar{f}_{\nu_x}(E), & \text{for neutrinos with } \omega > 0, \\ c_{\bar{e}} \bar{f}_{\bar{\nu}_e}(E) - c_{\bar{x}} \bar{f}_{\bar{\nu}_x}(E), & \text{for antineutrinos with } \omega < 0, \end{cases} \tag{3.29}$$

with $c_\alpha = \mu_{\nu_\alpha}(R_\nu)/\mu_{\nu_e}(R_\nu)$, such that

$$\frac{d\mathbf{s}_\omega}{dr} = \mathbf{s}_\omega \times \left[\omega \mathbf{H}_{\rm v} - \lambda(r)\hat{\mathbf{e}}_z^{\rm f} - \mu(r)\int_{-\infty}^{\infty} d\omega' g(\omega')\mathbf{s}_{\omega'}\right], \tag{3.30}$$

where $\lambda(r) \equiv \sqrt{2}G_F n_e(r)$ and $\mu(r) = \mu_{\nu_e}(r)$.

The collective behavior of neutrino oscillations can be illustrated in the high density limit where $\mu \gg \{\omega, \lambda\}$ is constant. In this limit,

$$\frac{d\mathbf{s}_\omega}{dr} \approx -\mathbf{s}_\omega \times \mu \int_{-\infty}^{\infty} d\omega' g(\omega')\mathbf{s}_{\omega'} = -\mathbf{s}_\omega \times \mu\mathbf{S}, \tag{3.31}$$

where $\mathbf{S} \equiv \int_{-\infty}^{\infty} d\omega g(\omega)\mathbf{s}_\omega$ is the spectrum-weighted sum of all NFIS's. It is clear that in this limit all $\mathbf{s}_\omega$ precess around $\mathbf{S}$ with the same frequency $|\mu\mathbf{S}|$. The evolution of $\mathbf{S}$ is then governed by

$$\frac{d\mathbf{S}}{dr} = \int_{-\infty}^{\infty} d\omega g(\omega)\mathbf{s}_\omega \omega \times \mathbf{H}_{\rm v} + \mathbf{S} \times \mathbf{H}_e. \tag{3.32}$$

Since the time scale for $\mathbf{s}_\omega$ to precess around $\mathbf{S}$ is much shorter than the time scale of the motion of $\mathbf{S}$, in equation (3.32), $\mathbf{s}_\omega$ can be approximately treated by its projection on $\mathbf{S}$ as the time-average over the longer time scale. Equation (3.32) then becomes

$$\frac{d\mathbf{S}}{dr} \approx \mathbf{S} \times (\langle\omega\rangle \mathbf{H}_{\rm v} + \mathbf{H}_e), \tag{3.33}$$

where $\langle\omega\rangle = \int d\omega\omega g(\omega)\mathbf{s}_\omega \cdot \mathbf{S}/|\mathbf{S}|^2$ which is often called the "synchronized" frequency. This is because in this high density limit, $\mathbf{s}_\omega$ and $\mathbf{S}$ almost align with each other and thus co-rotate around $\mathbf{H}_{\rm v}$ with the synchronized frequency $\langle\omega\rangle$ in the case of pure neutrino gas.

However, in the real environment where $\mu(r)$ is changing from $\mu \gg \{\omega, \lambda\}$ to $\mu \to 0$, we have to know how this collective behavior could be maintained and when it breaks down. We will see in the next chapter for several cases in which the single-angle approximation provides simple physical understanding of the complicated non-linear system. Although we note again that this single-angle approximation may not be a good approximation for all system as will be discussed in Chapter 5.

Chapter 4

Analytical Studies of Collective Neutrino Oscillations in Supernovae

As previous mentioned in Chap. 1 and 2, core-collapse supernovae signify the death of massive stars heavier than roughly 8 solar masses and release their gravitational potential energy by about 10^{58} neutrinos. Those large number of neutrinos play very important roles in various processes that occur during the explosion, such as the revival of the stalled shock [6], the formation of heavy elements in the neutrino-driven wind [7], and the neutrino-induced nucleosynthesis in C-O or He shell [8, 9]. In addition, current and planned neutrino detectors are able to detect a large number of events sufficient for detailed statistical analysis when a supernova occurs in the Galaxy [12, 13]. Such neutrino signals provide a unique probe of both exploring the physics of supernovae and the unknown neutrino mass hierarchy [11].

To understand the effects of neutrinos on those processes and to decipher the rich underlying physics from the supernova neutrino signals, we need to understand how neutrinos decouple from the neutron star and how their characteristics are affected by

propagation and flavor evolution through the supernova. This is a not only analytically but also computationally daunting task as it requires detailed supernova modeling and careful treatment of neutrino oscillations.

Recent studies of neutrino oscillations in supernovae suggest that collective oscillations would occur within a few hundred kilometers above the proto-neutron star due to the coherent neutrino-neutrino forward scattering that is discussed in chapter 3. The most distinct feature of collective oscillations is the formation of spectral splits/swaps such that ν_e and/or $\bar{\nu}_e$ swap part of their spectra with ν_μ, ν_τ and $\bar{\nu}_\mu$, $\bar{\nu}_\tau$ with higher energies [35, 38, 53–55].

In this chapter, we discuss our analytical model which provides simple physical understanding of collective neutrino oscillations in supernovae for several different phases of neutrino emission. This "'zeroth-order mean field" approximation is a further simplification from the single-angle approximation discussed in last chapter to reduce the numbers of degree of freedom of the complicated system. We first show in section 4.1 that this approach provides a very simple understanding of collective neutrino oscillations that occurs during the neutronization burst phase of O-Ne-Mg supernovae. In section 4.2, we use similar approach to discuss the collective neutrino oscillations for neutrino spectra that are dominated by ν_e and $\bar{\nu}_e$ compared to ν_x. This kind of neutrino spectra is similar to the spectra emitted during the accretion phase. In section 4.3, we discuss that a complete different oscillation behavior that would occur for typical neutrino emission spectra in the cooling phase and the limitation of the analytical approach.

4.1 Neutrino Oscillations in the Neutronization Burst of O-Ne-Mg Supernovae

As discussed in section 2.2, the ν_e flux dominates the fluxes of $\bar{\nu}_e$ and ν_x such that $\bar{\nu}_e$ and ν_x play little role in neutrino oscillations during the neutronization burst [34]. Thus,

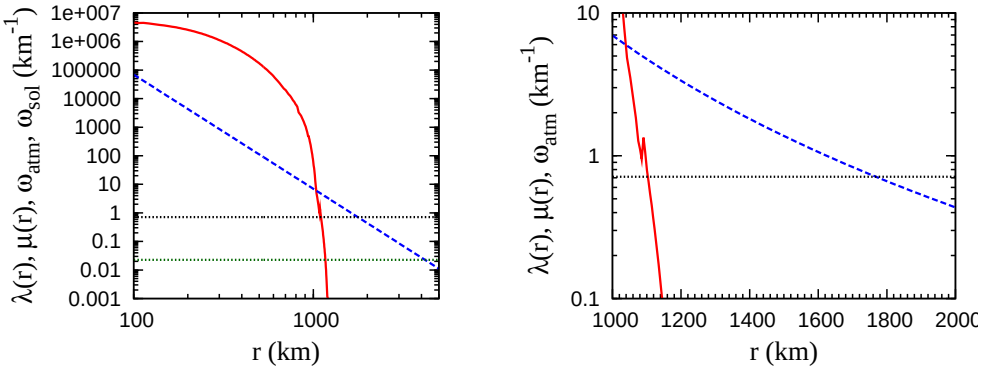

Figure 4.1: Density profiles $\lambda(r)$ (red solid line), $\mu(r)$ (blue dash line), $\omega_{\rm atm}$ (black dotted line), and $\omega_{\rm sol}$ (green dotted line) during the neutronization burst of the O-Ne-Mg supernovae as functions of r. Note tht $\lambda(r)$ has a large density gradient near the MSW resonance regions which happen before $\mu(r) = \omega_{\rm atm}$ or $\mu(r) = \omega_{\rm sol}$.

we completely ignore the emission of $\bar{\nu}_e$ and ν_x in this section. For the neutronization burst, we assume that ν_e are emitted from a neutrino sphere at $R_\nu = 60$ km with a total energy luminosity of $L_{\nu_e} = 10^{53}$ erg/s and a normalized spectrum

$$f_\nu(E) = \frac{1}{F_2(\eta_\nu)T_\nu^3}\frac{E^2}{\exp(E/T_\nu - \eta_\nu)+1}, \tag{4.1}$$

where $\eta_\nu = 3$ and $T_\nu = 2.75$ MeV [corresponding to an average ν_e energy $\langle E_\nu\rangle = F_3(\eta_\nu)T_\nu/F_2(\eta_\nu) = 11$ MeV at emission]. Here

$$F_n(\eta) = \int_0^\infty \frac{x^n}{\exp(x-\eta)+1}dx. \tag{4.2}$$

For the profile of electron density, we use $n_e(r) = \rho(r)Y_e(r)N_A$ from [56,57], where ρ is the baryon density, Y_e is the electron fraction, and N_A is the Avogadro's number. We show both $\lambda(r)$ and $\mu(r)$ in Fig. 4.1. One can see that the electron density drops steeply above the core around $r \approx 1000$ km compare to $\mu(r)$. Also, $\lambda(r)$ becomes comparable to $\omega_{\rm atm}$ and $\omega_{\rm sol}$ before $\mu(r)$ does. Here $\omega_{\rm atm}$ and $\omega_{\rm sol}$ are the vacuum frequencies calculated using $\Delta m^2_{\rm atm}$ and $\Delta m^2_{\rm sol}$ for a neutrino with $E = 8.53$ MeV. These two facts have great influences to the collective neutrino oscillations as will be discussed below.

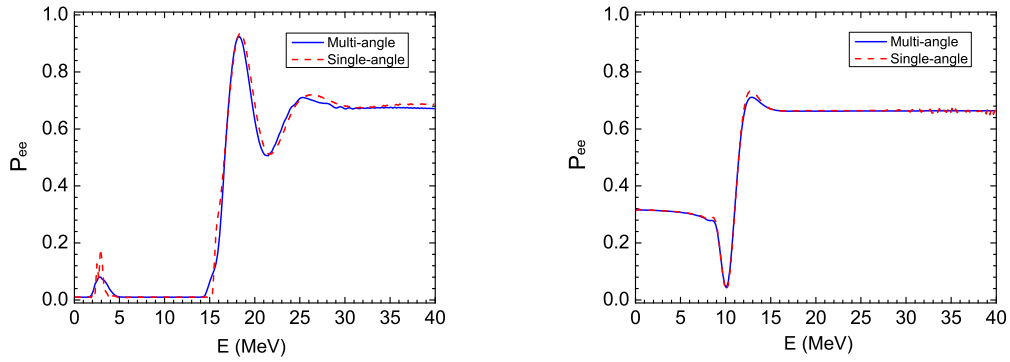

Figure 4.2: Final survival probability P_{ee} in the neutronization burst of the O-Ne-Mg supernovae as a function of the neutrino energy for the NH (left panel) and IH (right panel). The blue solid lines represent the results in multi-angle approximation and the red dash lines represent the results in the corresponding single-angle approximation.

Note that there is a bump in $\lambda(r)$ around $r = 1100$ km which is due to the Y_e jump from the helium layer to the hydrogen layer.

4.1.1 Spectral Splits

In Fig. 4.2, we compare the survival probability P_{ee} at $r = 5000$ km where only vacuum oscillations is operating in both the multi-angle and single-angle approximation in the three-flavor mixing scheme for both NH and IH. It shows that in both hierarchies, the final survival probabilities of low energy ν_e are smaller than the high energy ones, and there exists a sharp transition in both cases. It's also clear that the single-angle approximation well represents the multi-angle treatment here.

In Fig. 4.3, we further show that the probabilities of finding a neutrino in three mass eigenstates P_{e1}, P_{e2}, and P_{e3} at $r = 5000$ km. In these figures, the "spectral split" which represents a sharp transition in the probability/spectra is clearly shown. For example, there are two spectral splits in NH such that ν_e with $E \lesssim 15$ MeV are mostly in the m_3 eigenstate except for a few centered around 3 MeV, ν_e with $E \gtrsim 19$ MeV are all in m_1

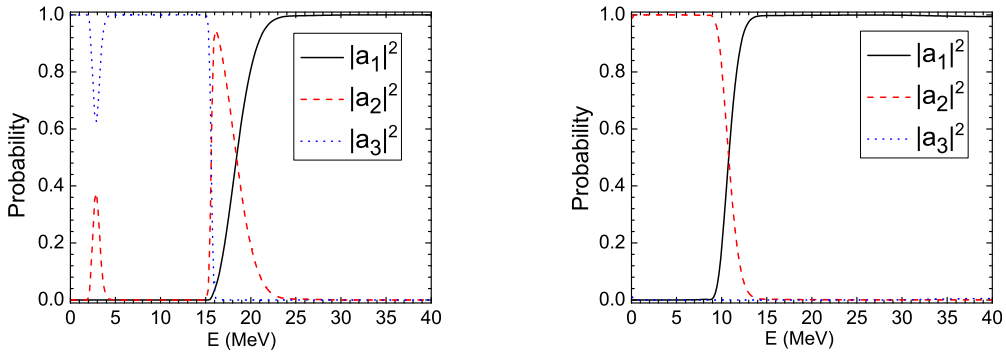

Figure 4.3: The probabilitiy $P_{ei} = |a_i|^2$ for normal mass hierarchy (left panel) and inverted mass hierarchy (right panel) as functions of the neutrino energy. There are two spectral splits in NH at $E \approx 15$ and 19 MeV, and one spectral split in IH at $E \approx 15$ MeV.

state, and ν_e with $15 \lesssim E \lesssim 19$ MeV are in m_2 state. In IH there is only one split such that ν_e with $E \gtrsim 11$ MeV are all in m_1 state and ν_e with $E \lesssim 11$ MeV are in m_2 state. In Fig. 4.4, we show how these probabilities evolve with radius and it clearly shows that the splits are formed hierarchically in two different mass splitting scales with two-flavor mixing in each. Therefore, we can use the NFIS formalism that is introduced in section 3.3 to discuss the formation of the spectral splits.

4.1.2 Zeroth-order Mean Field Approximation

Under single-angle approximation in the two-flavor mixing scenario, we need to solve the non-linear equation (3.30) for all $\mathbf{s}_\omega$ simultaneously to know the neutrino flavor evolution history as a function of r. However, since the ν_e spectrum is centered in a finite range of ω and all $\mathbf{s}_\omega$ essentially align with $\mathbf{S}$ at the high density limit, we

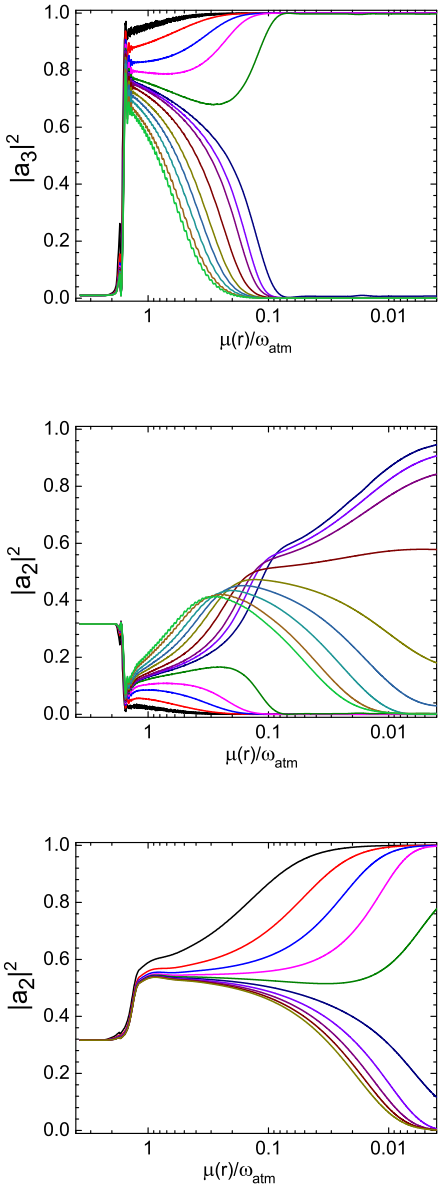

Figure 4.4: The flavor evolution history of $|a_3|^2$ in NH (upper panel), $|a_2|^2$ in NH (middle panel), and $|a_2|^2$ in IH (bottom panel) for different energies. The upper lines represent the flavor evolution history of neutrinos with lower energies. The hierarchical formation of spectral splits is clearly shown at two different scales.

approximate $g(\omega) \approx \delta(\omega - \langle\omega\rangle^{(0)})$, where $\langle\omega\rangle^{(0)} \approx \int \omega g(\omega) d\omega$, such that the zeroth-order mean field $\mathbf{S}^{(0)}$ can be obtained from

$$\frac{d\mathbf{S}^{(0)}}{dr} = \mathbf{S}^{(0)} \times (\langle\omega\rangle^{(0)}\mathbf{H}_{\rm v} + \mathbf{H}_e) \equiv \mathbf{S}^{(0)} \times \mathbf{H}^{(0)}_{\rm MSW}. \tag{4.3}$$

The evolution of $\mathbf{S}^{(0)}$ is the same as that of a ν_e with $E_{\rm MSW} = \delta m^2/2\langle\omega\rangle^{(0)} = 8.53$ MeV undergoing the usual MSW effect as discussed in section 3.2. Now we can approximately solve the evolution of $\mathbf{s}_\omega$ from

$$\frac{d}{dr}\mathbf{s}_\omega \approx \mathbf{s}_\omega \times \left[\omega\mathbf{H}_{\rm v} + \mathbf{H}_e - \mu(r)\mathbf{S}^{(0)}\right]. \tag{4.4}$$

As the heavy mass eigenstate essentially coincides with ν_e at high densities but the light mass eigenstate is predominantly ν_e at low densities, the survival probability of an initial ν_e is approximately $1 - P_{\rm H}$, where $P_{\rm H}$ is the probability for remaining in the heavy mass eigenstate. The probability $1-P_{\rm H}$ calculated from equations (4.3) and (4.4) as a function of $1/E$ for $\Delta m^2 = \Delta m^2_{31}$ and $\theta_{\rm v} = 0.1$ is shown as the dashed curve in Fig. 4.5. For comparison, we show the results calculated from equation (3.30) as the solid curve. Besides, we also show the flavor evolution of $\mathbf{S}$ and $\mathbf{S}^{(0)}$ as a function of r. It can be seen that the zeroth-order mean field $\mathbf{S}^{(0)}$ indeed captures the qualitative features of the single-angle approximation.

In a formal approach, we can use $\mathbf{S}^{(0)}$ as the zeroth-order approximation for $\mathbf{S}$ to solve equation (3.30) for the evolution of $\mathbf{s}^{(0)}_\omega$. We can then sum over $\mathbf{s}^{(0)}_\omega$ to get the next order approximation $\mathbf{S}^{(1)}$. This procedure may be recursively repeated until successive approximations for $\mathbf{S}$ converge. While this approach does not save numerical efforts compared with solving equation (3.30) directly, it motivates an analytic study based on the zeroth-order mean field $\mathbf{S}^{(0)}$, especially when $\mathbf{S}^{(0)}$ can be understood easily.

If the MSW flavor evolution of $\mathbf{S}^{(0)}$ is adiabatic, it will simply follow the change of direction of $\mathbf{H}_{\rm MSW}$ such that the corresponding ν_e being transformed to ν_x almost completely when $n_e \to 0$ as discussed in section 3.2. However, as shown in Fig. 4.5, $\mathbf{S}^{(0)}$ goes through the MSW resonance non-adiabatically due to the rapid-decreasing n_e such

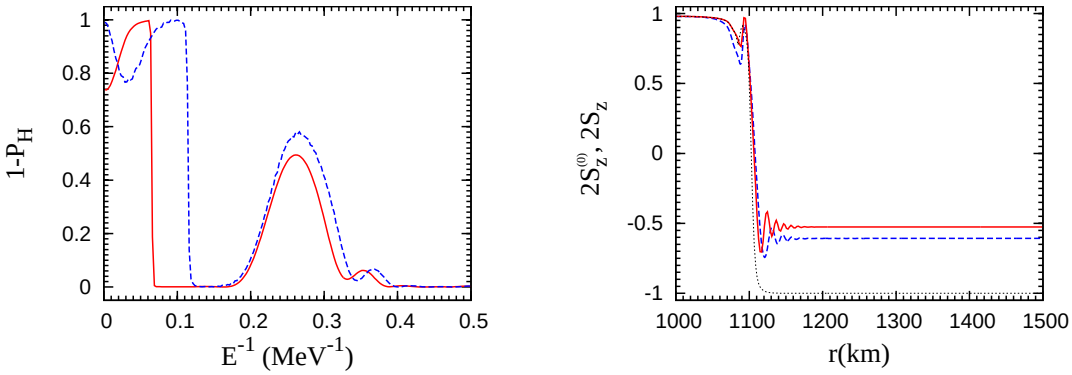

Figure 4.5: The spectral split (left panel) and flavor evolution of **S** (right panel) in O-Ne-Mg neutronization burst under the two-flavor mixing scneario. The single-angle results are shown in red solid lines and the zeroth-order mean field results are shown in blue dash lines. In the left panel, the spectral split is shown by $1 - P_{\rm H}$ as a function of E^{-1}, where $P_{\rm H}$ is the probability for a neutrino to stay in the heavier mass eigenstate. In the right panel, we show $2S_z$ and $2S_z^{(0)}$ as functions of r. In addition, we also show $H^{(0)}_{\rm MSW,z}/|\mathbf{H}^{(0)}_{\rm mSW}|$ in the right panel.

that a substantial component of $\mathbf{S}^{(0)}$ perpendicular to $\mathbf{H}_{\rm v}$ is left after the resonance. This $\mathbf{S}^{(0)}_{\perp}$ component then precesses around $\mathbf{H}_{\rm v}$ with the "vacuum" frequency $\langle\omega\rangle^{(0)}$.

For the individual $\mathbf{s}_\omega$ that follows equation (4.4), before the MSW resonance of $\mathbf{S}^{(0)}$, we can define the "MSW-like" resonance of individual $\mathbf{s}_\omega$ from equation (4.4) by

$$\omega_{\rm res}(r) = \frac{\lambda(r) + \mu(r) S^{(0)}_{z,f}}{\cos 2\theta_{\rm v}}, \tag{4.5}$$

$$\gamma_{\rm res}(r) = \frac{|\mathbf{H}_{{\rm tot},\omega_{\rm res}}(r)|^3}{|\dot{\mathbf{H}}_{{\rm tot},\omega_{\rm res}}(r) \times \mathbf{H}_{{\rm tot},\omega_{\rm res}}(r)|}, \tag{4.6}$$

where $\mathbf{H}_{{\rm tot},\omega} \equiv \omega \mathbf{H}_{\rm v} - \lambda(r)\hat{\mathbf{e}}^f_z - \mu(r)\mathbf{S}^{(0)}$.

We show both $\omega_{\rm res}(r)$ and $\gamma_{\rm res}(r)$ as functions of r in Fig. 4.6. It clearly shows that those neutrinos with $0.2 \lesssim 2\omega/\delta m^2 \lesssim 0.3$ MeV^{-1} go through the resonance non-adiabatically (see Fig. 4.5) around $r = 1094$ km where the highest peak of $1/\gamma_{\rm res}$ in Fig. 4.6 occurs due to the small bump in the n_e profile. Other neutrinos with $2\omega/\delta m^2 \lesssim$

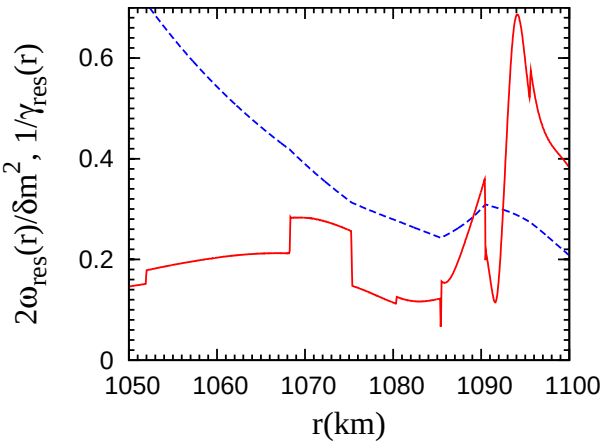

Figure 4.6: $\omega_{\rm res}$ and $\gamma_{\rm res}$ of low energy neutrinos that go through the MSW-like resonance as functions of r.

0.2 MeV^{-1} and $2\omega/\delta m^2 \gtrsim 0.3$ MeV^{-1}, that go through the resonance before the MSW resonance of $\mathbf{S}^{(0)}$ around $r = 1100$ km, all evolve adiabatically and are thus completely converted to ν_x.

After $\mathbf{S}^{(0)}$ goes through the MSW resonance and precesses around $\mathbf{H}_{\rm v}$, equation (4.5) is no longer valid because of the rotation of $\mathbf{S}^{(0)}_{\perp}$. How the rotation of $\mathbf{S}^{(0)}_{\perp}$ changes the resonance condition can be easily understood by introducing the "co-rotating" frame, in which $\mathbf{S}^{(0)}_{\perp}$ simply sits at the $\hat{\mathbf{e}}^{\rm v}_x$ axis. One can easily show that in this co-rotating frame, an additional component $-\langle\omega\rangle^{(0)}\mathbf{H}_{\rm v}$ will be introduced such that equation (4.4) becomes

$$\frac{d}{dr}\mathbf{s}_\omega = \mathbf{s}_\omega \times \left[(\omega - \langle\omega\rangle^{(0)})\mathbf{H}_{\rm v} + \mathbf{H}_e - \mu(r)\mathbf{S}^{(0)}\right]. \tag{4.7}$$

In this frame, the corresponding resonance condition then becomes :

$$\omega_{\rm res}(r) = \langle\omega\rangle^{(0)} + \frac{\lambda(r) + \mu(r)S^{(0)}_{z,f}}{\cos 2\theta_{\rm v}}. \tag{4.8}$$

Therefore, only those neutrinos with $\omega > \langle\omega\rangle^{(0)}$ will be converted to ν_x by going through the resonance. For $\mathbf{s}_\omega$ with $\omega < \langle\omega\rangle^{(0)}$, they will stay in the direction of $\mathbf{H}_{\rm v}$ and thus

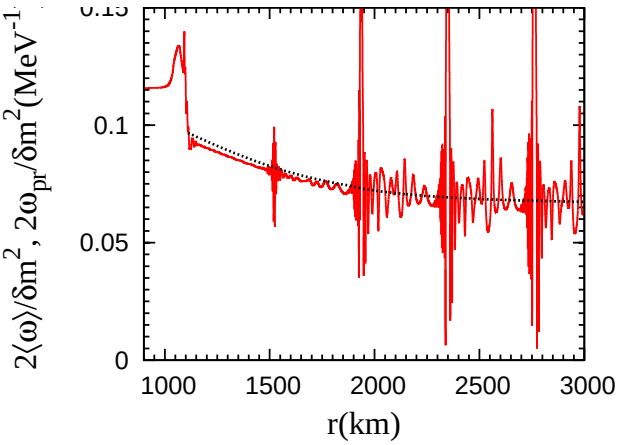

Figure 4.7: $\langle\omega\rangle$ and $\omega_{\rm pr}$ in the single-angle simulation as functions of r. Note that both change with radius but agree with each other well. The asymptotic value when $\mu \to 0$ gives the correct value of split frequency ω_s.

remain as ν_e in the two-flavor mixing scenario. As a result, a spectral split at $\langle\omega\rangle^{(0)}$ would emerge as shown in Fig. 4.5.

4.1.3 Discussions and Summary

From section 4.1.2, we see that the zeroth-order mean field approximation provides a very simple qualitatively understanding for how **S** should evolve and how the spectral split is formed. It also gives a relatively good description for the non-adiabaticity of low energy neutrinos that are affected by the bump in the n_e profile. However, from Fig. 4.5, we see that the position of the spectral split is at quite different ω in the case with or without using the zeroth-order mean field approximation. This is because when the majority part of the ν_e spectra has gone or is going through the resonance, $\mathbf{s}_\omega$ and **S** no longer align to each other. However, they still roughly remain in the same plane. As a result, $\langle\omega\rangle$ becomes

$$\langle\omega\rangle \approx \frac{\int \omega g(\omega)\mathbf{s}_\omega d\omega \times \mathbf{H}_{\rm v}}{\mathbf{S}\times\mathbf{H}_{\rm v}}. \tag{4.9}$$

In Fig. 4.7, we compare this $\langle\omega\rangle$ and $\omega_{\rm pr}$ which can be calculated from equation (34)

and (35) in [58] using the asymptotic value of S_z. It is clear that by neglecting the fast oscillations around the mean value of $\langle\omega\rangle$, $\langle\omega\rangle$ and $\omega_{\rm pr}$ basically agree to each other. Also, the asymptotic value of $\langle\omega\rangle \approx \omega_{\rm pr}$ when $\mu \to 0$ agrees with the split frequency ω_s very well at $\frac{2\omega}{\delta m^2} \approx 0.067$ MeV^{-1} as shown in Fig 4.5.

For the multi-angle approximation, the angle-averaging results are in very good agreement with the single-angle results as shown in Fig. 4.2. (For the detailed survival probabilities P_{ee} as a function of both emission angle and energy and some discussions about the slight angle-dependence, please see [29, 34] as references.)

As for the full three-flavor mixing scenario, for NH, ν_e with $E < E_{s,\rm atm}$ will remain in the heaviest mass eigenstate which is $|\nu_3\rangle$ after the atmospheric scale, where $E_{s,\rm atm} = |\Delta m^2_{\rm atm}|/2\omega_{s,\rm atm} \approx 15$ MeV. They will then decouple from the later evolution through the solar scale since θ_{13} is small. For ν_e with $E > E_{s,\rm atm}$, since $\mu \gg \{\omega_{\rm sol}, \lambda\}$ after the atmospheric scale but before the solar scale, they thus form another $\mathbf{S}_{\rm sol}$ which simply precesses around $\mathbf{H}_{\rm v,sol}$ in the three-dimensional real space spanned by the 1-2 flavor subspace. With $\mu(r)$ decreasing, a second spectral split forms at $E_{s,\rm sol} \approx 19$ MeV such that ν_e with $E < E_{s,\rm sol}$ being in the heavier state of $|\nu_2\rangle$ and ν_e with $E > E_{s,\rm sol}$ being in the lightest state of $|\nu_1\rangle$. For IH, since only the resonances that occur in the solar scale are involved, there is only one spectral split at $E_{s,\rm sol} \approx 11$ MeV such that ν_e with $E < E_{s,\rm sol}$ being in the heaviest state of $|\nu_2\rangle$ and ν_e with $E > E_{s,\rm sol}$ being in the lighter state of $|\nu_1\rangle$. (See [59–61] for detailed discussions.)

The above discussions basically summarize and explain the neutrino oscillations that occur for a specific luminosity and density profile that is representative for the neutronization burst phase of O-Ne-Mg supernovae. Note that in an actual situation, as shown in Fig. 2.1, the neutrino luminosity and the average energy are both changing with time. A detailed discussion of the luminosity dependence and the time-averaging neutrino signal can be found in [30] and there we see that the sharpness of the spectral split depends on the micro-physics adopted in the supernova models. Also, a detailed discussion of the interesting interplay of neutrino oscillations and the bump in the

electron density profile can be found in [29], which might have some future observation interests.

4.2 Resonances Driven by a Neutrino Gyroscope

In this section we focus on the occurrence of spectral swaps for the case where the initial number densities of ν_e and $\bar{\nu}_e$ are significantly larger than those of ν_x and $\bar{\nu}_x$ that mimic the neutrino emission during the accretion phase. We assume that all neutrinos are emitted from a neutrino sphere of radius $R_\nu = 10$ km with a normalized spectrum of the form

$$f_{\nu_\alpha}(E) = \frac{128}{3}\frac{E^3}{\langle E_{\nu_\alpha}\rangle^4}\exp(-4E/\langle E_{\nu_\alpha}\rangle), \tag{4.10}$$

where $\langle E_{\nu_\alpha}\rangle$ is the average energy. We take $\langle E_{\nu_e}\rangle = 10$ MeV, $\langle E_{\bar{\nu}_e}\rangle = 15$ MeV, and $\langle E_{\nu_x}\rangle = \langle E_{\bar{\nu}_x}\rangle = 24$ MeV. We further take the neutrino luminosity to be $L_{\nu_a} = 10^{51}$ erg/s for each species so that the initial number densities of ν_e, $\bar{\nu}_e$, ν_x, and $\bar{\nu}_x$ are in ratios of $2.4 : 1.6 : 1 : 1$.

Also, we assume that the electron density n_e here is not high enough (roughly speaking $n_e \ll n_{\nu_e} - n_{\bar{\nu}_e}$) such that the multi-angle matter-suppression effect [26,27,62] would not occur. This enables us to transform away the matter effect by adopting a much smaller effective mixing angle [24] which is chosen to be $\theta_{\rm v} = 10^{-5}$ here.

We first follow the flavor evolution under the single-angle approximation by solving equation (3.30) up to a radius $r = 250$ km, where the oscillations have effectively ceased. Figure 4.8 compares the neutrino flux spectra at the neutrino sphere (dashed curves) and at $r = 250$ km (solid curves). The vertical scale measures the relative energy-differential fluxes, which are $\propto L_{\nu_a} f_{\nu_a}(E)/\langle E_{\nu_a}\rangle$ at the neutrino sphere. It can be seen that the ν_e and ν_x spectra are swapped for $E \gtrsim 7.6$ MeV and the $\bar{\nu}_e$ and $\bar{\nu}_x$ spectra are swapped for $E \gtrsim 3.1$ MeV. To highlight these spectral changes, we define a "swap factor"

$$f_S(\omega, t) \equiv s^{\rm f}_{\omega,z}(t)/s^{\rm f}_{\omega,z}(0), \tag{4.11}$$

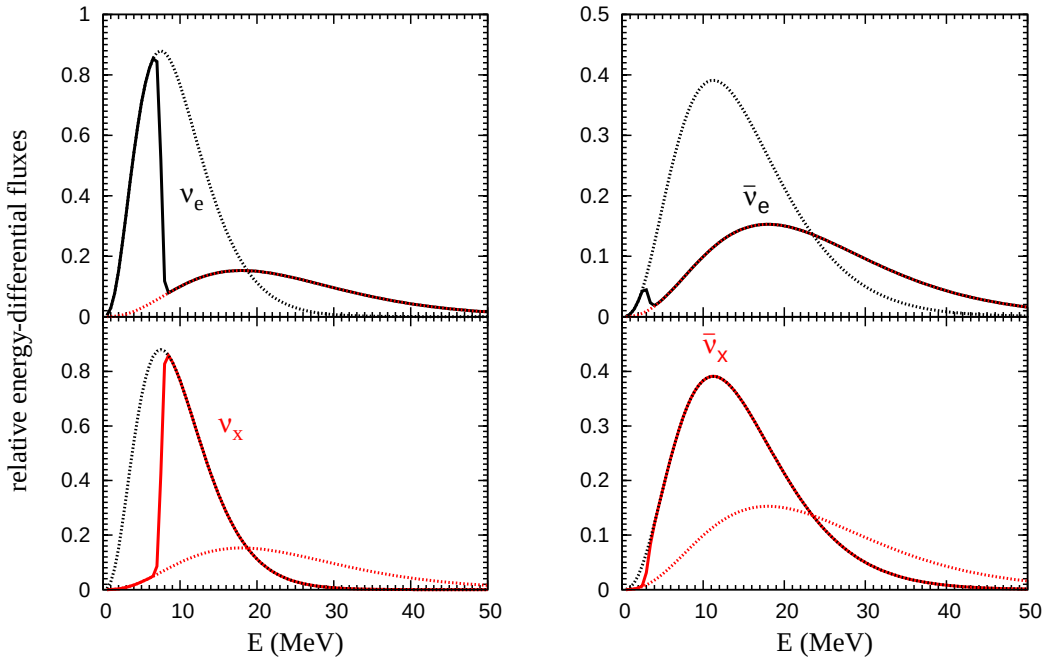

Figure 4.8: An example of stepwise spectral swaps for the IH and for the case where the initial number densities of ν_e and $\bar{\nu}_e$ are significantly larger than those of ν_x and $\bar{\nu}_x$. The neutrino flux spectra at the neutrino sphere (dashed curves) and at $r = 250$ km (solid curves) are shown. The dashed curves with larger maxima are for the initial ν_e and $\bar{\nu}_e$ while those with lower maxima are for the initial ν_x and $\bar{\nu}_x$. It can be seen that the ν_e and ν_x spectra are swapped for $E \gtrsim 7.6$ MeV and the $\bar{\nu}_e$ and $\bar{\nu}_x$ spectra are swapped for $E \gtrsim 3.1$ MeV.

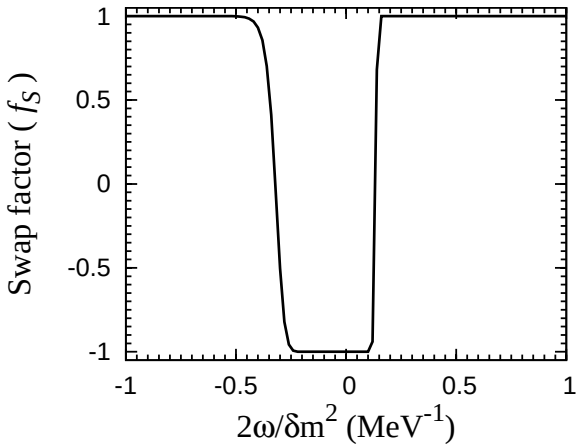

Figure 4.9: The swap factor $f_S(\omega, t)$ at $r = 250$ km as a function of $2\omega/\delta m^2$ for the example shown in Fig. 4.8. Note that the negative range of the horizontal axis corresponds to $\bar{\nu}_e$ and $\bar{\nu}_x$ while the positive range corresponds to ν_e and ν_x.

where $s^{\rm f}_{\omega,z}(t) \equiv \mathbf{s}_\omega(t) \cdot \hat{\mathbf{e}}^{\rm f}_z$. The value of $f_S(\omega, t) = 1$ or -1 corresponds to complete survival or conversion of the initial ν_a, respectively. The swap factor $f_S(\omega, t)$ at $r = 250$ km for the above example is shown as a function of $2\omega/\delta m^2$ in Fig. 4.9. Note that here we only discuss the IH case because the flavor oscillations is suppressed in NH as will be seen later.

4.2.1 Zeroth-order Mean Field and Neutrino Gyroscope

We show the effective neutrino spectra $2g(\omega)/\delta m^2$ as a function of $2\omega/\delta m^2$ for our supernova example in Fig. 4.10. There are three "spectral crossings" [55] at $\omega = \omega_-$, 0, and ω_+, respectively, for which $g(\omega) = 0$. We consider that the four spectral regions $(-\infty, \omega_-)$, $(\omega_-, 0)$, $(0, \omega_+)$, and (ω_+, ∞) can be represented by four effective NFIS's $\mathbf{s}^{(0)}_{\bar{e}}$, $\mathbf{s}^{(0)}_{\bar{x}}$, $\mathbf{s}^{(0)}_x$, and $\mathbf{s}^{(0)}_e$, respectively, which correspond to a $\bar{\nu}_e$, a $\bar{\nu}_x$, a ν_x, and a ν_e at the neutrino sphere. We then approximate $\mathbf{S}$ by the zeroth-order mean field

$$\mathbf{S}^{(0)} = \alpha_e \mathbf{s}^{(0)}_e + \alpha_x \mathbf{s}^{(0)}_x + \alpha_{\bar{x}} \mathbf{s}^{(0)}_{\bar{x}} + \alpha_{\bar{e}} \mathbf{s}^{(0)}_{\bar{e}}, \tag{4.12}$$

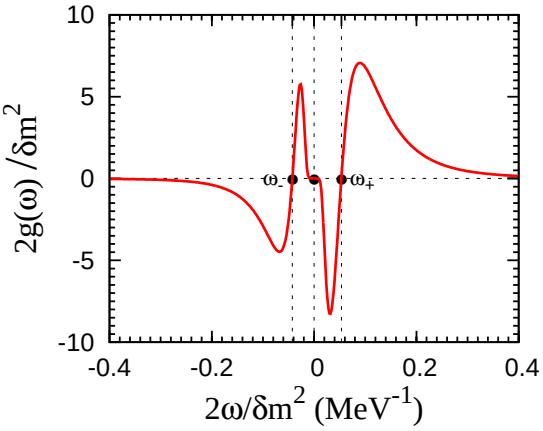

Figure 4.10: Example supernova neutrino spectrum shown in terms of $2g(\omega)/\delta m^2$ as a function of $2\omega/\delta m^2$. There are three spectral crossings (filled circles) at $\omega = \omega_-$, 0, and ω_+, respectively, for which $g(\omega) = 0$.

where the evolution of each $\mathbf{s}_a^{(0)}$ is governed by

$$\frac{d}{dr}\mathbf{s}_a^{(0)} = \mathbf{s}_a^{(0)} \times \left[\omega_a \mathbf{H}_{\rm v} - \mu(r)\mathbf{S}^{(0)}\right]. \tag{4.13}$$

In the above equations,

$$\alpha_e = \int_{\omega_+}^{\infty} |g(\omega)| d\omega, \tag{4.14}$$

$$\omega_e = \frac{1}{\alpha_e}\int_{\omega_+}^{\infty} \omega |g(\omega)| d\omega, \tag{4.15}$$

and other quantities are defined similarly. For our supernova example, $\alpha_e = 0.78$, $\alpha_x = 0.20$, $\alpha_{\bar{x}} = 0.10$, and $\alpha_{\bar{e}} = 0.35$, while $2\omega_a/\delta m^2 = 0.15$, 0.032, -0.027, and -0.11 MeV^{-1} for $\mathbf{s}_e^{(0)}$, $\mathbf{s}_x^{(0)}$, $\mathbf{s}_{\bar{x}}^{(0)}$, and $\mathbf{s}_{\bar{e}}^{(0)}$, respectively.

At the neutrino sphere, $\mathbf{S} = \mathbf{S}^{(0)} = \hat{\mathbf{e}}_z^{\rm f}/6$. As can be shown from Eqs. (3.30) and (4.13), the components of $\mathbf{S}$ and $\mathbf{S}^{(0)}$ parallel to $\mathbf{H}_{\rm v}$ are conserved during the subsequent evolution. We numerically obtain their components perpendicular to $\mathbf{H}_{\rm v}$, $S_\perp$ (solid curve) and $S_\perp^{(0)}$ (dashed curve), and show these as functions of $\mu(r)/\omega_e$ in Fig. 4.11. It can be seen that $S_\perp^{(0)}$ closely tracks $S_\perp$ for $\mu(r)/\omega_e \gtrsim 20$ but large deviations occur

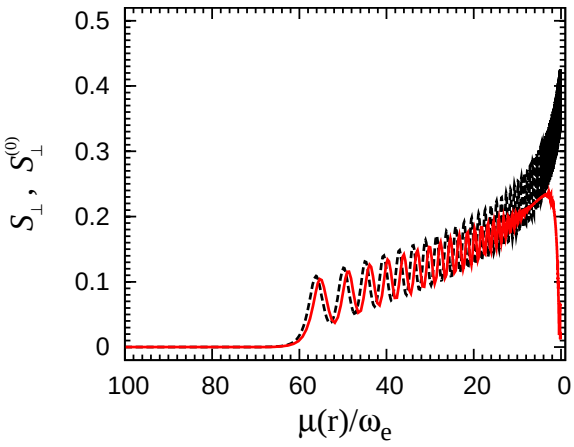

Figure 4.11: Comparison of $S_\perp$ (solid curve) and $S_\perp^{(0)}$ (dashed curve) as functions of $\mu(r)/\omega_e$ for the supernova example.

for $\mu(r)/\omega_e < 10$. In particular, $S_\perp^{(0)}$ diverges from $S_\perp$ at $\mu(r)/\omega_e < 4$. The above results can be understood by comparing $\mu(r)|\mathbf{S}|$ with the spread in ω for the spectrum shown in Fig. 4.10. For $\mu(r)/\omega_e \gtrsim 20$, $\mu(r)|\mathbf{S}| \gtrsim 3\omega_e$ exceeds the spread over the entire spectrum $\Delta\omega \sim 2\omega_e$. So all NFIS's evolve collectively in this regime and the four effective NFIS's included in $\mathbf{S}^{(0)}$ are sufficient to give a good description of $\mathbf{S}$. For $\mu(r)/\omega_e \sim 10$, $\mu(r)|\mathbf{S}| \sim \omega_e$ approaches $\Delta\omega_e = 0.66\omega_e$, which is the spread in the spectral region (ω_+, ∞) calculated from

$$\Delta\omega_e = \frac{1}{\alpha_e}\left[\int_{\omega_+}^{\infty}(\omega-\omega_e)^2|g(\omega)|d\omega\right]^{1/2}. \tag{4.16}$$

Consequently, for $\mu(r)/\omega_e < 10$, the NFIS's in the above spectral region are no longer well represented by $\mathbf{s}_e^{(0)}$ and large differences between $S_\perp^{(0)}$ and $S_\perp$ occur. Eventually, none of the effective NFIS's can represent their respective spectral regions and $S_\perp^{(0)}$ diverges from $S_\perp$.

System Initially Consisting of ν_e and $\bar{\nu}_e$ Only

In our supernova example, the initial number densities of ν_e and $\bar{\nu}_e$ are significantly larger than those of ν_x and $\bar{\nu}_x$. To facilitate an analytic study, we consider a simpler system initially consisting of ν_e and $\bar{\nu}_e$ only. We take normalized emission spectra of the form in Eq. (4.10) with $\langle E_{\nu_e} \rangle = \langle E_{\bar{\nu}_e} \rangle = 12$ MeV and luminosities $L_{\nu_e} = 1.2 \times 10^{51}$ and $L_{\bar{\nu}_e} = 0.8 \times 10^{51}$ erg s^{-1} so that the initial number densities of ν_e and $\bar{\nu}_e$ are the same as those in the supernova example. In this case, the effective neutrino spectrum $g(\omega)$ reduces to

$$h(\omega) = \frac{\delta m^2}{2\omega^2} \times \begin{cases} f_{\nu_e}(E_\omega), & \text{for } \omega > 0, \\ \alpha f_{\bar{\nu}_e}(E_\omega), & \text{for } \omega < 0, \end{cases} \tag{4.17}$$

where $\alpha = n_{\bar{\nu}_e}(R_\nu)/n_{\nu_e}(R_\nu) = 2/3$.

We consider that the zeroth order approximation for the mean field $\mathbf{S} = \int_{-\infty}^{\infty} h(\omega)\mathbf{s}_\omega d\omega$ is given by

$$\mathbf{S}^{(0)} \equiv \mathbf{s}_1^{(0)} + \alpha \mathbf{s}_2^{(0)}, \tag{4.18}$$

where $\mathbf{s}_1^{(0)}$ and $\mathbf{s}_2^{(0)}$ are the NFIS's for an initial ν_e and an initial $\bar{\nu}_e$ with

$$\omega_1 = \int_0^{\infty} \omega h(\omega) d\omega, \tag{4.19}$$

$$\omega_2 = \frac{1}{\alpha} \int_{-\infty}^{0} \omega h(\omega) d\omega, \tag{4.20}$$

respectively. Specifically, $\omega_1 = -\omega_2 \equiv \mu_{\rm v}$ and $2\mu_{\rm v}/\delta m^2 = 1/9$ MeV^{-1}. We show $S_\perp$ (solid curve) and $S_\perp^{(0)}$ (dashed curve) as functions of $\mu(r)/\mu_{\rm v}$ in Fig. 4.12. It can be seen that the comparison between $S_\perp$ and $S_\perp^{(0)}$ is very similar to that in the supernova example [note that the horizontal scales for Figs. 4.11 and 4.12 are related by $\mu(r)/\mu_{\rm v} = 1.35\mu(r)/\omega_e$].

The swap factor $f_S(\omega, t)$ at $r = 250$ km for the system initially consisting of ν_e and $\bar{\nu}_e$ only is shown as the solid curve in Fig. 4.13. The swap factor $f_S^{(0)}(\omega, t)$ calculated from

$$\frac{d}{dr}\mathbf{s}_\omega = \mathbf{s}_\omega \times \left[\omega \mathbf{H}_{\rm v} - \mu(r)\mathbf{S}^{(0)}\right], \tag{4.21}$$

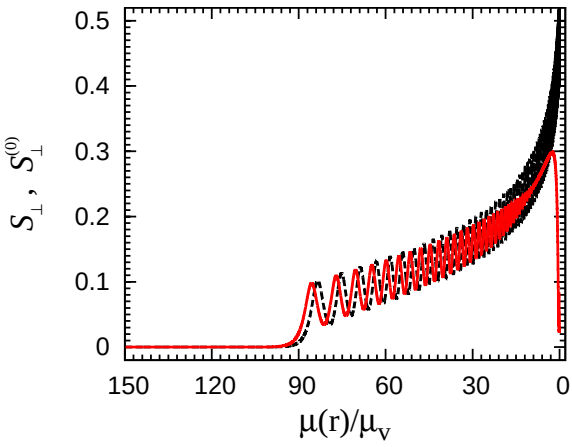

Figure 4.12: Comparison of $S_\perp$ (solid curve) and $S_\perp^{(0)}$ (dashed curve) as functions of $\mu(r)/\mu_{\rm v}$ for the system initially consisting of ν_e and $\bar{\nu}_e$ only.

which uses $\mathbf{S}^{(0)}$ to approximate $\mathbf{S}$, is shown as the dashed curve. It can be seen that just as in the supernova example, $f_S(\omega,t)$ and $f_S^{(0)}(\omega,t)$ have two characteristic split energies, one in the region of $\omega > 0$ and the other in the region of $\omega < 0$. Although $f_S^{(0)}(\omega,t)$ has a different split energy from that of $f_S(\omega,t)$ in the region of $\omega < 0$, they have the same qualitative behavior, especially the same split energy in the region of $\omega > 0$. Our goal is to understand the behavior of $f_S^{(0)}(\omega,t)$ analytically.

Neutrino Gyroscope as the Approximate Mean Field

For the system initially consisting of ν_e and $\bar{\nu}_e$ only, the evolution of $\mathbf{s}_1^{(0)}$ and $\mathbf{s}_2^{(0)}$ is governed by

$$\frac{d}{dr}\mathbf{s}_1^{(0)} = \mathbf{s}_1^{(0)} \times \left[\mu_{\rm v}\mathbf{H}_{\rm v} - \mu(r)\mathbf{S}^{(0)}\right], \tag{4.22}$$

$$\frac{d}{dr}\mathbf{s}_2^{(0)} = \mathbf{s}_2^{(0)} \times \left[-\mu_{\rm v}\mathbf{H}_{\rm v} - \mu(r)\mathbf{S}^{(0)}\right]. \tag{4.23}$$

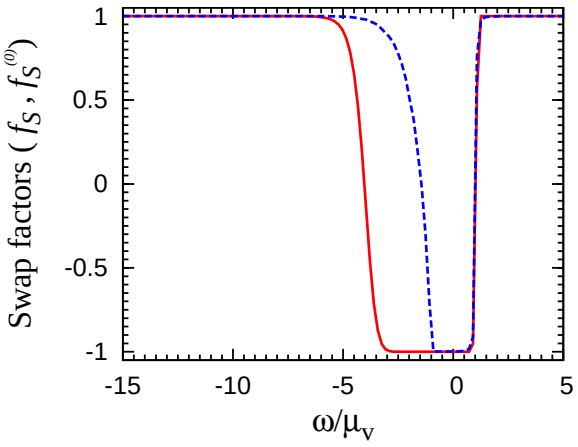

Figure 4.13: Comparison of the swap factors $f_S(\omega, t)$ (solid curve) and $f_S^{(0)}(\omega, t)$ (dashed curve) at $r = 250$ km for the system initially consisting of ν_e and $\bar{\nu}_e$ only.

For convenience, we will drop the superscript "(0)". It is useful to consider the time evolution of $\mathbf{s}_1$ and $\mathbf{s}_2$ at a constant μ governed by

$$\dot{\mathbf{s}}_1 \equiv \frac{d}{dt}\mathbf{s}_1 = \mathbf{s}_1 \times (\mu_{\rm v}\mathbf{H}_{\rm v} - \mu\mathbf{S}), \tag{4.24}$$

$$\dot{\mathbf{s}}_2 \equiv \frac{d}{dt}\mathbf{s}_2 = \mathbf{s}_2 \times (-\mu_{\rm v}\mathbf{H}_{\rm v} - \mu\mathbf{S}). \tag{4.25}$$

As discussed in [63,64] and repeated below, the system governed by the above equations is mathematically equivalent to a gyroscope in a uniform gravitational field.

From Eqs. (4.24) and (4.25) it is straightforward to show that

$$\dot{\mathbf{Q}} = \mu\mathbf{S} \times \mathbf{Q}, \tag{4.26}$$

$$\dot{\mathbf{S}} = \mu_{\rm v}\mathbf{Q} \times \mathbf{H}_{\rm v}, \tag{4.27}$$

where

$$\mathbf{Q} = \mathbf{s}_1 - \alpha\mathbf{s}_2 + \frac{\mu_{\rm v}}{\mu}\mathbf{H}_{\rm v}. \tag{4.28}$$

From Eq. (4.26) it can be shown that $Q \equiv |\mathbf{Q}|$ is conserved. With the definition of a

unit vector $\hat{\mathbf{r}} \equiv \mathbf{Q}/Q$, Eqs. (4.26) and (4.27) can be rewritten as

$$\mathbf{S} = \frac{1}{\mu}\hat{\mathbf{r}} \times \dot{\hat{\mathbf{r}}} + \sigma\hat{\mathbf{r}}, \tag{4.29}$$

$$\dot{\mathbf{S}} = \tfrac{1}{\mu}\hat{\mathbf{r}} \times \mathbf{g}, \tag{4.30}$$

where $\sigma \equiv \mathbf{S} \cdot \hat{\mathbf{r}}$ and $\mathbf{g} \equiv \mu\mu_{\rm v} Q\mathbf{H}_{\rm v}$. The above equations describe the motion of a gyroscope in a uniform gravitational field with an acceleration of gravity $\mathbf{g}$. The gyroscope has a spinning point particle of mass $1/\mu$ attached to the tip of a massless rod of unit length. The spin of the gyroscope is along the direction $\hat{\mathbf{r}}$ of the rod and it can be shown from Eqs. (4.26) and (4.27) that the magnitude σ of the spin is conserved. As can be seen from Eq. (4.30), the component of the total angular momentum $\mathbf{S}$ parallel to $\mathbf{H}_{\rm v}$ is also conserved.

If μ varies smoothly with time, the neutrino gyroscope described above evolves through a series of configurations corresponding to a continuous range of μ. The motion of this gyroscope provides a well-studied mechanical analog to the evolution of the approximate mean field.

4.2.2 Precession and Nutation of The Neutrino Gryoscope

We specify the unit vector $\hat{\mathbf{r}}$ of the neutrino gyroscope by two of the Euler angles, θ and ϕ, in Frame I:

$$\hat{\mathbf{r}} = \sin\theta\sin\phi\,\hat{\mathbf{e}}^{\rm I}_x - \sin\theta\cos\phi\,\hat{\mathbf{e}}^{\rm I}_y + \cos\theta\,\hat{\mathbf{e}}^{\rm I}_z, \tag{4.31}$$

where $\hat{\mathbf{e}}^{\rm I}_x$, $\hat{\mathbf{e}}^{\rm I}_y$, and $\hat{\mathbf{e}}^{\rm I}_z$ are the unit vectors associated with the three axes of Frame I and $\hat{\mathbf{e}}^{\rm I}_z = -\mathbf{H}_{\rm v}$ (see Fig. 4.14). We focus on the IH with $\tilde{\theta}_{\rm v} \ll 1$, for which $\mathbf{H}_{\rm v} = -\sin 2\tilde{\theta}_{\rm v}\hat{\mathbf{e}}^{\rm f}_x - \cos 2\tilde{\theta}_{\rm v}\hat{\mathbf{e}}^{\rm f}_z \approx -\hat{\mathbf{e}}^{\rm f}_z$. Thus, $\hat{\mathbf{e}}^{\rm I}_z \approx \hat{\mathbf{e}}^{\rm f}_z$ is the upward direction and $\mathbf{g}$ (in the same direction as $\mathbf{H}_{\rm v}$) points downward. When the neutrino gyroscope starts at $\mu \gg \mu_{\rm v}$, $\mathbf{Q} \approx \mathbf{s}_1 - \alpha\mathbf{s}_2$ points in the direction of $\hat{\mathbf{e}}^{\rm f}_z$, i.e., it is in the upright position. This initial configuration can give rise to interesting subsequent evolution.

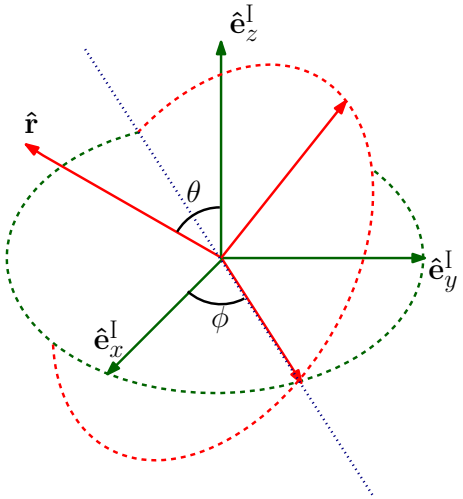

Figure 4.14: Euler angles for the unit vector $\hat{\mathbf{r}}$ of the neutrino gyroscope in Frame I. The azimuthal angle ϕ and the polar angle θ are associated with precession and nutation of the gyroscope, respectively.

Motion of the Neutrino Gyroscope at Constant μ

We first discuss motion of the neutrino gyroscope at constant μ. Using Eq. (4.29), we can express $\mathbf{S}$ in terms of θ and ϕ as

$$S_x = \frac{1}{\mu}(\dot{\theta}\cos\phi - \dot{\phi}\sin\theta\cos\theta\sin\phi) + \sigma\sin\theta\sin\phi, \tag{4.32}$$

$$S_y = \frac{1}{\mu}(\dot{\theta}\sin\phi + \dot{\phi}\sin\theta\cos\theta\cos\phi) - \sigma\sin\theta\cos\phi, \tag{4.33}$$

$$S_z = \frac{1}{\mu}\dot{\phi}\sin^2\theta + \sigma\cos\theta = \frac{1-\alpha}{2}\cos 2\tilde{\theta}_{\mathrm{v}}, \tag{4.34}$$

where we have used conservation of S_z in the exact form (i.e., no approximation made for $\tilde{\theta}_{\mathrm{v}} \ll 1$) in the last equation. In addition to σ and S_z, the third conserved quantity of the gyroscope is its total energy:

$$E_{\mathrm{gyro}} = \frac{\mu}{2}\mathbf{S}^2 - \frac{1}{\mu}\hat{\mathbf{r}}\cdot\mathbf{g}, \tag{4.35}$$

$$= \frac{1}{2\mu}\left(\dot{\theta}^2 + \dot{\phi}^2\sin^2\theta\right) + \frac{\mu}{2}\sigma^2 + \mu_{\mathrm{v}}Q\cos\theta. \tag{4.36}$$

Conservation of $E_{\rm gyro}$ can be shown using Eqs. (4.29) and (4.30). We can also derive an explicit equation of motion from Eq. (4.30):

$$\ddot{\theta} - \dot{\phi}(\dot{\phi}\cos\theta - \mu\sigma)\sin\theta = \mu\mu_{\rm v}Q\sin\theta. \tag{4.37}$$

In general, both θ and ϕ of a gyroscope evolve with time, and the corresponding motion is referred to as nutation (θ) and precession (ϕ). For the neutrino gyroscope, conservation of σ, S_z, $E_{\rm gyro}$ can be combined to give a conserved effective energy associated with nutation only:

$$E_\theta = E_{\rm gyro} - \frac{\mu}{2}\sigma^2 = \frac{\dot{\theta}^2}{2\mu} + V_{\rm eff}(\theta), \tag{4.38}$$

where

$$V_{\rm eff}(\theta) = \frac{\mu}{2}\frac{(S_z - \sigma\cos\theta)^2}{\sin^2\theta} + \mu_{\rm v}Q\cos\theta. \tag{4.39}$$

As shown in Fig. 4.15, nutation of the neutrino gyroscope mostly occurs around the minimum of the effective potential $V_{\rm eff}(\theta)$. This potential minimum corresponds to $\theta = \theta_p$, for which

$$\left.\frac{dV_{\rm eff}}{d\theta}\right|_{\theta_p} = \mu\frac{(S_z - \sigma\cos\theta_p)(\sigma - S_z\cos\theta_p)}{\sin^3\theta_p} - \mu_{\rm v}Q\sin\theta_p = 0, \tag{4.40}$$

$$\mu\left.\frac{d^2V_{\rm eff}}{d\theta^2}\right|_{\theta_p} = \dot{\phi}_p^2\sin^2\theta_p + \Big(2\dot{\phi}_p\cos\theta_p - \mu\sigma\Big)^2 \equiv \omega_n^2 > 0. \tag{4.41}$$

In Eq. (4.41), $\dot{\phi}_p$ is the instantaneous precession frequency at the potential minimum and can be obtained from Eq. (4.34) after θ_p is solved from Eq. (4.40). Note that Eq. (4.40) is the same as

$$\dot{\phi}_p(\dot{\phi}_p\cos\theta_p - \mu\sigma) + \mu\mu_{\rm v}Q = 0, \tag{4.42}$$

which can also be obtained by setting $\ddot{\theta} = 0$ and $\dot{\phi} = \dot{\phi}_p$ in Eq. (4.37). In other words, the minimum $V_{\rm eff}$ corresponds to the maximum $\dot{\theta}$, and hence $\ddot{\theta} = 0$.

To the leading order, nutation can be approximated as oscillations of θ around θ_p in response to the potential

$$V_{\rm eff}(\theta) \approx V_{\rm eff}(\theta_p) + \frac{\omega_n^2}{2\mu}(\theta - \theta_p)^2. \tag{4.43}$$

In this approximation, the motion of the neutrino gyroscope can be described by

$$\theta \approx \theta_p - \eta \cos\omega_n t, \tag{4.44}$$

$$\dot{\theta} \approx \eta\omega_n \sin\omega_n t, \tag{4.45}$$

$$\phi \approx \dot{\phi}_p t - \eta \left[\frac{\mu\sigma - 2\dot{\phi}_p \cos\theta_p}{\omega_n \sin\theta_p}\right] \sin\omega_n t, \tag{4.46}$$

$$\dot{\phi} \approx \dot{\phi}_p - \eta \left[\frac{\mu\sigma - 2\dot{\phi}_p \cos\theta_p}{\sin\theta_p}\right] \cos\omega_n t. \tag{4.47}$$

From Eqs. (4.32)–(4.34) and (4.44)–(4.47) we obtain

$$\begin{aligned} S_x + iS_y \approx\ & i\left\{\left(\frac{\dot{\phi}_p}{\mu}\cos\theta_p - \sigma\right)\sin\theta_p + \frac{\eta}{2}\frac{\dot{\phi}_p}{\mu}\left[\left(1 - \frac{2\dot{\phi}_p - \mu S_z}{\omega_n}\right)\exp(i\omega_n t)\right.\right. \\ & + \left.\left.\left(1 + \frac{2\dot{\phi}_p - \mu S_z}{\omega_n}\right)\exp(-i\omega_n t)\right]\right\}\exp(i\dot{\phi}_p t), \end{aligned} \tag{4.48}$$

which is accurate to the first order in η. The above expression is derived assuming the initial conditions $\dot{\theta} = 0$ and $\phi = 0$. It can be shown that more general initial conditions only add constant phases to the exponential terms in Eq. (4.48). This equation shows that to the leading order, the angular momentum **S** can be described by three precessing vectors with different amplitudes and different precession frequencies, which are $\dot{\phi}_p$, $\dot{\phi}_p + \omega_n$, and $\dot{\phi}_p - \omega_n$, respectively. This leading-order expression of **S** provides a very useful analytic description of the motion of the neutrino gyroscope.

Motion of the Neutrino Gyroscope for Slowly Decreasing μ

We now extend the discussion to the case where $\mu(t)$ slowly decreases with time from a large initial value $\mu(0) \gg \mu_{\rm v}$. Specifically, we consider the system that initially consists of monoenergetic ν_e and $\bar{\nu}_e$ only and is governed by Eqs. (4.24) and (4.25). For this system, $2\mu_{\rm v}/\delta m^2 = 1/9$ MeV^{-1}, $\alpha = 2/3$, and

$$\mu(t) = \mu(0)\left[1 - \sqrt{1 - \left(\frac{\tau}{t+\tau}\right)^2}\right]^2, \tag{4.49}$$

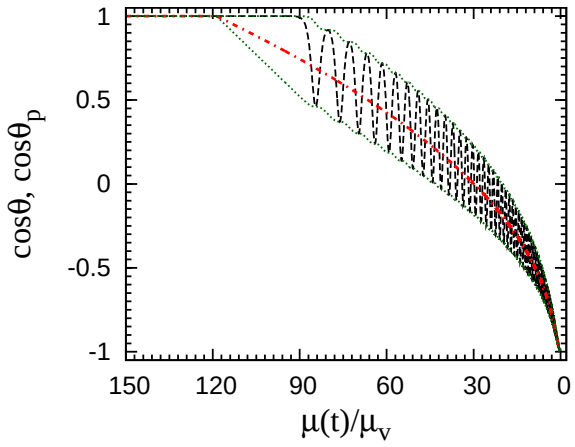

Figure 4.15: Nutation of the neutrino gyroscope shown in terms of $\cos\theta$ as a function of $\mu(t)/\mu_{\rm v}$ (dashed curve) for $\tilde{\theta}_{\rm v} = 10^{-5}$ (IH). The gyroscope is characterized by $2\mu_{\rm v}/\delta m^2 = 1/9$ MeV^{-1}, $\alpha = 2/3$, and $\mu(t) = \mu(0)\left\{1 - \sqrt{1-[\tau/(t+\tau)]^2}\right\}^2$, where $\mu(0)/\mu_{\rm v} = 2.52 \times 10^5$ and $\tau = 8.45/\mu_{\rm v}$. The dot-dashed curve is for $\cos\theta_p$, which corresponds to the minimum of the instantaneous $V_{\rm eff}(\theta)$, and the dotted curves are for $\cos\theta_{\rm max}$ and $\cos\theta_{\rm min}$, which correspond to $V_{\rm eff}(\theta) = E_\theta$.

where $\mu(0) = 2.52 \times 10^5 \mu_{\rm v}$ and $\tau = 8.45/\mu_{\rm v}$. The above form of $\mu(t)$ corresponds to $n_{\nu_e}(r)$ in the supernova example. Taking $\tilde{\theta}_{\rm v} = 10^{-5}$ (IH), we numerically solve Eqs. (4.24) and (4.25). Using the instantaneous $\mathbf{s}_1$ and $\mathbf{s}_2$ from the numerical results, we construct a gyroscope at each specific value of μ. We show $\cos\theta$ (dashed curve) for the series of gyroscopes as a function of $\mu(t)/\mu_{\rm v}$ in Fig. 4.15. Using σ and Q for each gyroscope and the fact that S_z is conserved even when μ changes with time [see Eq. (4.27)], we construct an "instantaneous" $V_{\rm eff}(\theta)$ from Eq. (4.39). We define $\theta_{\rm max}$ and $\theta_{\rm min}$ as the solutions to $V_{\rm eff}(\theta) = E_\theta$, where E_θ is the corresponding instantaneous effective energy [see Eq. (4.38)]. We show the evolution of $\cos\theta_{\rm max}$ and $\cos\theta_{\rm min}$ as the dotted curves in Fig. 4.15. We also calculate θ_p corresponding to the minimum of the instantaneous $V_{\rm eff}(\theta)$ and show the evolution of $\cos\theta_p$ as the dot-dashed curve in Fig. 4.15. Finally, we calculate $\dot{\phi}_p$ and ω_n from Eqs. (4.34) and (4.41) and show $\dot{\phi}_p/\mu_{\rm v}$

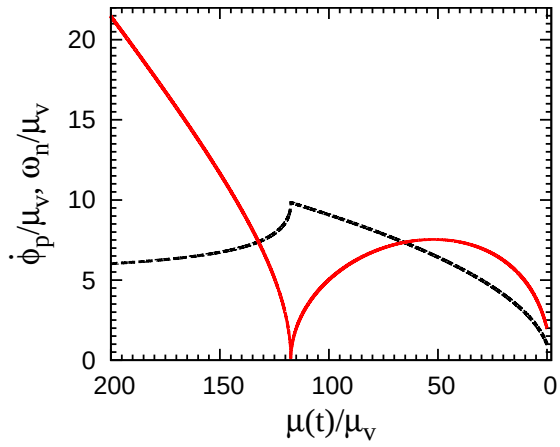

Figure 4.16: Dimensionless precession frequency $\dot{\phi}_p/\mu_{\rm v}$ (dashed curve) and nutation frequency $\omega_n/\mu_{\rm v}$ (solid curve) as functions of $\mu(t)/\mu_{\rm v}$ for the neutrino gyroscope shown in Fig. 4.15.

(dashed curve) and $\omega_n/\mu_{\rm v}$ (solid curve) as functions of $\mu(t)/\mu_{\rm v}$ in Fig. 4.16.

It can be seen from Fig. 4.15 that the general trend of θ follows the evolution of θ_p. In other words, nutation of the neutrino gyroscope occurs around the minimum of the instantaneous $V_{\rm eff}(\theta)$ as $\mu(t)$ slowly decreases from a large initial value $\mu(0) \gg \mu_{\rm v}$. It is also clear that the motion of the gyroscope falls into two distinct regimes separated by a critical $\mu_{\rm cr} \approx 119\mu_{\rm v}$. For $\mu > \mu_{\rm cr}$, the nutation amplitude is extremely small and $\theta \approx \theta_p$ to very good approximation. As μ drops below $\mu_{\rm cr}$, θ initially stays small even as θ_p increases. This can be understood from Fig. 4.16, which shows that the nutation frequency ω_n is small at $\mu \sim \mu_{\rm cr}$ and is practically zero at $\mu_{\rm cr}$. As μ decreases further, ω_n becomes sufficiently large and θ starts to oscillate around θ_p. The amplitude of this oscillation is also that of nutation, which can be taken as $\eta \approx (\theta_{\rm max} - \theta_{\rm min})/2$. The longer ω_n stays small at $\mu \sim \mu_{\rm cr}$, the larger η is for $\mu < \mu_{\rm cr}$.

We have constructed the series of gyroscopes for specific values of μ using the instantaneous $\mathbf{s}_1$ and $\mathbf{s}_2$ numerically calculated for the $\mu(t)$ in Eq. (4.49). In fact, so long as $\mu(t)$ slowly decreases from some large initial value $\mu(0) \gg \mu_{\rm v}$, the characteristics of such

gyroscopes essentially depend on the values of μ but not the specific functional form of $\mu(t)$. To see this, we consider the set of parameters σ, Q, and θ_p that characterize the gyroscope at a specific value of μ. We can choose three equations to solve for these parameters as follows. From the definitions of σ, $\mathbf{S}$, and $\mathbf{Q}$, we obtain

$$\sigma Q = \frac{1-\alpha^2}{4} - \frac{\mu_{\rm v}}{\mu} S_z, \tag{4.50}$$

$$S^2 + Q^2 + 2\frac{\mu_{\rm v}}{\mu} Q\cos\theta + \left(\frac{\mu_{\rm v}}{\mu}\right)^2 = \frac{1+\alpha^2}{2}. \tag{4.51}$$

Applying Eqs. (4.34) and (4.51) to $\theta = \theta_p$, at which $\dot{\theta}$ reaches its maximum value of $(\dot{\theta})_{\rm max} \approx \eta\omega_n$ [see Eqs. (4.44) and (4.45)], we further obtain

$$\frac{\dot{\phi}_p}{\mu}\sin^2\theta_p + \sigma\cos\theta_p = S_z, \tag{4.52}$$

$$\left(\frac{\eta\omega_n}{\mu}\right)^2 + \left(\frac{\dot{\phi}_p}{\mu}\right)^2 \sin^2\theta_p + \sigma^2 + Q^2 + 2\frac{\mu_{\rm v}}{\mu} Q\cos\theta_p + \left(\frac{\mu_{\rm v}}{\mu}\right)^2 \approx \frac{1+\alpha^2}{2}. \tag{4.53}$$

Treating η as a small parameter and ignoring the η^2 term in Eq. (4.53), we can solve this equation along with Eqs. (4.50) and (4.52) to obtain σ, Q, and θ_p [note that $\dot{\phi}_p$ is given in terms of σ, Q, and θ_p by Eq. (4.42); see Appendix A.1 for a different but equivalent method to obtain these parameters]. As this approximate solution assumes $\eta = 0$, it is a "pure-precession" solution [64], for which the gyroscope always stays at the minimum of the instantaneous $V_{\rm eff}(\theta)$.

For $\tilde{\theta}_{\rm v} \ll 1$, the pure-precession solution gives

$$\theta_p \ll 1, \tag{4.54}$$

$$\dot{\phi}_p \to \frac{1+\alpha}{1-\alpha}\mu_{\rm v}, \tag{4.55}$$

$$\omega_n \to \frac{1-\alpha}{2}\mu - 2\left(\frac{1+\alpha}{1-\alpha}\right)\mu_{\rm v}, \tag{4.56}$$

at $\mu \gg \mu_{\rm v}$ (see Appendix A.2 for more detailed discussion of the initial motion of the neutrino gyroscope), and

$$\theta_p \to \pi, \tag{4.57}$$

$$\dot{\phi}_p \rightarrow \mu_{\rm v}, \tag{4.58}$$

$$\omega_n \rightarrow 2\mu_{\rm v}, \tag{4.59}$$

at $\mu \ll \mu_{\rm v}$. In general, the θ_p, $\dot{\phi}_p$, and ω_n calculated for the pure-precession solution are within $\sim 1\%$ of the values shown in Figs. 4.15 and 4.16.

Equation (4.56) suggests that ω_n becomes very small as μ decreases to some critical value $\mu_{\rm cr}$. In Appendix A.3, we show that

$$\mu_{\rm cr} = \frac{4\mu_{\rm v}}{(1-\sqrt{\alpha})^2}, \tag{4.60}$$

which is $\mu_{\rm cr} \approx 119\mu_{\rm v}$ for $\alpha = 2/3$, in excellent agreement with Figs. 4.15 and 4.16. At $\mu = \mu_{\rm cr}$, we have (see Appendix A.3)

$$\theta_{p,{\rm cr}} \approx \frac{2\sqrt{2}\alpha^{1/6}}{(1+\sqrt{\alpha})^{2/3}}\tilde{\theta}_{\rm v}^{2/3}, \tag{4.61}$$

$$\dot{\phi}_{p,{\rm cr}} \approx \frac{\mu_{\rm cr}S_z}{2} \approx \frac{1+\sqrt{\alpha}}{1-\sqrt{\alpha}}\mu_{\rm v}, \tag{4.62}$$

$$\omega_{n,{\rm cr}} \approx \frac{\sqrt{3}}{2}\mu_{\rm cr}S_z\theta_{p,{\rm cr}} \approx \frac{2\sqrt{6}\alpha^{1/6}(1+\sqrt{\alpha})^{1/3}}{1-\sqrt{\alpha}}\tilde{\theta}_{\rm v}^{2/3}\mu_{\rm v}. \tag{4.63}$$

As $\theta_p \ll 1$ at $\mu \gg \mu_{\rm v}$ and at $\mu = \mu_{\rm cr}$ for $\tilde{\theta}_{\rm v} \ll 1$, the neutrino gyroscope stays in the upright position and behaves like a sleeping top at $\mu \geq \mu_{\rm cr}$ (see Fig. 4.15).

4.2.3 Resonances Driven by The Neutrino Gyroscope

In this section we return to the system initially consisting of ν_e and $\bar{\nu}_e$ with spectra of the form in Eq. (4.10). As discussed in Secs. 4.2.1, the approximate mean field of NFIS's for this system can be described by the neutrino gyroscope. We now try to understand the evolution of an individual NFIS in the system in terms of its response to the neutrino gyroscope. Specifically, we study the evolution of $\mathbf{s}_\omega$ governed by

$$\frac{d}{dt}\mathbf{s}_\omega = \mathbf{s}_\omega \times [\omega\mathbf{H}_{\rm v} - \mu(t)\mathbf{S}] = [\omega\hat{\mathbf{e}}_z^{\rm I} + \mu(t)\mathbf{S}] \times \mathbf{s}_\omega, \tag{4.64}$$

where $\mathbf{S}$ is the total angular momentum of the neutrino gyroscope discussed in Sec. 4.2.2.

Precession-Driven Resonance

We first ignore nutation and consider only precession of the neutrino gyroscope. With $\eta = 0$, Eq. (4.48) becomes

$$S_x + iS_y \approx iS_\perp \exp(i\dot{\phi}_p t), \tag{4.65}$$

where

$$S_\perp = \left(\frac{\dot{\phi}_p}{\mu}\cos\theta_p - \sigma\right)\sin\theta_p. \tag{4.66}$$

Equation (4.65) represents a vector rotating in the xy-plane of Frame I. Let Frame II rotate with an angular velocity $\dot{\phi}_p\hat{\mathbf{e}}_z^{\rm I}$ relative to Frame I. Then $\mathbf{S}$ is a non-rotating vector in Frame II and can be chosen as

$$\mathbf{S} \approx S_z\hat{\mathbf{e}}_z^{\rm I} + S_\perp\hat{\mathbf{e}}_y^{\rm II}, \tag{4.67}$$

where $\hat{\mathbf{e}}_y^{\rm II}$ is the unit vector in the y-direction of Frame II. We rewrite Eq. (4.64) in this frame as

$$\frac{d}{dt}\mathbf{s}_\omega = [(\omega + \mu S_z - \dot{\phi}_p)\hat{\mathbf{e}}_z^{\rm I} + \mu S_\perp\hat{\mathbf{e}}_y^{\rm II}] \times \mathbf{s}_\omega \equiv \mathbf{H}_{\rm II} \times \mathbf{s}_\omega. \tag{4.68}$$

Note that in the above equation ω and S_z are constants but $\dot{\phi}_p$ and $S_\perp$ are functions of $\mu(t)$. A resonance occurs at $\mu = \mu_{{\rm res},p}$, for which

$$\omega = \dot{\phi}_p(\mu_{{\rm res},p}) - \mu_{{\rm res},p}S_z, \tag{4.69}$$

and the z-component of $\mathbf{H}_{\rm II}$ vanishes. We refer to this as the precession-driven resonance. Using the neutrino gyroscope in Fig. 4.15, we show $\mu_{{\rm res},p}/\mu_{\rm v}$ as a function of $\omega/\mu_{\rm v}$ (solid curve) in Fig. 4.17 (note that the pure-precession solution gives essentially the same result).

The evolution of $\mathbf{s}_\omega$ in Frame II based on Eq. (4.68) is very similar to the MSW effect. At a specific time t, $\mathbf{s}_\omega$ precesses around the instantaneous $\mathbf{H}_{\rm II}$ with an angular velocity $\mathbf{H}_{\rm II}$. For slowly varying $\mu(t)$, the evolution of $\mathbf{s}_\omega$ is adiabatic in that the precession adjusts to the instantaneous angular velocity (the direction and magnitude of which are both changing slowly in general) but the angle between $\mathbf{s}_\omega$ and $\mathbf{H}_{\rm II}$ remains fixed.

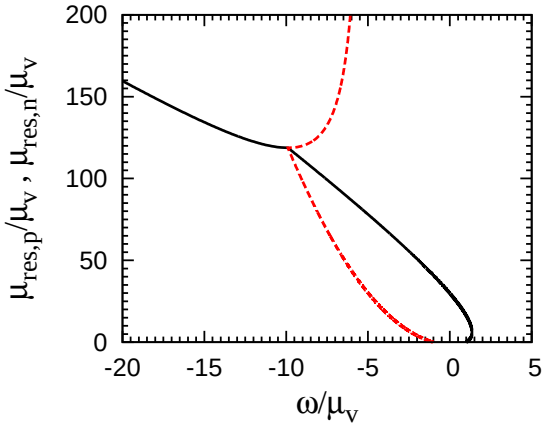

Figure 4.17: Values of $\mu_{\mathrm{res},p}/\mu_{\mathrm{v}}$ (solid curve) and $\mu_{\mathrm{res},n}/\mu_{\mathrm{v}}$ (dashed curve) as functions of ω/μ_{v}. An NFIS $\mathbf{s}_\omega$ goes through the precession-driven (nutation-driven) resonance at $\mu = \mu_{\mathrm{res},p}$ ($\mu_{\mathrm{res},n}$) as the neutrino gyroscope in Fig. 4.15 evolves through $\mu(t)$.

Therefore, the initial ν_e or $\bar{\nu}_e$ represented by $\mathbf{s}_\omega$ remains in the same flavor following adiabatic evolution if the initial and final directions of $\mathbf{H}_{\mathrm{II}}$ are the same, but is fully converted into a ν_x or $\bar{\nu}_x$ if the initial and final directions of $\mathbf{H}_{\mathrm{II}}$ are opposite. For the neutrino gyroscope under consideration, $\mathbf{H}_{\mathrm{II}} \approx \mu S_z \hat{\mathbf{e}}_z^{\mathrm{I}}$ at $t = 0$ corresponding to $\mu \gg \mu_{\mathrm{v}}$, where we have used $\mu S_z \gg |\omega|, \dot{\phi}_p, \mu|S_\perp|$ in this limit. At large times corresponding to $\mu \ll \mu_{\mathrm{v}}$, $\mathbf{H}_{\mathrm{II}} \approx (\omega - \mu_{\mathrm{v}})\hat{\mathbf{e}}_z^{\mathrm{I}}$, where we have used $\dot{\phi}_p = \mu_{\mathrm{v}}$ in this limit. Consequently, the initial and final directions of $\mathbf{H}_{\mathrm{II}}$ are the same for $\omega > \mu_{\mathrm{v}}$ but are opposite for $\omega < \mu_{\mathrm{v}}$. In the latter case, a precession-driven resonance occurs when the z-component of $\mathbf{H}_{\mathrm{II}}$ vanishes before the direction of $\mathbf{H}_{\mathrm{II}}$ is reversed. Thus, when only precession-driven resonance matters and adiabatic evolution applies, an initial ν_e with $\omega > \mu_{\mathrm{v}}$ remains as a ν_e, while an initial ν_e with $\omega < \mu_{\mathrm{v}}$ or an initial $\bar{\nu}_e$ (with $\omega < 0$) is fully converted into a ν_x or $\bar{\nu}_x$, respectively. This is basically the explanation for the stepwise spectral swap originally discovered in [53] (see also discussion in [65]).

For adiabatic evolution, the rate at which the direction of $\mathbf{H}_{\mathrm{II}}$ changes must be slow

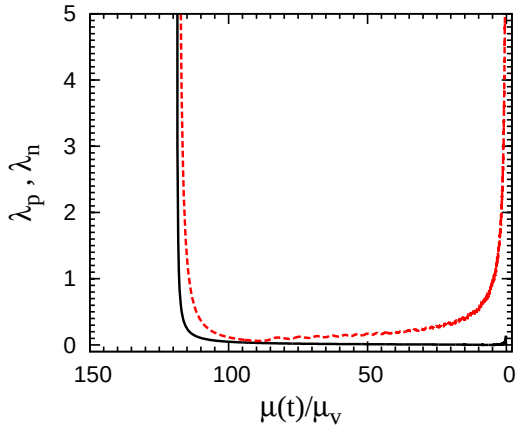

Figure 4.18: Adiabaticity parameters λ_p (solid curve) and λ_n (dashed curve) for evolution through precession-driven and nutation-driven resonances, respectively, as functions of $\mu(t)/\mu_{\rm v}$ for the neutrino gyroscope shown in Fig. 4.15.

compared with the precession frequency of $\mathbf{s}_\omega$:

$$\left|\frac{d}{dt}\frac{\mathbf{H}_{\rm II}}{|\mathbf{H}_{\rm II}|}\right| = \frac{|\mathbf{H}_{\rm II}\times d\mathbf{H}_{\rm II}/dt|}{|\mathbf{H}_{\rm II}|^2} \ll |\mathbf{H}_{\rm II}|. \tag{4.70}$$

The above condition is most stringent at resonance when the z-component of $\mathbf{H}_{\rm II}$ vanishes. We define the adiabaticity parameter for this precession-driven resonance as

$$\lambda_p \equiv \frac{|\mathbf{H}_{\rm II}\times d\mathbf{H}_{\rm II}/dt|_{\rm res}}{|\mathbf{H}_{\rm II}|^3_{\rm res}} = \frac{|d(\dot{\phi}_p-\mu S_z)/dt|}{(\mu S_\perp)^2}. \tag{4.71}$$

Adiabatic evolution obtains for $\lambda_p \ll 1$ (note that λ_p is defined differently from the usual adiabaticity parameter for the conventional MSW effect). Using the neutrino gyroscope in Fig. 4.15, we show λ_p as a function of $\mu(t)/\mu_{\rm v}$ (solid curve) in Fig. 4.18. It can be seen from this figure that evolution through the precession-driven resonance is adiabatic at $\mu < 115\mu_{\rm v}$, but is extremely nonadiabatic at $\mu \gtrsim \mu_{\rm cr} \approx 119\mu_{\rm v}$. As $\mu \gtrsim \mu_{\rm cr}$ corresponds to the sleeping-top regime with $\theta_p \ll 1$, the small values of $S_\perp \propto \sin\theta_p$ [see Eq. (4.66)] result in $\lambda_p \gg 1$ in this regime.

Nutation-Driven Resonance

Now we consider both precession and nutation of the neutrino gyroscope. The terms proportional to η in Eq. (4.48) contain the factors $\exp(i\omega_n t)$ and $\exp(-i\omega_n t)$, which correspond to rotation with angular velocities $\omega_n \hat{\mathbf{e}}_z^{\mathrm{I}}$ and $-\omega_n \hat{\mathbf{e}}_z^{\mathrm{I}}$, respectively, relative to Frame II. However, frames rotating with these angular velocities are not convenient to use because $\mu(t) S_\perp \hat{\mathbf{e}}_y^{\mathrm{II}}$, and hence $\mathbf{H}_{\mathrm{II}}$, rotate in such frames. To find the appropriate frames, we first consider Frame III with its axes defined by the unit vectors

$$\hat{\mathbf{e}}_x^{\mathrm{III}} = \hat{\mathbf{e}}_x^{\mathrm{II}}, \tag{4.72}$$

$$\hat{\mathbf{e}}_y^{\mathrm{III}} = \cos\delta \hat{\mathbf{e}}_y^{\mathrm{II}} + \sin\delta \hat{\mathbf{e}}_z^{\mathrm{I}}, \tag{4.73}$$

$$\hat{\mathbf{e}}_z^{\mathrm{III}} = \mathbf{H}_{\mathrm{II}}/|\mathbf{H}_{\mathrm{II}}|, \tag{4.74}$$

where

$$\cos\delta = \frac{\omega + \mu S_z - \dot{\phi}_p}{|\mathbf{H}_{\mathrm{II}}|}, \tag{4.75}$$

$$\sin\delta = -\frac{\mu S_\perp}{|\mathbf{H}_{\mathrm{II}}|}. \tag{4.76}$$

Note that just like Frame II, Frame III also rotates with an angular velocity $\dot{\phi}_p \hat{\mathbf{e}}_z^{\mathrm{I}}$ relative to Frame I. Using Eq. (4.48) we write $\mathbf{S}$ in Frame III as

$$\begin{aligned} \mathbf{S} &\approx S_z \hat{\mathbf{e}}_z^{\mathrm{I}} + S_\perp \hat{\mathbf{e}}_y^{\mathrm{II}} - \eta \frac{\dot{\phi}_p}{\mu} \sin\delta \cos(\omega_n t) \hat{\mathbf{e}}_z^{\mathrm{III}} \\ &+ \eta \frac{\dot{\phi}_p}{\mu} \frac{2\dot{\phi}_p - \mu S_z}{\omega_n} \sin(\omega_n t) \hat{\mathbf{e}}_x^{\mathrm{III}} + \eta \frac{\dot{\phi}_p}{\mu} \cos\delta \cos(\omega_n t) \hat{\mathbf{e}}_y^{\mathrm{III}}. \end{aligned} \tag{4.77}$$

The last two terms in the above expression can be rewritten as two vectors rotating with angular velocities $\omega_n \hat{\mathbf{e}}_z^{\mathrm{III}}$ and $-\omega_n \hat{\mathbf{e}}_z^{\mathrm{III}}$, respectively, relative to Frame III:

$$(S_x + iS_y')_{\mathrm{III}} \equiv i\frac{\eta}{2}\frac{\dot{\phi}_p}{\mu}\left[\left(\cos\delta - \frac{2\dot{\phi}_p - \mu S_z}{\omega_n}\right)\exp(i\omega_n t) + \left(\cos\delta + \frac{2\dot{\phi}_p - \mu S_z}{\omega_n}\right)\exp(-i\omega_n t)\right]. \tag{4.78}$$

As we will see shortly, a new resonance occurs for $|\mathbf{H}_{\mathrm{II}}| = \omega_n$. Using Eqs. (4.41), (4.42), (4.52), and (4.68), we can rewrite the above resonance condition as:

$$(\omega + \dot{\phi}_p)(\omega + 2\mu S_z - 3\dot{\phi}_p) = 0. \tag{4.79}$$

The term with the factor $\exp(-i\omega_n t)$ in Eq. (4.78) vanishes for $\omega = -\dot{\phi}_p$, while that with the factor $\exp(i\omega_n t)$ vanishes for $\omega = 3\dot{\phi}_p - 2\mu S_z$. We will see that the new resonance corresponds to $\omega = -\dot{\phi}_p$. So we can ignore the term with the factor $\exp(-i\omega_n t)$ in Eq. (4.78) when treating this resonance. We choose Frame IV to rotate with an angular velocity $\omega_n \hat{\mathbf{e}}_z^{\mathrm{III}}$ relative to Frame III. The term with the factor $\exp(i\omega_n t)$ in Eq. (4.78) represents a vector parallel to the unit vector $\hat{\mathbf{e}}_y^{\mathrm{IV}}$ in the y-direction of Frame IV. In this frame Eq. (4.64) effectively becomes

$$\frac{d}{dt}\mathbf{s}_\omega = \left[\left(|\mathbf{H}_{\mathrm{II}}| - \omega_n - \eta\dot{\phi}_p \sin\delta\cos\omega_n t\right)\hat{\mathbf{e}}_z^{\mathrm{III}} + \frac{\eta\dot{\phi}_p}{2}\left(\cos\delta - \frac{2\dot{\phi}_p - \mu S_z}{\omega_n}\right)\hat{\mathbf{e}}_y^{\mathrm{IV}}\right] \times \mathbf{s}_\omega. \tag{4.80}$$

It can be seen that a new resonance indeed occurs when $|\mathbf{H}_{\mathrm{II}}| = \omega_n$ if we ignore the small contribution proportional to η in the term associated with $\hat{\mathbf{e}}_z^{\mathrm{III}}$ in the above equation. The resonance condition relevant for Eq. (4.80) can be rewritten as

$$\omega = -\dot{\phi}_p(\mu_{\mathrm{res},n}), \tag{4.81}$$

where $\mu_{\mathrm{res},n}$ is the value of μ at resonance. We refer to this as the nutation-driven resonance as it is driven by the nutation-dependent component of $\mathbf{S}$. Using the neutrino gyroscope in Fig. 4.15, we show $\mu_{\mathrm{res},n}/\mu_{\mathrm{v}}$ as a function of ω/μ_{v} (dashed curve) in Fig. 4.17 (note again that the pure-precession solution gives essentially the same result).

To see that $\omega = 3\dot{\phi}_p - 2\mu S_z$, which also gives $|\mathbf{H}_{\mathrm{II}}| = \omega_n$, does not correspond to a resonance, we recall that the term with the factor $\exp(i\omega_n t)$ in Eq. (4.78) vanishes for this ω. We choose Frame V to rotate with an angular velocity $-\omega_n \hat{\mathbf{e}}_z^{\mathrm{III}}$ relative to Frame III and rewrite Eq. (4.64) in Frame V effectively as

$$\frac{d}{dt}\mathbf{s}_\omega = \left[\left(|\mathbf{H}_{\mathrm{II}}| + \omega_n - \eta\dot{\phi}_p \sin\delta\cos\omega_n t\right)\hat{\mathbf{e}}_z^{\mathrm{III}} + \frac{\eta\dot{\phi}_p}{2}\left(\cos\delta + \frac{2\dot{\phi}_p - \mu S_z}{\omega_n}\right)\hat{\mathbf{e}}_y^{\mathrm{V}}\right] \times \mathbf{s}_\omega, \tag{4.82}$$

where $\hat{\mathbf{e}}_y^{\mathrm{V}}$ is the unit vector in the y-direction of Frame V. It can be seen that the term associated with $\hat{\mathbf{e}}_z^{\mathrm{III}}$ in the above equation never vanishes, and consequently, there is no resonance for $\omega = 3\dot{\phi}_p - 2\mu S_z$.

The adiabaticity for evolution through the nutation-driven resonance can be discussed similarly to the case of precession-driven resonance studied previously. The evolution of $\mathbf{s}_\omega$ in Frame IV is governed by

$$\frac{d}{dt}\mathbf{s}_\omega = \mathbf{H}_{\rm IV} \times \mathbf{s}_\omega. \tag{4.83}$$

At resonance $\mathbf{H}_{\rm IV}$ is given by

$$(\mathbf{H}_{\rm IV})_{\rm res} \approx \eta\dot{\phi}_p \left(\frac{\mu S_z - 2\dot{\phi}_p}{\omega_n}\right) \hat{\mathbf{e}}_y^{\rm IV}. \tag{4.84}$$

We define the adiabaticity parameter for the nutation-driven resonance as

$$\lambda_n \equiv \frac{|\mathbf{H}_{\rm IV} \times d\mathbf{H}_{\rm IV}/dt|_{\rm res}}{|\mathbf{H}_{\rm IV}|^3_{\rm res}} \approx \frac{|d(|\mathbf{H}_{\rm II}| - \omega_n)/dt|_{\rm res}}{|\mathbf{H}_{\rm IV}|^2_{\rm res}}. \tag{4.85}$$

In Eqs.(4.84) and (4.85), we have neglected oscillatory terms proportional to η. Using the neutrino gyroscope in Fig. 4.15, we show λ_n as a function of $\mu/\mu_{\rm v}$ (dashed curve) in Fig. 4.18. It can be seen from this figure that evolution through the nutation-driven resonance is adiabatic at $110 > \mu/\mu_{\rm v} > 10$ and becomes non-adiabatic outside this range. In particular, evolution is extremely non-adiabatic at $\mu \gtrsim \mu_{\rm cr} \approx 119\mu_{\rm v}$ and at $\mu \lesssim 5\mu_{\rm v}$ as the very small nutation amplitude η (see Fig. 4.15) results in $\lambda_n \gg 1$ in these two regimes.

Evolution through Resonances Driven by the Neutrino Gyroscope

Based on the above discussions, an NFIS may experience two types of resonances driven by precession and nutation of the neutrino gyroscope, respectively. For the NFIS $\mathbf{s}_\omega$, a precession-driven resonance occurs at $\omega = \dot{\phi}_p(\mu_{{\rm res},p}) - \mu_{{\rm res},p}S_z$, and a nutation-driven resonance occurs at $\omega = -\dot{\phi}_p(\mu_{{\rm res},n})$. Formally these two resonances coincide at $\mu_{{\rm res},p} = \mu_{{\rm res},n} = \mu_{\rm cr}$ for $\omega = \omega_{\rm cr} \equiv -\dot{\phi}_{p,{\rm cr}} \approx (1+\sqrt{\alpha})\mu_{\rm v}/(1-\sqrt{\alpha})$ [see Eq. (4.62)]. Noting that $\dot{\phi}_p \to (1+\alpha)\mu_{\rm v}/(1-\alpha)$ at $\mu \gg \mu_{\rm cr}$ [see Eq. (4.55)] and $\dot{\phi}_p \to \mu_{\rm v}$ at $\mu \ll \mu_{\rm v}$ [see Eq. (4.58)], we introduce $\omega_A \equiv -(1+\alpha)\mu_{\rm v}/(1-\alpha)$, $\omega_B \equiv -\mu_{\rm v}$, and $\omega_C \equiv \mu_{\rm v}$ to define ranges of ω with different resonances. It turns out that for $\omega = \omega_D$ slightly larger

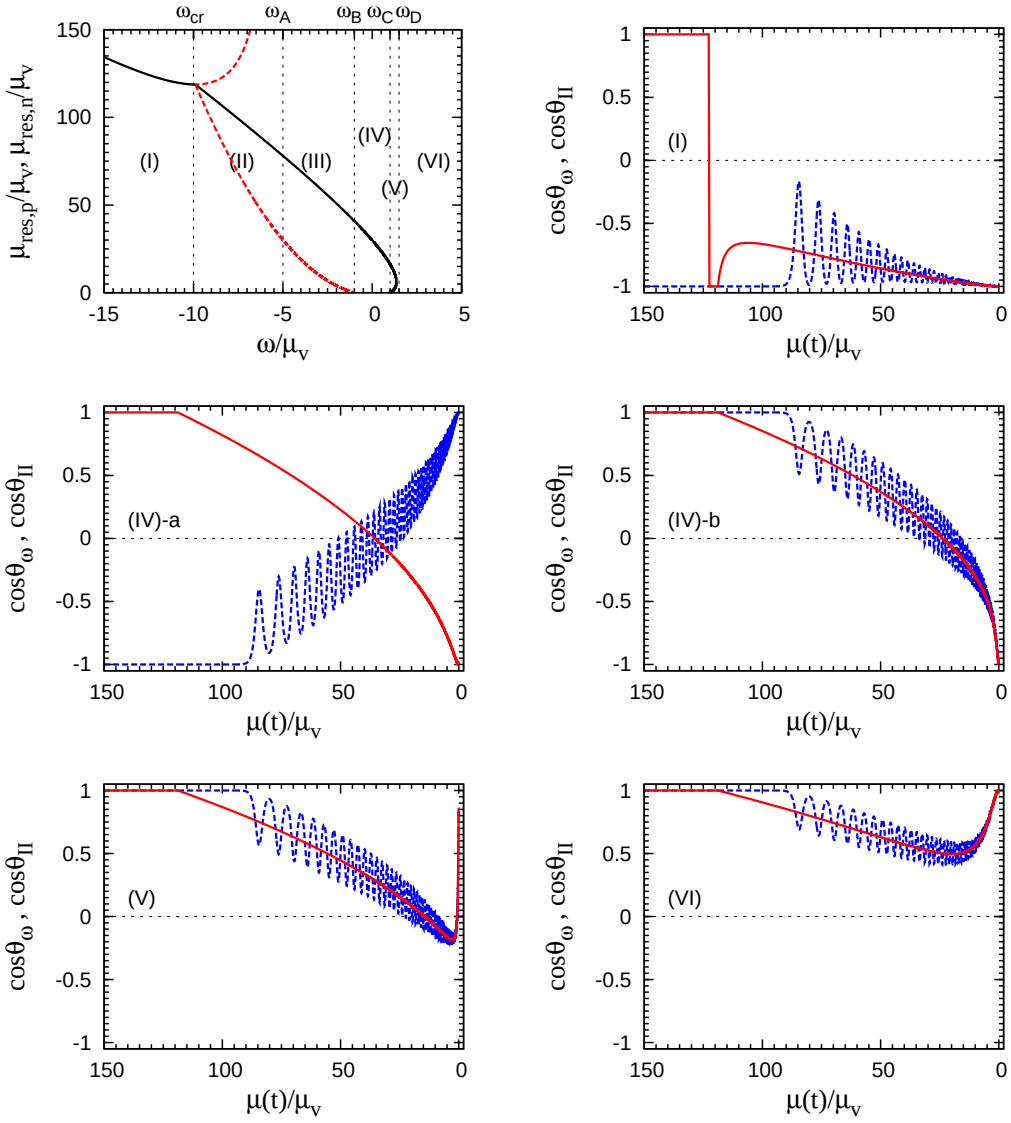

Figure 4.19: Ranges I–VI of ω based on occurrences of precession-driven (solid curve) and nutation-driven (dashed curve) resonances (top left panel) and example evolution of $\cos\theta_\omega$ (dashed curves) and $\cos\theta_{\rm II}$ (solid curves) as functions of $\mu(t)/\mu_{\rm v}$ for $\omega/\mu_{\rm v} = -12$ (I), -0.5 (IV-a), 0.5 (IV-b), 1.1 (V), and 3 (VI), respectively. See text for details.

than ω_C, there are two possible values for $\mu_{\mathrm{res},p}$. Altogether, the varieties of resonances experienced by $\mathbf{s}_\omega$ can be classified into six categories:

I. for $\omega < \omega_{\mathrm{cr}}$, $\mathbf{s}_\omega$ experiences only a precession-driven resonance at $\mu_{\mathrm{res},p} > \mu_{\mathrm{cr}}$;

II. for $\omega_{\mathrm{cr}} < \omega < \omega_A$, $\mathbf{s}_\omega$ experiences a nutation-driven resonance at $\mu_{\mathrm{res},n} > \mu_{\mathrm{cr}}$, then a precession-driven resonance at $\mu_{\mathrm{res},p} < \mu_{\mathrm{cr}}$, and finally a second nutation-driven resonance at $\mu'_{\mathrm{res},n} < \mu_{\mathrm{res},p}$;

III. for $\omega_A < \omega < \omega_B$, $\mathbf{s}_\omega$ experiences a precession-driven resonance at $\mu_{\mathrm{res},p} < \mu_{\mathrm{cr}}$ followed by a nutation-driven resonance at $\mu_{\mathrm{res},n} < \mu_{\mathrm{res},p}$;

IV. for $\omega_B < \omega < \omega_C$, $\mathbf{s}_\omega$ experiences only a precession-driven resonance at $\mu_{\mathrm{res},p} < \mu_{\mathrm{cr}}$;

V. for $\omega_C < \omega < \omega_D$, $\mathbf{s}_\omega$ experiences two precession-driven resonances at $\mu_{\mathrm{res},p} < \mu_{\mathrm{cr}}$ and $\mu'_{\mathrm{res},p} < \mu_{\mathrm{res},p}$, respectively.

VI. for $\omega > \omega_D$, $\mathbf{s}_\omega$ does not experience any resonance.

For the neutrino gyroscope in Fig. 4.15, $\mu_{\mathrm{cr}} \approx 119\mu_{\mathrm{v}}$, $\omega_{\mathrm{cr}} \approx -10\mu_{\mathrm{v}}$, $\omega_A \approx -5\mu_{\mathrm{v}}$, and $\omega_D \approx 1.5\mu_{\mathrm{v}}$. The six categories of resonances for this example are shown in the top left panel of Fig. 4.19.

Only precession-driven resonances are involved for ω in ranges I, IV, and V, and there are no resonances for ω in range VI. We first consider the overall evolution of $\mathbf{s}_\omega$ for ω in these ranges using the neutrino gyroscope in Fig. 4.15. As nutation is unimportant for these cases, we focus on $\mathbf{H}_{\mathrm{II}}$ as the net effective field interacting with $\mathbf{s}_\omega$ [see Eq. (4.68)]. At $\mu = \mu(0) \gg \mu_{\mathrm{cr}}$, $\mathbf{H}_{\mathrm{II}}$ is essentially in the direction of $\hat{\mathbf{e}}_z^{\mathrm{I}}$ and $\mathbf{s}_\omega$ is either aligned (initial ν_e, $\omega > 0$) or anti-aligned (initial $\bar{\nu}_e$, $\omega < 0$) with $\mathbf{H}_{\mathrm{II}}$. We show the subsequent evolution of $\mathbf{s}_\omega$ relative to $\mathbf{H}_{\mathrm{II}}$ by comparing $\cos\theta_\omega \equiv \mathbf{s}_\omega \cdot \hat{\mathbf{e}}_z^{\mathrm{I}}/|\mathbf{s}_\omega|$ (dashed curve) with $\cos\theta_{\mathrm{II}} \equiv \mathbf{H}_{\mathrm{II}} \cdot \hat{\mathbf{e}}_z^{\mathrm{I}}/|\mathbf{H}_{\mathrm{II}}|$ (solid curve) in Fig. 4.19. For $\omega/\mu_{\mathrm{v}} = -12$ in range I, $\mathbf{s}_\omega$ is initially anti-aligned with $\mathbf{H}_{\mathrm{II}}$ ($\cos\theta_\omega \approx -1$ but $\cos\theta_{\mathrm{II}} \approx 1$). At $\mu/\mu_{\mathrm{v}} \approx 122$, $\cos\theta_{\mathrm{II}}$ vanishes and a resonance occurs. However, evolution through this resonance is extremely

non-adiabatic (see Fig. 4.18). Consequently, $\cos\theta_\omega$ is unaffected while $\cos\theta_{\rm II}$ changes drastically from ≈ 1 to ≈ -1 immediately after the resonance. Subsequent evolution of $\mathbf{s}_\omega$ is essentially adiabatic with $\cos\theta_\omega$ oscillating around $\cos\theta_{\rm II}$ and eventually settling to ≈ -1 again. This kind of evolution applies to all ω in range I, for which there is no net flavor transformation. For $\omega/\mu_{\rm v} = -0.5$ (0.5) in range IV, there is a resonance at $\mu/\mu_{\rm v} \approx 36$ (24). Evolution through the resonance is adiabatic (see Fig. 4.18) and $\mathbf{s}_\omega$ stays anti-aligned (aligned) with $\mathbf{H}_{\rm II}$ during the entire evolution. As the initial and final directions of $\mathbf{H}_{\rm II}$ are opposite, there is full flavor conversion for ω in range IV. For $\omega/\mu_{\rm v} = 1.1$ in range V, there are two resonances at $\mu/\mu_{\rm v} \approx 14$ and 1, respectively. Evolution through both resonances is essentially adiabatic (see Fig. 4.18) and $\mathbf{s}_\omega$ stays aligned with $\mathbf{H}_{\rm II}$ during the entire evolution. As $\cos\theta_{\rm II}$ changes sign twice, the initial and final directions of $\mathbf{H}_{\rm II}$ are the same and there is no net flavor transformation for ω in range V. Finally, for $\omega/\mu_{\rm v} = 3$ in range VI, there is no resonance and evolution is adiabatic. So $\cos\theta_\omega$ oscillates around $\cos\theta_{\rm II}$, indicating that $\mathbf{s}_\omega$ is always aligned with $\mathbf{H}_{\rm II}$. There is no net flavor transformation for ω in range VI.

Resonances driven by both precession and nutation of the neutrino gyroscope are involved for ω in ranges II and III. We discuss the evolution of $\mathbf{s}_\omega$ for these ranges using $\mathbf{H}_{\rm IV}$ as the net effective field. We define $\cos\theta_{\rm IV} \equiv \mathbf{H}_{\rm IV}\cdot\hat{\mathbf{e}}_z^{\rm I}/|\mathbf{H}_{\rm IV}|$. Neglecting terms proportional to η, we obtain $\cos\theta_{\rm IV} \approx {\rm sgn}(|\mathbf{H}_{\rm II}| - \omega_n)\cos\theta_{\rm II}$, where ${\rm sgn}(x)$ is the sign of x. Using the neutrino gyroscope in Fig. 4.15, we compare the evolution of $\cos\theta_\omega$ and $\cos\theta_{\rm IV}$ for ω in ranges II and III in Fig. 4.20. For $\omega/\mu_{\rm v} = -6$ in range II, $\mathbf{s}_\omega$ is initially aligned with $\mathbf{H}_{\rm IV}$. A nutation-driven resonance occurs at $\mu/\mu_{\rm v} \approx 210$. However, evolution through this resonance is extremely non-adiabatic (see Fig. 4.18). So $\cos\theta_\omega$ is unaffected although $\cos\theta_{\rm IV}$ jumps from ≈ -1 to ≈ 1 immediately after the resonance. Then $\cos\theta_{\rm IV}$ vanishes at $\mu/\mu_{\rm v} \approx 99$ corresponding to $\omega = 3\dot{\phi}_p - 2\mu S_z$ and $|\mathbf{H}_{\rm II}| = \omega_n$, but this is not a resonance. A precession-driven resonance occurs at $\mu/\mu_{\rm v} \approx 86$ and a second nutation-driven resonance occurs at $\mu/\mu_{\rm v} \approx 43$. Evolution through both these resonances is adiabatic (see Fig. 4.18). Consequently, at $\mu/\mu_{\rm v} < 99$, $\cos\theta_\omega$ oscillate

around $\cos\theta_{\rm IV}$, eventually settling to ≈ -1 again. There is no net flavor transformation for ω in range II. For $\omega/\mu_{\rm v} = -4$ in range III, $\cos\theta_{\rm IV}$ vanishes at $\mu/\mu_{\rm v} \approx 89$, which is not a resonance. A precession-driven resonance occurs at at $\mu/\mu_{\rm v} \approx 69$ and a nutation-driven resonance occurs at $\mu/\mu_{\rm v} \approx 19$. Evolution is adiabatic throughout and there is no net flavor transformation. For $\omega/\mu_{\rm v} = -2$ also in range III, the evolution of $\cos\theta_{\rm IV}$ is similar to that for $\omega/\mu_{\rm v} = -4$. However, for $\omega/\mu_{\rm v} = -2$, evolution through the precession-driven resonance at $\mu/\mu_{\rm v} \approx 51$ is adiabatic while that through the nutation-driven resonance at $\mu/\mu_{\rm v} \approx 4$ is non-adiabtic (see Fig. 4.18). This kind of evolution applies to $-3 < \omega/\mu_{\rm v} < -1$ and results in significant flavor transformation.

In summary, evolution of $\mathbf{s}_\omega$ can be understood in terms of the resonances it experiences. A resonance does not affect the net flavor transformation if evolution through it is very non-adiabatic. Net full flavor conversion results from adiabatic evolution through an odd number of resonances while little net flavor transformation results from adiabatic evolution through an even number (including zero) of resonances. Note that the evolution through a resonance driven by either precession or nutation at $\mu > \mu_{\rm cr}$ is extremely non-adiabatic. In contrast, evolution through a precession-driven resonance at $\mu < \mu_{\rm cr}$ is essentially always adiabatic. On the other hand, evolution through a nutation-driven resonance at $\mu_{\rm tr} < \mu < \mu_{\rm cr}$ is adiabatic, but one at $\mu < \mu_{\rm tr}$ is non-adiabatic. We choose $\mu_{\rm tr}$ to correspond to an adiabaticity parameter $\lambda_n = 0.5$. For the neutrino gyroscope in Fig. 4.15, $\mu_{\rm tr} \approx 12\mu_{\rm v}$ and $\mathbf{s}_\omega$ with $\omega \approx -3\mu_{\rm v}$ goes through a nutation-driven resonance at $\mu = \mu_{\rm tr}$ (see Figs. 4.17 and 4.18). Based on the above discussion and the occurrences of resonances shown in Figs. 4.19 and 4.20, the swap factor shown as the dashed curve in Fig. 4.13 can be understood (see also discussion of Fig. 4.21).

Application to System of Neutrinos with Continuous Spectra

As discussed in Sec. 4.2.1, the total angular momentum of the neutrino gyroscope, which we denote as $\mathbf{S}^{(0)}$ again for clarity, approximates the mean field $\mathbf{S}$ of the NFIS's in the system of neutrinos with continuous spectra as specified in Sec. 4.2.1. The oscillations

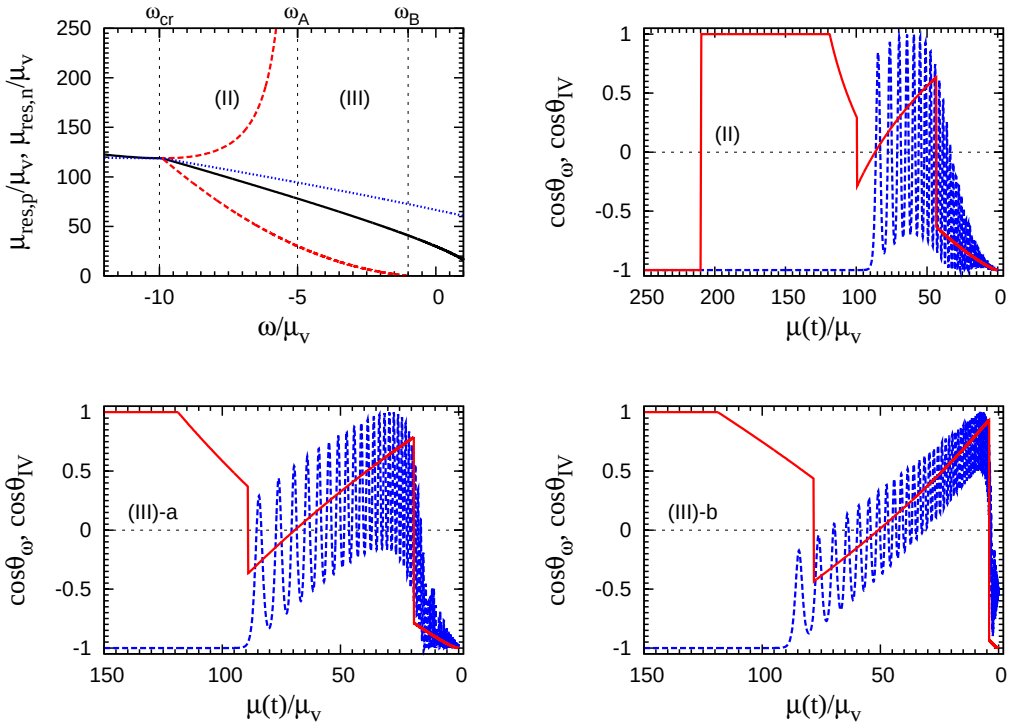

Figure 4.20: Ranges II and III of ω based on occurrences of precession-driven (solid curve) and nutation-driven (dashed curve) resonances (top left panel) and example evolution of $\cos\theta_\omega$ (dashed curves) and $\cos\theta_{\rm IV}$ (solid curves) as functions of $\mu(t)/\mu_{\rm v}$ for $\omega/\mu_{\rm v} = -6$ (II), -4 (III-a), and -2 (III-b), respectively. The dotted curve in the top left panel shows the value of $\mu/\mu_{\rm v}$ for which $\omega = 3\dot{\phi}_p - 2\mu S_z$ as a function of $\omega/\mu_{\rm v}$. Note that no resonance occurs at this μ although the corresponding $\cos\theta_{\rm IV}$ vanishes. See text for details.

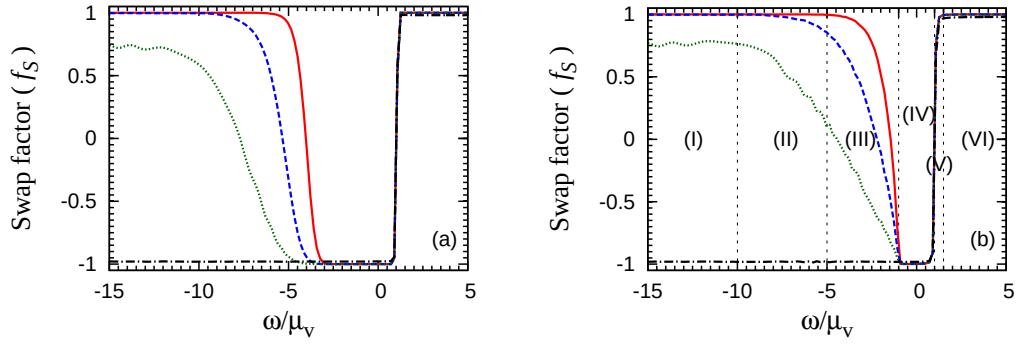

Figure 4.21: Comparison of the swap factors $f_S(\omega, t)$ (a) and $f_S^{(0)}(\omega, t)$ (b) at $r = 250$ km for the system initially consisting of ν_e and $\bar{\nu}_e$ only as in Fig. 4.13. The solid, dashed, dotted, and dot-dashed curves are for $\tilde{\theta}_{\rm v} = 10^{-5}$, 10^{-3}, 10^{-2}, and 10^{-1}, respectively. Ranges I-VI of ω shown in (b) are based on occurrences of precession-driven and nutation-driven resonances (calculated for $\tilde{\theta}_{\rm v} = 10^{-5}$ but valid for $\tilde{\theta}_{\rm v} \ll 1$).

of $S_\perp^{(0)}$ and $S_\perp$ shown in Fig. 4.12 reflect the nutation of the gyroscope. It can be seen from this figure that large deviations of $\mathbf{S}^{(0)}$ from $\mathbf{S}$ occur only at $\mu/\mu_{\rm v} < 20$, where the nutation amplitude of $\mathbf{S}$ rapidly decreases. In addition, $S_\perp$ sharply drops at $\mu/\mu_{\rm v} < 2$. The small nutation amplitude of $\mathbf{S}$ at $\mu/\mu_{\rm v} < 20$ affects the adiabaticity of evolution through the nutation-driven resonance for ω in range III (see Fig. 4.19). In fact, the evolution is extremely non-adiabatic for $-3 < \omega/\mu_{\rm v} < -1$. On the other hand, evolution through the precession-driven resonance is adiabatic for these values of ω, which results in net full flavor conversion. Thus, compared with the results based on $\mathbf{S}^{(0)}$, the swap factor is ≈ -1 for a wider range of ω as shown by the solid curve in Fig. 4.21a. In principle, the sharp decrease of $S_\perp$ at $\mu/\mu_{\rm v} < 2$ could affect the adiabaticity of evolution through the precession-driven resonance at the lower μ for ω in range V (see Fig. 4.19). However, in practice this has little effect (see the solid curve in Fig. 4.21a) as resonances at such low values of μ only occur for a very narrow range of ω and adiabaticity is affected for an even narrower range of ω.

To further illustrate how adiabaticity of evolution through precession-driven and nutation-driven resonances affect net flavor transformation, we increase $\tilde{\theta}_{\rm v}$ from 10^{-5} to 10^{-3}, 10^{-2}, and 10^{-1}, respectively. For a larger $\tilde{\theta}_{\rm v}$, $S_\perp$ in the "sleeping-top" regime of $\mu > \mu_{\rm cr}$ is larger as the initial θ_p of the neutrino gyroscope becomes larger [see Eq. (4.66) and Appendix A.2]. On the other hand, the nutation amplitude η is smaller at $\mu < \mu_{\rm cr}$ as it grows less at $\mu \sim \mu_{\rm cr}$ due to a shorter nutation period $\sim 2\pi/\omega_{n,{\rm cr}}$ for a larger $\tilde{\theta}_{\rm v}$ [see Eq. (4.63)]. Consequently, evolution through a precession-driven resonance at $\mu > \mu_{\rm cr}$ becomes less non-adiabatic while that through a nutation-driven resonance at $\mu < \mu_{\rm cr}$ becomes more non-adiabatic. The former effect becomes quite large for $\tilde{\theta}_{\rm v} = 10^{-2}$ as partial flavor conversion occurs for ω in range I (dotted curves in Fig. 4.21), while the latter effect is already significant for $\tilde{\theta}_{\rm v} = 10^{-3}$ as more flavor transformation occurs for ω in ranges II and III. For $\tilde{\theta}_{\rm v} = 10^{-1}$, $S_\perp$ is sufficiently large initially and η remains small at all μ. Consequently, evolution through precession-driven resonances is adiabatic for ω in ranges I to V while nutation-driven resonances have no effect on the net flavor transformation. This can be seen from the dot-dashed curves in Fig. 4.21, which show that net full flavor conversion occurs for ω in ranges I to IV with a single precession-driven resonance but there is no net flavor transformation for ω in ranges V and VI with two and zero precession-driven resonances, respectively.

4.2.4 Collective Neutrino Oscillations in Supernovae

In this section we consider the system of neutrinos exhibiting the spectral swaps shown in Figs. 4.8 and 4.9. As described at the beginning of this section, this system initially consists of ν_e, $\bar{\nu}_e$, ν_x, and $\bar{\nu}_x$ with continuous spectra. In addition, the initial number densities of ν_e and $\bar{\nu}_e$ are significantly larger than those of ν_x and $\bar{\nu}_x$. We first show that the swap factor shown in Fig. 4.9 can be understood in terms of the six different kinds of flavor evolution that have been discussed in Secs. 4.2.3 for the system initially consisting of ν_e and $\bar{\nu}_e$ only. The evolution of $\cos\theta_\omega$ corresponding to Fig. 4.9 is shown in Fig. 4.22 for $2\omega/\delta m^2 = -0.90$, -0.50, -0.32, 0.02, 0.14, and 0.50 MeV^{-1}, respectively. It can be

seen that these six kinds of evolution are very similar to those shown in Figs. 4.19 and 4.20 for the six ranges of ω discussed in Secs. 4.2.3. As the comparison of $\mathbf{S}^{(0)}$ and $\mathbf{S}$ shown in Fig. 4.11 for the system of four initial neutrino species is similar to that shown in Fig. 4.12 for the system of two initial neutrino species, the differences between the evolution based on $\mathbf{S}^{(0)}$ and $\mathbf{S}$ are also similar to those discussed in Sec. 4.2.3. Therefore, we conclude that the flavor evolution of a system with initial number densities of ν_e and $\bar{\nu}_e$ significantly larger than those of ν_x and $\bar{\nu}_x$ can be understood in terms of the resonances driven by precession and nutation of a neutrino gyroscope.

Next we consider the flavor evolution of the system exhibiting the spectral swaps in Figs. 4.8 and 4.9 by relaxing the single-angle approximation used to produce these results. In the multi-angle approximation as discussed in Sec. 3.3 in detail, neutrinos are emitted from the neutrino sphere with equal probability in the forward directions, which are defined to be $0 \leq \theta_{\rm em} \leq \pi/2$. Here $\theta_{\rm em}$ is the angle with respect to the radial direction at the point of emission. Under the multi-angle approximation, an NFIS can be specified by the corresponding neutrino energy and emission angle in terms of ω and $\epsilon \equiv \cos\theta_{\rm em}$. The evolution of $\mathbf{s}_{\omega,\epsilon}$ is governed by

$$\frac{d}{dr}\mathbf{s}_{\omega,\epsilon} = \mathbf{s}_{\omega,\epsilon} \times \left\{ \frac{\omega}{D_\epsilon(r)}\mathbf{H}_{\rm v} - 2\mu(R_\nu)\frac{R_\nu^2}{r^2}\int_{-\infty}^{\infty} g(\omega')d\omega' \int_0^1 \mathbf{s}_{\omega',\epsilon'}\left[\frac{1}{D_\epsilon(r)D_{\epsilon'}(r)} - 1\right]\epsilon' d\epsilon' \right\}, \tag{4.86}$$

where $D_\epsilon(r) \equiv \sqrt{1-(1-\epsilon^2)R_\nu^2/r^2}$.

Using the same neutrino emission parameters as for Figs. 4.8 and 4.9, we follow the flavor evolution of the system with initial number densities of ν_e and $\bar{\nu}_e$ significantly larger than those of ν_x and $\bar{\nu}_x$ under the multi-angle approximation. The angle-averaged swap factor $\langle f_S(\omega,\epsilon,r)\rangle_\epsilon$ at $r = r_f = 250$ km is shown as a function of $2\omega/\delta m^2$ in Fig. 4.23a. This average factor is defined as

$$\langle f_S(\omega,\epsilon,r)\rangle_\epsilon \equiv \frac{\int_0^1 f_S(\omega,\epsilon,r)[\epsilon/D_\epsilon(r)]d\epsilon}{\int_0^1 [\epsilon/D_\epsilon(r)]d\epsilon} = \frac{\int_0^1 f_S(\omega,\epsilon,r)[\epsilon/D_\epsilon(r)]d\epsilon}{\left[1-\sqrt{1-R_\nu^2/r^2}\right]r^2/R_\nu^2}, \tag{4.87}$$

and can be used to calculate the effect of flavor transformation on e.g., neutrino reaction rates at radius r. Compared with the swap factor shown in Fig. 4.9 for the single-angle

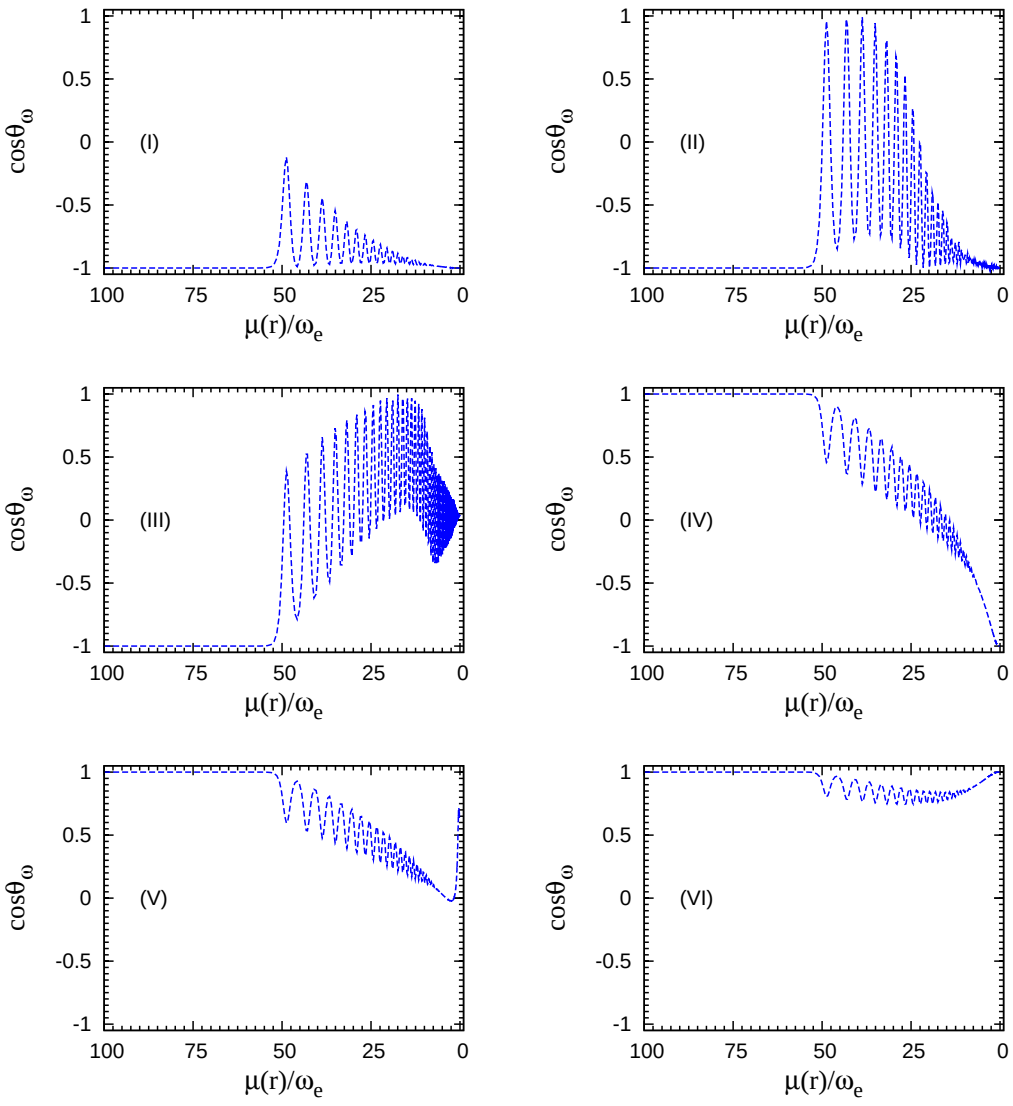

Figure 4.22: Example evolution of $\cos\theta_\omega$ as a function of $\mu(r)/\omega_e$ for the system shown in Figs. 4.8 and 4.9 for $2\omega/\delta m^2 = -0.90$ (I), -0.50 (II), -0.32 (III), 0.02 (IV), 0.14 (V), and 0.50 (VI) MeV^{-1}, respectively. Note the similarity to the evolution shown in Figs. 4.19 and 4.20 for the six ranges of ω based on occurrences of precession-driven and nutation-driven resonances.

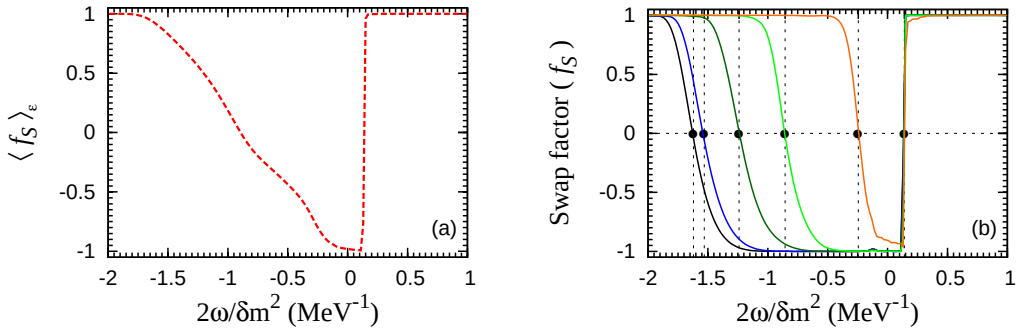

Figure 4.23: Angle-averaged swap factor $\langle f_S(\omega, \epsilon, r_f)\rangle_\epsilon$ (a) and angle-specific swap factors $f_S(\omega, \epsilon, r_f)$ (b) at $r_f = 250$ km for the system with the same neutrino emission parameters as for Fig. 4.9 but in multi-angle approximation. From left to right, the curves for $\omega < 0$ in (b) are for $\epsilon = 10^{-3}$, 0.24, 0.49, 0.74, and 0.99, respectively. The sharp changes in $f_S(\omega, \epsilon, r_f)$ occur at $2\omega/\delta m^2 = -1.63$, -1.54, -1.24, -0.86, -0.24, and 0.14 MeV^{-1}, respectively, for which $f_S(\omega, \epsilon, r_f) = 0$ (filled circles).

approximation, $\langle f_S(\omega, \epsilon, r_f)\rangle_\epsilon$ is identical for $\omega > 0$ but shows large deviations for $\omega < 0$. On the other hand, swap factors $f_S(\omega, \epsilon, r_f)$ for specific values of ϵ shown in Fig. 4.23b have the same general structure as shown in Fig. 4.9. This can be understood from the precession-driven resonance as discussed below.

It is convenient to define

$$\mathbf{S}_a \equiv \int_{-\infty}^{\infty} g(\omega) d\omega \int_0^1 \mathbf{s}_{\omega,\epsilon} \epsilon d\epsilon, \tag{4.88}$$

$$\mathbf{S}_b \equiv \int_{-\infty}^{\infty} g(\omega) d\omega \int_0^1 \mathbf{s}_{\omega,\epsilon} \left[\frac{\epsilon}{D_\epsilon(r)}\right] d\epsilon, \tag{4.89}$$

and rewrite Eq. (4.86) as

$$\frac{d}{dr}\mathbf{s}_{\omega,\epsilon} = \mathbf{s}_{\omega,\epsilon} \times \left\{ \frac{\omega}{D_\epsilon(r)}\mathbf{H}_{\rm v} - 2\mu(R_\nu)\frac{R_\nu^2}{r^2}\left[\frac{\mathbf{S}_b}{D_\epsilon(r)} - \mathbf{S}_a\right]\right\}. \tag{4.90}$$

Our numerical results show that both $\mathbf{S}_a$ and $\mathbf{S}_b$ precess around $\mathbf{H}_{\rm v}$ with the same frequency $\dot{\phi}_p(r)$ at a specific r for $R_\nu \le r \lesssim r_f$. This is consistent with the conclusions of [66] based on symmetry arguments. The synchronized oscillations of $S_{a,x}/S_{a,\perp}$ and

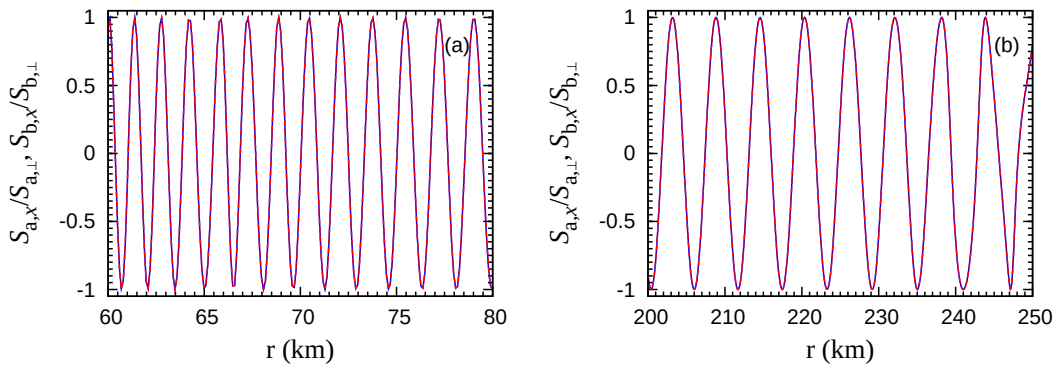

Figure 4.24: Synchronized oscillations of $S_{a,x}/S_{a,\perp}$ and $S_{b,x}/S_{b,\perp}$ due to precession for the system shown in Fig. 4.23 for $r = 60$–80 (a) and 200–250 km (b). In either panel two curves are shown but they are indistinguishable.

$S_{b,x}/S_{b,\perp}$ due to precession are shown for $r = 60$–80 and 200–250 km in Figs. 4.24a and b, respectively. Here the x-axis is in the plane perpendicular to $\mathbf{H}_{\rm v}$ and the subscript "$\perp$" denotes the net perpendicular component. It can be shown from Eq. (4.90) that $S_{a,z} \equiv \mathbf{S}_a \cdot \hat{\mathbf{e}}_z^{\rm I}$ ($\hat{\mathbf{e}}_z^{\rm I} = -\mathbf{H}_{\rm v}$) is conserved (see Fig. 4.25a). Components of the "mean field" $\mathbf{S}_b/D_\epsilon(r) - \mathbf{S}_a$ are shown as functions of r for $\epsilon = 0$ (solid curve) and 1 (dashed curve) in Figs. 4.25b and c. Clearly, the mean field experienced by $\mathbf{s}_{\omega,\epsilon}$ is different for different ϵ. It can also be seen from Fig. 4.25c that the perpendicular component $S_{b,\perp}/D_\epsilon(r) - S_{a,\perp}$ increases sharply at $r_{\rm cr} \approx 64$ km just as $S_\perp$ does at the critical point in the single-angle approximation (see Fig. 4.11). However, in contrast to the single-angle approximation, nutation of the mean field is damped out very quickly in the mutli-angle approximation, and therefore, can be neglected.

Based on the above discussion, we only need to consider the precession-driven resonance in explaining the swap factor $f_S(\omega, \epsilon, r_f)$. A precession-driven resonance occurs when the z-component of the net effective field interacting with $\mathbf{s}_{\omega,\epsilon}$ vanishes in the co-precessing frame (see Sec. 4.2.3). It can be seen from Eq. (4.90) that $\mathbf{s}_{\omega,\epsilon}$ goes through

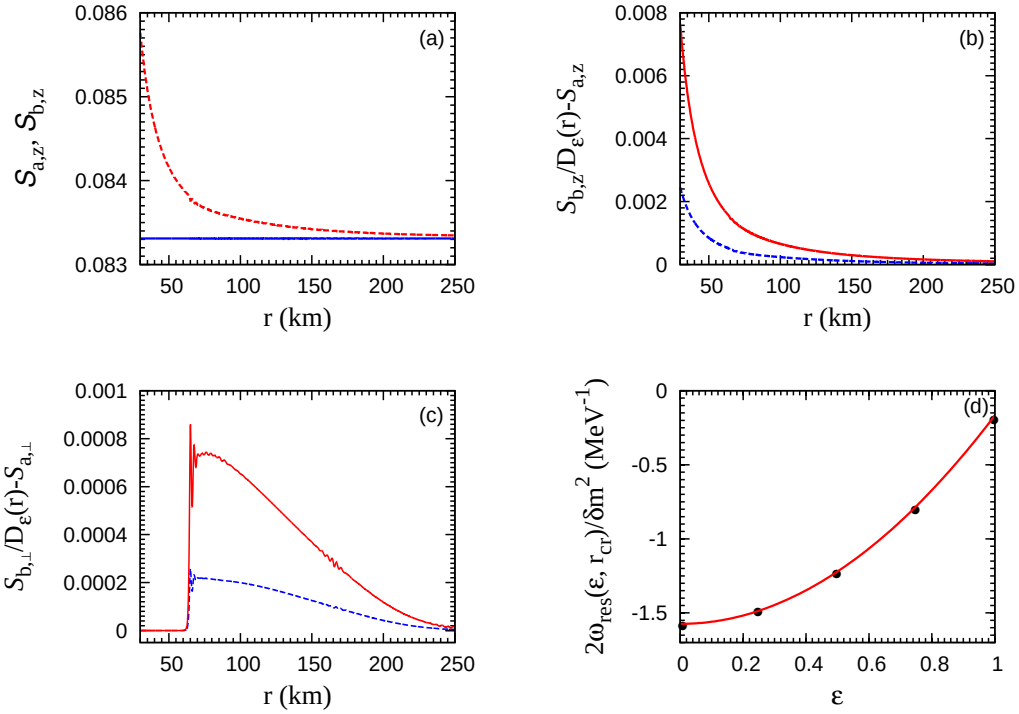

Figure 4.25: Components of the mean field as functions of r: (a) S_a (solid curve) and S_b (dashed curve), (b) $S_{b,z}/D_\epsilon(r) - S_{a,z}$ for $\epsilon = 0$ (solid curve) and 1 (dashed curve), and (c) $S_{b,\perp}/D_\epsilon(r) - S_{a,\perp}$ for $\epsilon = 0$ (solid curve) and 1 (dashed curve). (d) The value of $2\omega_{\rm res}(\epsilon, r_{\rm cr})/\delta m^2$ at $r_{\rm cr} \approx 64$ km shown as a function of ϵ. From left to right, the filled circles correspond to $2\omega_{\rm res}(\epsilon, r_{\rm cr})/\delta m^2 \approx -1.57$, -1.50, -1.24, -0.81, and -0.21 MeV^{-1}, respectively. These values are very close to those values of $2\omega/\delta m^2$ that correspond to the filled circles at $\omega < 0$ in Fig. 4.23b.

a precession-driven resonance when

$$\omega = \omega_{\rm res}(\epsilon, r) \equiv D_\epsilon(r) \left\{ \dot{\phi}_p(r) - 2\mu(R_\nu) \frac{R_\nu^2}{r^2} \left[\frac{S_{b,z}}{D_\epsilon(r)} - S_{a,z} \right] \right\}. \tag{4.91}$$

However, evolution through a resonance at $r < r_{\rm cr}$ is extremely non-adiabatic and does not result in any net flavor transformation. Thus, we expect that net full conversion $[f_S(\omega, \epsilon, r_f) = -1]$ occurs only for $\omega_{\rm res}(\epsilon, r_{\rm cr}) < \omega < \omega_{\rm res}(\epsilon, r_f)$. At $r = r_{\rm cr}$, $\omega_{\rm res}(\epsilon, r_{\rm cr}) < 0$ for $0 \leq \epsilon \leq 1$ and is larger for a larger ϵ (more radial trajectory, see Fig. 4.25d). At $r = r_f$, $D_\epsilon(r) \approx 1$ and $S_{b,z}/D_\epsilon(r) - S_{a,z}$ becomes very small (see Fig. 4.25b), so $\omega_{\rm res}(\epsilon, r_f) \approx \dot{\phi}_p(r_f)$ and is nearly independent of ϵ. Using our numerical results for $\dot{\phi}_p(r)$, $S_{a,z}$, and $S_{b,z}$, we obtain $2\omega_{\rm res}(\epsilon, r_{\rm cr})/\delta m^2 \approx -1.57$, -1.50, -1.24, -0.81, and -0.21 MeV^{-1} for $\epsilon = 10^{-3}$, 0.24, 0.49, 0.74, and 0.99, respectively, and $2\omega_{\rm res}(\epsilon, r_f)/\delta m^2 \approx 0.14$ MeV^{-1} for $0 \leq \epsilon \leq 1$. These results are in excellent agreement with Figure 4.23b.

4.2.5 Discussions

Using a system initially consisting of ν_e and $\bar{\nu}_e$ with the same energy spectrum but different number densities, we have shown that flavor evolution of this system in the single-angle approximation can be understood in terms of the response of the individual NFIS to the mean field, which is very well approximated by the total angular momentum of a neutrino gyroscope. The evolution of an NFIS is governed by two types of resonances driven by precession and nutation of the gyroscope, respectively. A resonance does not affect the net flavor transformation if evolution through it is extremely non-adiabatic. Nearly full flavor conversion occurs following adiabatic evolution through an odd number of resonances but there is no net flavor transformation following adiabatic evolution through an even number (including zero) of resonances. The detailed results on NFIS evolution are presented in Figs. 4.19, 4.20, and 4.21, and discussed in Secs. 4.2.3.

We have also shown that the above results for the system of two initial neutrino species can be extended to a system of four species with the initial number densities of ν_e and $\bar{\nu}_e$ significantly larger than those of ν_x and $\bar{\nu}_x$. Further, we find that when

the multi-angle approximation is adopted instead of the single-angle approximation, nutation of the mean field is quickly damped out and can be neglected. In contrast, precession-driven resonances still govern the evolution of NFIS's with different energy and emission angles just as in the single-angle approximation. These results are presented and discussed in Sec. 4.2.4.

In sum, we have presented a detailed pedagogically and analytically analysis of collective neutrino oscillations in supernovae for the case where the initial number densities of ν_e and $\bar{\nu}_e$ are significantly larger than those of ν_x and $\bar{\nu}_x$. Other studies such as [67], [42] and [37] also address this issue but have used different approaches.

Note again that here we assume the electron density n_e is low enough such that the multi-angle matter suppression effect [26, 27, 62] will not happen. Recent supernova simulations suggest that the matter density is so high such that it may completely suppress the collective neutrino oscillations during the accretion phase. However, a more self-consistent study needs to be performed to include the contribution from the "neutrino halo" [31], which is due to neutrinos that undergo inelastic scatterings from high and flat density profile, to rule out the possibility of occurrence of collective oscillations between the proto-neutron star and the standing shock.

4.3 Neutrino Flavor Instability

From previous sections, we see that there is basically no flavor oscillation happened in the large λ and μ limit except for tiny nutation around the pure-precession solution. However, it was firstly shown in [68] that large flavor oscillations can happen in high density limit in a specifically symmetric case under the single-angle approximation. Shortly after [68], it was shown that a similar behavior such that large flavor oscillations could happen very close to the neutrino sphere using the neutrino spectra that represents the neutrino emission during the cooling phase [35]. This early onset of the "flavor instability" might have interesting consequence if it really occurs in nature.

In this section, we briefly discuss the origin of this instability. We find that it is because the "pure-precession" solution may not be stable in simple systems with more than two NFIS's. We further show that a three-NFIS system which represents the zeroth-order mean field of the cooling phase spectra in high density is equivalent to an effective two-spin system in low density after the instability has occurred. This equivalence allows the three-NFIS system to have large flavor oscillations in the high density limit. At last, we discuss the multi-angle suppression of this early instability and the need of numerical exploration as a summary.

4.3.1 Instability of Pure-precession Solution in Synchronization Limit

Using the single-angle approximation under the two-flavor mixing scenario, the flavor evolution of an NFIS $\mathbf{s}_i$ with energy E_i and number density n_i is governed by the following equation in the discretized form :

$$\frac{d}{dt}\mathbf{s}_i = \mathbf{s}_i \times (\omega_i \mathbf{H}_{\rm v} - \sum_j \mu_j \mathbf{s}_j), \tag{4.92}$$

$$\equiv \mathbf{s}_i \times (\omega \gamma_i \mathbf{H}_{\rm v} - \mu \sum_j \alpha_j \mathbf{s}_j). \tag{4.93}$$

We here recap the convention used in the above equations : $\omega_i \equiv \frac{|\delta m^2|}{\pm 2E_i}$, where $+/-$ is for a neutrino/antineutrino, $\mu_i \equiv 2\sqrt{2}G_F n_i$ and $\mathbf{s}_i = \hat{\mathbf{e}}^{\rm f}_z/2(-\hat{\mathbf{e}}^{\rm f}_z/2)$ for a ν_e or $\bar{\nu}_x(\nu_x$ or $\bar{\nu}_e)$. For a small vacuum mixing angle $\theta_{\rm v} \ll 1$, $\mathbf{H}_{\rm v} = -\sin 2\theta_{\rm v}\hat{\mathbf{e}}^{\rm f}_x \pm \cos 2\theta_{\rm v}\hat{\mathbf{e}}^{\rm f}_z$ where $+/-$ is for NH/IH. In equation (4.93), we arbitrarily define $\omega_i \equiv \omega$ and $\mu_i \equiv \mu$ for a specific $\mathbf{s}_i$, and define $\gamma_j \equiv \omega_j/\omega$ and $\alpha_j \equiv \mu_j/\mu$ for all $\mathbf{s}_j$ correspondingly. Note that we ignore the matter density completely since it can be rotated away by adopting an effective vacuum mixing angles in the single-angle approximation [24].

Because the value of ω can be effectively shifted by introducing the "co-rotating frame" which rotates around $\mathbf{H}_{\rm v}$ as used in previous sections without changing physical consequences, we can always find a pair of $\mathbf{s}_i$ such that $\gamma_i = \pm 1$ by choosing an

appropriate co-rotating frame. In this frame, we define

$$\mathbf{S} \equiv \sum_i \alpha_i \mathbf{s}_i, \tag{4.94}$$

$$\mathbf{Q} \equiv \sum_i \frac{\alpha_i \mathbf{s}_i}{\gamma_i} + \frac{\omega}{\mu}\mathbf{H}_{\rm v}. \tag{4.95}$$

It's straightforward to show that when μ is constant, $\mathbf{S}$, $\mathbf{r} \equiv \mathbf{Q}/Q$ and $\mathbf{r}_i \equiv 2\mathbf{s}_i$ with $\gamma_i \neq \pm 1$ form a close set of differential equations :

$$\frac{d\mathbf{S}}{dt} = \omega Q \mathbf{r} \times \hat{\mathbf{z}} + \omega \sum_i \frac{\alpha_i}{2}\left(\gamma_i - \frac{1}{\gamma_i}\right)\mathbf{r}_i \times \hat{\mathbf{z}}, \tag{4.96}$$

$$\frac{d\mathbf{r}}{dt} = -\mu \mathbf{r} \times \mathbf{S}, \tag{4.97}$$

$$\frac{d\mathbf{r}_i}{dt} = -\mu \mathbf{r}_i \times \left(\mathbf{S} - \frac{\omega\gamma_i}{\mu}\hat{\mathbf{z}}\right), \tag{4.98}$$

where $\hat{\mathbf{z}} \equiv \mathbf{H}_{\rm v}$. Note that here $\mathbf{r}$ and $\mathbf{r}_i$ have constant unit lengths and Q and S_z are constant under time evolution. Besides, from the conservation of the "effective energy" (see Sec. 4.2 or [24]) $E_{\rm eff} \equiv \frac{\mu}{2}\mathbf{S}^2 - \sum_i \omega\gamma_i\alpha_i \mathbf{s}_i \cdot \hat{\mathbf{z}}$, it is straightforward to show that

$$E'_{\rm eff} \equiv \frac{\mu}{2}\mathbf{S}^2 - \left[\omega Q \mathbf{r} + \omega \sum_i \frac{\alpha_i}{2}\left(\gamma_i - \frac{1}{\gamma_i}\right)\mathbf{r}_i\right] \cdot \hat{\mathbf{z}}, \tag{4.99}$$

is also a constant of motion.

Pure-Precession Solution in Synchronization Limit

Since S_z, $|\mathbf{r}|$ and $|\mathbf{r}_i|$ are constant, it is natural to parametrize $\mathbf{S}$, $\mathbf{r}$ and $\mathbf{r}_i$ in the typical spherical coordinate by

$$\mathbf{S} \equiv S_z\hat{\mathbf{z}} + S_\perp \cos\phi_s \hat{\mathbf{x}} + S_\perp \sin\phi_s \hat{\mathbf{y}}, \tag{4.100}$$

$$\mathbf{r} \equiv \cos\theta\hat{\mathbf{z}} + \sin\theta\cos\phi\hat{\mathbf{x}} + \sin\theta\sin\phi\hat{\mathbf{y}}, \tag{4.101}$$

$$\mathbf{r}_i \equiv \cos\theta_i\hat{\mathbf{z}} + \sin\theta_i\cos\phi_i\hat{\mathbf{x}} + \sin\theta_i\sin\phi_i\hat{\mathbf{y}}. \tag{4.102}$$

Equaion (4.96)-(4.98) then becomes

$$\dot{S}_\perp = \omega Q \sin\theta \sin(\phi - \phi_s) + \sum_i \omega q_i \sin\theta_i \sin(\phi_i - \phi_s), \tag{4.103}$$

$$S_\perp \dot{\phi}_s = -\omega Q \sin\theta \cos(\phi - \phi_s) - \sum_i \omega q_i \sin\theta_i \cos(\phi_i - \phi_s), \quad (4.104)$$

$$\dot{\theta} = -\mu S_\perp \sin(\phi - \phi_s), \quad (4.105)$$

$$\dot{\phi} \sin\theta = \mu S_z \sin\theta - \mu S_\perp \cos\theta \cos(\phi - \phi_s), \quad (4.106)$$

$$\dot{\theta}_i = -\mu S_\perp \sin(\phi_i - \phi_s), \quad (4.107)$$

$$\dot{\phi}_i \sin\theta_i = \mu \left(S_z - \frac{\omega\gamma_i}{\mu} \right) \sin\theta_i - \mu S_\perp \cos\theta_i \cos(\phi_i - \phi_s), \quad (4.108)$$

where $q_i \equiv \frac{\alpha_i}{2}\left(\gamma_i - \frac{1}{\gamma_i}\right)$.

To analyze any non-linear ODE system, the first step is always to find out its static solution which is essentially a fixed point in the phase space because the stability of the fixed point could tell us the qualitative behavior of the system. In this particular case, due to the rotational symmetry in $\hat{\mathbf{z}}$ direction, any pure-precession solution such that all vectors rotate around $\hat{\mathbf{z}}$ with the same frequency is equivalent to a static solution.

A pure-precession solution can be derived using the conditions $\dot{\phi}_s = \dot{\phi} = \dot{\phi}_i$, $\ddot{\phi} = 0$ and $\dot{\theta} = \dot{\theta}_i = 0$. This implies $\sin(\phi - \phi_s) = \sin(\phi_i - \phi_s) = 0$ and $\dot{S}_\perp = 0$ from equations (4.103), (4.105) and (4.107). The remaining equations become

$$S_\perp \dot{\phi} = -\omega Q \sin\theta C - \sum_i \omega q_i \sin\theta_i C_i, \quad (4.109)$$

$$\dot{\phi} \sin\theta = \mu S_z \sin\theta - \mu S_\perp \cos\theta C, \quad (4.110)$$

$$\dot{\phi} \sin\theta_i = \mu \left(S_z - \frac{\omega\gamma_i}{\mu} \right) \sin\theta_i - \mu S_\perp \cos\theta_i C_i, \quad (4.111)$$

where C and C_i are $\cos(\phi - \phi_s)$ and $\cos(\phi_i - \phi_s)$, which can only be either 1 or -1 depending on the initial directions of $\mathbf{s}_i$. Using equation (4.99) and equations (4.109)-(4.111), for any given initial conditions, one can always solve for $S_\perp$, θ, θ_i and $\dot{\phi}$ to find out the corresponding pure-precession solution. A particular important case is when $\mu \to \infty$ and $\theta_{\rm v} \to 0$, which is an approximate initial condition for our supernova neutrinos. In this case, by taking $S_\perp \to 0$, $\theta \to 0$, and $\theta_i \to 0$ because of the small effective mixing angle, one can show that there always exists a pure-precession solution

which is at the neighborhood of the initial condition as follows :

$$\theta \approx \frac{\mu S_\perp}{|\dot{\phi} - \mu S_z|}, \tag{4.112}$$

$$\theta_i \approx \frac{\mu S_\perp}{|\dot{\phi} + \omega\gamma_i - \mu S_z|}, \tag{4.113}$$

$$\dot{\phi} \approx -\frac{(\pm\omega Q) + (\sum_i \pm\omega q_i)}{S_z}, \tag{4.114}$$

$$S_\perp \approx 2S_z\theta_V, \tag{4.115}$$

where in equation (4.114), a plus(minus) sign indicates that $\mathbf{r}$ or $\mathbf{r}_i$ initially approximately align(anti-align) with $\hat{\mathbf{z}}$. Note that here the precession frequency $\dot{\phi}$ is "slow" in the order of ω instead of the order of μ. One can easily show that it is the same as the "synchronized frequency" $\omega_{\rm sync}$ defined in equation (3.33).

If this pure-precession solution is a stable fixed point, we should expect that the actual system would stay near it as the gyroscope in Sec. 4.2. However, it was shown in [35, 68] that large flavor oscillation may happen even at the extremely synchronized regime. This indicates that the stability of this pure-precession solution needs to be carefully examined.

Instability of the Pure-Precession Solution

The simplest method to determine the stability of non-linear ODEs is to linearize the equations around the fixed point by linear expansions. For a system $\dot{\mathbf{x}} = f(\mathbf{x})$ with a fixed point $\mathbf{x}_0$ such that $f(\mathbf{x}_0) = 0$, by defining $\mathbf{x} \equiv \mathbf{x}_0 + \boldsymbol{\xi}$, the equation becomes $\dot{\boldsymbol{\xi}} = A(\mathbf{x}_0)\boldsymbol{\xi} + O(\boldsymbol{\xi}^2)$, where $A(\mathbf{x}_0)$ is the linearized matrix of $f(\mathbf{x})$. If all eigenvalues of $A(\mathbf{x}_0)$ have non-positive real parts, then $\mathbf{x}_0$ is a local stable fixed point. If there exists any eigenvalue with positive real part, then the fixed point is unstable.

We derive the general structure of the linearized matrix and the form of its corresponding characteristic equation for a system with any numbers of NFIS's in Appendix B.1. We first look at the simplest case with only two NFIS's which is an equivalent gyroscope. Using equations (B.1) and (B.2), it is straightforward to show that the

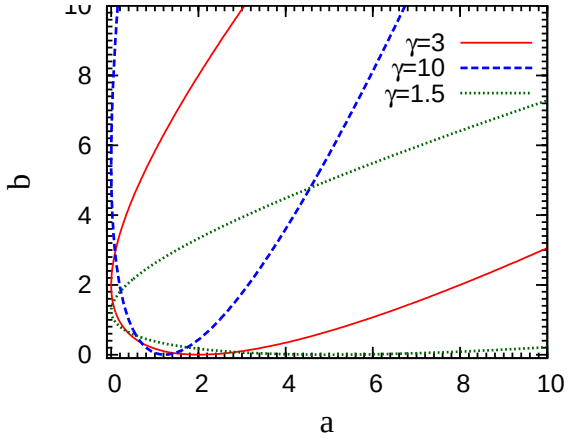

Figure 4.26: Boundary of the flavor instability of the pure-precession solution in the high density $\mu \to \infty$ limit. The region inside the parabola is where the system becomes unstable.

eigenvalues λ in this simple system satisfy the reduced characteristic equation

$$\lambda^2 + \frac{\mu^2 S_\perp^4 + 2c_\theta s_\theta^2 \mu Q S_\perp^2 + s_\theta^2 Q^2}{s_\theta^2 S_\perp^2} = \lambda^2 + \omega_n^2 = 0, \tag{4.116}$$

where ω_n is the nutation frequency defined in equation (4.41). The result $\lambda = \pm i\omega_n$ confirms that any perturbation around the pure-precession solution of a gyroscope system is always stable. Note that the form of the nutation frequency here is independent of the value C which is the relative angle between $\mathbf{S}$ and $\mathbf{Q}$ in the x-y plane.

However, for a system with three NFIS's which has $-\mathbf{s}_1(0) = \mathbf{s}_2(0) = \mathbf{s}_3(0) = \hat{\mathbf{e}}_z^{\mathrm{f}}/2$, $\alpha_1 = 1$, $\gamma_1 = 1$, $\alpha_2 = a$, $\gamma_2 = -1$, $\alpha_3 = b$ and $\gamma_3 = \gamma > 1$ without loss of generality. (a and b may be negative to represent different initial directions of those NFIS's.) After lengthy calculation as shown in Appendix B.2, we derive that the initial synchronized pure-precession of the three-spin system is unstable when

$$[a(\gamma - 1) - 2b]^2 - 2a(\gamma^2 - 1) - 4b(\gamma + 1) + (\gamma + 1)^2 < 0, \tag{4.117}$$

for $\mu \to \infty$ and $\theta_{\mathrm{v}} \to 0$. We plot the parabolic curves which correspond to the boundary of the inequality for three different values of γ in Fig. 4.26. The regions inside those

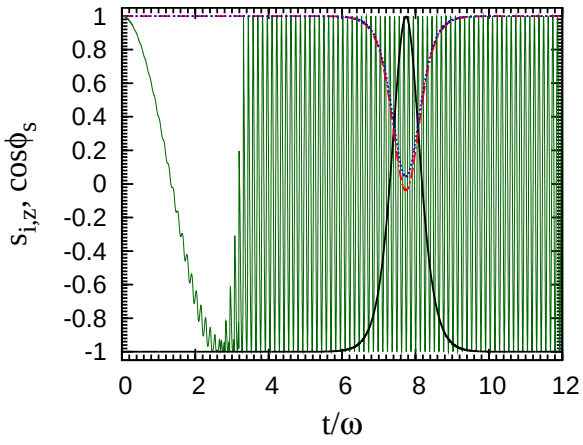

Figure 4.27: The evolution of $\mathbf{s}_{1,z}$ (black line), $\mathbf{s}_{2,z}$ (blue line), $\mathbf{s}_{3,z}$ (red line) and ϕ_s (green line) in a three-NFIS system with the parameters $a = b = 1$, $\gamma = 1$, $\theta_v = 10^{-5}$, and $\mu/\omega = 100$.

parabolas are where the system becomes unstable. One particular case which was discussed in [68] is when $\gamma = 3$ and $a = b$, it is easy to show that the above inequality becomes $a > 1/2$ which recovers the criterion given by the numerical suggestion there. Note that equation (4.117) cannot be satisfied if $a = 0$, $b = 0$ or $\gamma = \pm 1$ which essentially reduces the three-NFIS system to a two-NFIS system. This again confirms that the two-NFIS system is always stable but the instability may occur for a three-NFIS system.

In Fig. 4.27, we show the evolution of $s_{i,z}$ and ϕ_s in a three-NFIS system with the parameters $a = b = 1$, $\theta_{\rm v} = 10^{-5}$, $\mu/\omega = 100$. One can clearly see that the amplitude of the fast rotation with frequency in the order of $|\mu S_z|$ which is initially a small perturbation around the slow synchronized precession grows at the initial phase due to the instability. This amplitude of the fast rotation eventually dominates the amplitude of the synchronized precession and large flavor oscillations of $\mathbf{s}_i$ are then triggered after this fast rotation mode grows.

4.3.2 Two-NFIS Reduction of a Three-NFIS System and Resonance

From the discussion in the section 4.3.1 about the instability of the NFIS system, we know that the synchronized pure-precession solution which is close to the initial configuration in high density limit may be unstable when there are more than two NFIS's. If the instability occurs, the system will go through a transition region where the nutation amplitudes of the fast rotation grows very fast and finally dominates the initial slow pure-precession.

After that, the system behaves as in a stable state again which is in average similar to be in an effective low density such that an average large "nutation" would develop (see Fig. 4.27). This behavior can be understood by adopting an approximate reduction from the original three-NFIS system to a two-NFIS system as will be shown below.

Effective Two-NFIS Reduction in High Density Limit

In a three-NFIS system with $\alpha_1 = 1$, $\alpha_2 = a$, $\alpha_3 = b$, $\gamma_1 = 1$, $\gamma_2 = -1$, $\gamma_3 = \gamma$, equations (4.96)-(4.98) becomes

$$\frac{d\mathbf{S}}{dt} = \omega Q\mathbf{r} \times \hat{\mathbf{z}} + \omega p\mathbf{r}_3 \times \hat{\mathbf{z}}, \tag{4.118}$$

$$\frac{d\mathbf{r}}{dt} = -\mu\mathbf{r} \times \mathbf{S}, \tag{4.119}$$

$$\frac{d\mathbf{r}_3}{dt} = -\mu\mathbf{r}_3 \times \left(\mathbf{S} - \frac{\omega\gamma}{\mu}\hat{\mathbf{z}}\right), \tag{4.120}$$

where $p \equiv \frac{b}{2}\left(\gamma - \frac{1}{\gamma}\right)$.

Since we know that all three vectors are rotating fast after the initial phase (see Fig. 4.27), we can go to a frame which rotates around $\hat{\mathbf{z}}$ with the frequency μS_z to eliminate the common fast motion. Equations (4.118)-(4.120) then becomes :

$$\frac{d\mathbf{S}_\perp}{dt} = (\mu S_z\mathbf{S}_\perp + \omega Q\mathbf{r} + \omega p\mathbf{r}_3) \times \hat{\mathbf{z}}, \tag{4.121}$$

$$\frac{d\mathbf{r}}{dt} = -\mu\mathbf{r} \times \mathbf{S}_\perp, \tag{4.122}$$

$$\frac{d\mathbf{r}_3}{dt} = -\mu\mathbf{r}_3 \times \mathbf{S}_\perp + \omega\gamma\mathbf{r}_3 \times \hat{\mathbf{z}}. \tag{4.123}$$

In equation (4.121), we know the leading order of μ dependence of the r.h.s. must vanish because the fast motion of $\mathbf{S}_\perp$ has been removed. This implies

$$\mathbf{S}_\perp = -\frac{\omega}{\mu S_z}(Q\mathbf{r}_\perp + p\mathbf{r}_{3,\perp}) + O\left(\frac{\omega^2}{\mu^2}\right). \tag{4.124}$$

Thus, in the limit of large μ, the remaining two equations become

$$\frac{d\mathbf{r}}{dt} \approx \frac{\omega}{S_z}\mathbf{r}\times(Q\mathbf{r}_\perp + p\mathbf{r}_{3,\perp}), \tag{4.125}$$

$$\frac{d\mathbf{r}_3}{dt} \approx \frac{\omega}{S_z}\mathbf{r}_3\times(Q\mathbf{r}_\perp + p\mathbf{r}_{3,\perp}) + \omega\gamma\mathbf{r}_3\times\hat{\mathbf{z}}. \tag{4.126}$$

It is easy to show that the quantity $Qr_z + pr_{3,z}$ is approximately conserved up to the leading order $O(1)$. We can thus go to another rotating frame with the frequency $\frac{\omega}{S_z}(Qr_z + pr_{3,z}) - \frac{1}{2}\omega\gamma$ to reduce the above equations to be

$$\frac{d\mathbf{r}}{dt} \approx -\frac{\omega\gamma}{2}\mathbf{r}\times\hat{\mathbf{z}} - \frac{\omega p}{-S_z}\mathbf{r}\times\mathbf{r}_3, \tag{4.127}$$

$$\frac{d\mathbf{r}_3}{dt} \approx \frac{\omega\gamma}{2}\mathbf{r}_3\times\hat{\mathbf{z}} - \frac{\omega Q}{-S_z}\mathbf{r}_3\times\mathbf{r}. \tag{4.128}$$

These two equations have exactly the same form as a two-NFIS system by defining $\vec{\mathsf{s}}_1 \equiv \frac{\mathbf{r}_3}{2}$, $\vec{\mathsf{s}}_2 \equiv \frac{\mathbf{r}}{2}$, $\mu' \equiv \frac{2\omega p}{-S_z}$, $\alpha' \equiv \frac{Q}{p}$, and $\mu'_{\mathrm{v}} \equiv \frac{\omega\gamma}{2}$ such that:

$$\frac{d\vec{\mathsf{s}}_1}{dt} \approx \frac{\mu'_{\mathrm{v}}}{2}\vec{\mathsf{s}}_1\times\hat{\mathbf{z}} - \mu'\alpha'\vec{\mathsf{s}}_1\times\vec{\mathsf{s}}_2, \tag{4.129}$$

$$\frac{d\vec{\mathsf{s}}_2}{dt} \approx -\frac{\mu'_{\mathrm{v}}}{2}\vec{\mathsf{s}}_2\times\hat{\mathbf{z}} - \mu'\vec{\mathsf{s}}_2\times\vec{\mathsf{s}}_1. \tag{4.130}$$

One may worry about the sign of μ' and α' being possibly negative. However, p can be chosen to be positive without lose of generality. If $S_z > 0$, the transformation $\vec{\mathsf{s}}_{1,2} \to -\vec{\mathsf{s}}_{1,2}$ and $\mu' \to -\mu'$ can always recover the same form of equations. This transformation according to the sign of S_z also guarantees that the mass hierarchy makes no difference in high density limit. Thus, once the three-NFIS system is specified in high density limit and satisfies the instability condition, it will behave like an effective two-NFIS system in low density. For example, a three-NFIS system with $a = b = 1$, $\gamma = 3$ with $\mathbf{s}_1(0) = -\mathbf{s}_2(0) = \mathbf{s}_3(0) = \hat{\mathbf{z}}_f \approx \pm\hat{\mathbf{z}}$ in high density limit has $S_z \approx \pm 0.5$,

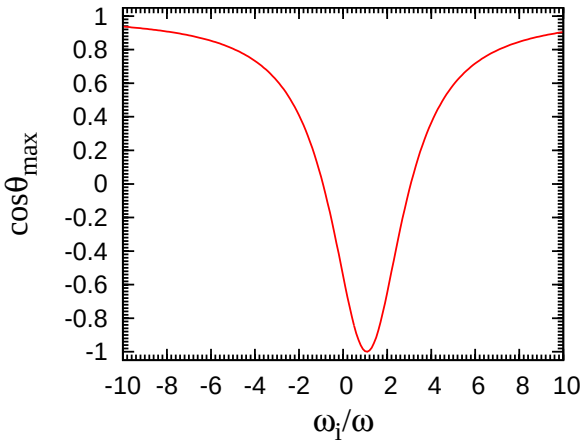

Figure 4.28: Resonance pattern of test NFIS's in the three-NFIS system shown by $\cos\theta_{\max}$ as a function of ω_i, where $\theta_{\max}$ is the maximum angle for the test NFIS could reach.

$Q \approx 5/6$, $p = 4/3$. The effective two-spin system will have the corresponding parameters $\frac{\mu'}{\mu'_v} \approx 32/9$ and $\alpha' \approx 5/8$ in the "inverted mass hierarchy" such that the large "nutation" can occur.

Behavior of the Effective Two-NFIS System

From Fig. 4.27, one can see that $\mathbf{s}_1$ goes through complete flavor transformation during the oscillations. Also, $S_\perp$ seems to rotate around $\hat{\mathbf{z}}$ with a constant frequency. This indicates that this particular system forms a self-resonant system such that $\mathbf{s}_1$ is right on resonance with $\mathbf{s}_2$ and $\mathbf{s}_3$ being almost equally off-resonance. We further find out that a resonance pattern exist if we put test NFIS's with vacuum frequency ω_i along with any three-block system as long as the instability criterion is satisfied. An example is shown in Fig. 4.28. This again suggests that at least in the period when the resonance occurs, $S_\perp$ is approximately rotating around $\hat{\mathbf{z}}$ in a quasi-uniform frequency ω_s. With this assumption, we can then find out the behavior of $S_\perp$ and explain the observed resonance pattern.

We define the gyroscopic vectors for the effective two-spin system as $\vec{\mathsf{S}} \equiv \vec{\mathsf{s}}_1 + \alpha'\vec{\mathsf{s}}_2$, $\vec{\mathsf{Q}} \equiv \vec{\mathsf{s}}_1 - \alpha'\vec{\mathsf{s}}_2 + \frac{\mu'_{\rm v}}{\mu'}\hat{\mathbf{z}}$, and $\vec{\mathsf{r}} \equiv \frac{\vec{\mathsf{Q}}}{\mathsf{Q}}$. Equations (4.129) and (4.130) then becomes

$$\dot{\vec{\mathsf{S}}} = \mu'_{\rm v}\mathsf{Q}\vec{\mathsf{r}} \times \hat{\mathbf{z}}, \tag{4.131}$$

$$\dot{\vec{\mathsf{r}}} = -\vec{\mathsf{r}} \times \mu'\vec{\mathsf{S}}. \tag{4.132}$$

Assuming $S_\perp$ rotates around $\hat{\mathbf{z}}$ with a constant frequency ω_s. We can parametrize S, r in the co-rotating frame of $\vec{\mathsf{S}}$ by writing

$$\vec{\mathsf{S}} \equiv \mathsf{S}_z\hat{\mathbf{z}} + \mathsf{S}_\perp\hat{\mathbf{x}}, \tag{4.133}$$

$$\vec{\mathsf{r}} \equiv \cos\theta\hat{\mathbf{z}} + \sin\theta\cos\phi\hat{\mathbf{x}} + \sin\theta\sin\phi\hat{\mathbf{y}}. \tag{4.134}$$

Equations (4.131) and (4.132) then become

$$\dot{\mathsf{S}}_\perp = \mu'_{\rm v}\mathsf{Q}\sin\theta\sin\phi, \tag{4.135}$$

$$\mathsf{S}_\perp\omega_s = -\mu'_{\rm v}\mathsf{Q}\sin\theta\cos\phi, \tag{4.136}$$

$$\dot{\theta} = -\mu'\mathsf{S}_\perp\sin\phi, \tag{4.137}$$

$$\dot{\phi} = \mu'\mathsf{S}_z - \omega_s - \mu'\mathsf{S}_\perp\frac{\cos\theta}{\sin\theta}\cos\phi, \tag{4.138}$$

From equations (4.136), (4.137) and (4.138), it is easy to show that

$$\dot{\mathsf{S}}_\perp\omega_s = \mu'_{\rm v}\mathsf{Q}\sin\theta\sin\phi(\mu'\mathsf{S}_z - \omega_s). \tag{4.139}$$

Comparing equation (4.139) to equation (4.135), we immediately see that $\vec{\mathsf{S}}$ rotates with the frequency

$$\omega_s = \frac{\mu'\mathsf{S}_z}{2}. \tag{4.140}$$

The equation of motion for $\mathsf{S}_\perp$ can be found by taking derivative of equation (4.135), substituting $\dot{\theta}$ and $\dot{\phi}$ by (4.137) and (4.138) again, and using equations (4.136) and (4.140):

$$\ddot{\mathsf{S}}_\perp = -\mu'_{\rm v}\mu'\mathsf{Q}\mathsf{S}_\perp\cos\theta - \left(\frac{\mu'\mathsf{S}_z}{2}\right)^2\mathsf{S}_\perp, \tag{4.141}$$

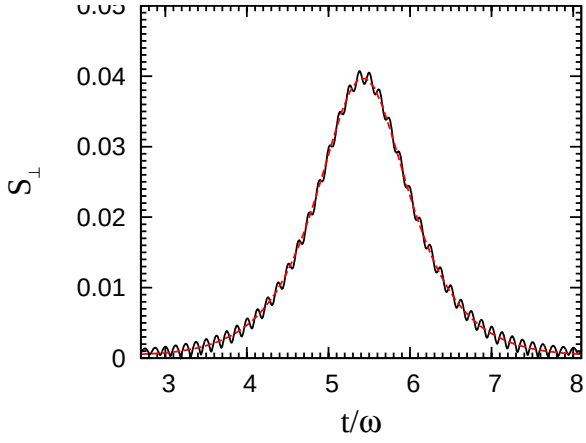

Figure 4.29: Time evolution of $\frac{2\omega p}{\mu S_z}\mathsf{S}_\perp$ (red line) and $\mathbf{S}_\perp$ (black line) of the three-NFIS system as functions of t/ω.

$$= \mu'\left(-\mu'_{\rm v}\vec{\mathsf{Q}}\cdot\hat{\mathbf{z}} - \frac{\mu'}{4}\mathsf{S}_z^2\right)\mathsf{S}_\perp, \tag{4.142}$$

$$= \mu'\left(\mathsf{E} - \frac{3\mu'}{4}\mathsf{S}_z^2 - \frac{\mu'}{2}\mathsf{S}_\perp^2\right)\mathsf{S}_\perp, \tag{4.143}$$

where $\mathsf{E} = -\mu'_{\rm v}\vec{\mathsf{Q}}\cdot\hat{\mathbf{z}} + \frac{\mu'}{2}\mathsf{S}^2$ is the conserved effective energy for the two-spin system.

The integration of equation (4.143) with the initial conditions $\mathsf{S}_\perp(0) \approx 0$ and $\dot{\mathsf{S}}_\perp(0) = 0$ gives

$$\dot{\mathsf{S}}_\perp^2 - \mu'\left(\mathsf{E} - \frac{3\mu'}{4}\mathsf{S}_z^2\right)\mathsf{S}_\perp^2 + \frac{\mu'^2}{4}\mathsf{S}_\perp^4 = 0. \tag{4.144}$$

The potential is a double-well type since $\mathsf{E}' \equiv \mathsf{E} - \frac{3\mu'}{4}\mathsf{S}_z^2 > 0$. Because $\mathsf{S}_\perp(0)$ is slightly positive, it will slowly roll toward larger value initially, then quickly reach the potential minimum where $\mathsf{S}_\perp = \sqrt{2E'/\mu'}$ is maximum. After the potential minimum, it will continue rolling over to the potential maximum with $\mathsf{S}_\perp = 2\sqrt{E'/\mu'}$ and and then oscillate back and forth. In Fig. 4.29, we show the time evolution of $\frac{2\omega p}{\mu S_z}\mathsf{S}_\perp$ from equation (4.144) and compare it with the solution $S_\perp$ solving from the original three-NFIS system. It is clear that the two-NFIS reduction and the quasi-precession assumption of $S_\perp$ indeed approximate the three-NFIS system very well. Note that the growth of $\mathsf{S}_\perp$ to large value

is a key feature to provide the system a wide resonance range as we will discuss next.

Resonance of Test Neutrinos

After knowing how the $\mathsf{S}_\perp$ of a three-NFIS system evolves with time, we can discuss how a test NFIS $\mathbf{s}_i = \mathbf{r}_i/2$ with energy E_i would respond to this three-spin system which could be used as the zeroth-order mean field of a continuous neutrino spectrum such as during the cooling phase. In the same frame as of equation (4.131), the equation for the NFIS is

$$\dot{\mathbf{r}}_i = \omega_i' \mathbf{r}_i \times \hat{\mathbf{z}} - \mu' \mathbf{r}_i \times \vec{\mathsf{S}}, \tag{4.145}$$

where $\omega_i' \equiv \omega_i - \frac{\omega\gamma}{2}$. Again, we parametrize the above equation in the co-rotating frame of $\vec{\mathsf{S}}$ as

$$\mathbf{r}_i \equiv \cos\theta_i \hat{\mathbf{z}} + \sin\theta_i \cos\phi_i \hat{\mathbf{x}} + \sin\theta_i \sin\phi_i \hat{\mathbf{y}}, \tag{4.146}$$

and derive

$$\dot{\theta}_i = -\mu' \mathsf{S}_\perp \sin\phi_i, \tag{4.147}$$

$$\dot{\phi}_i = \frac{\mu' \mathsf{S}_z}{2} + \omega_i' - \mu \mathsf{S}_\perp \frac{\cos\theta_i}{\sin\theta_i} \cos\phi_i, \tag{4.148}$$

where we have used equation (4.140).

For an NFIS which has the correct resonance frequency, it must be non-rotating in this co-rotating frame of $\vec{\mathsf{S}}$. From equation (4.148), one sees that $\dot{\phi}_i = 0$ can only be satisfied if $\cos\phi_i = 0$. This directly implies

$$\omega_{\rm res}' = -\frac{\mu' \mathsf{S}_z}{2}. \tag{4.149}$$

One can further show that $\frac{1}{2}\dot{\theta}_{\rm res}^2 = \mu' \mathsf{E}'(1 - \cos\theta_{\rm res})$, which is the energy form of an anharmonic oscillator released from the vertical position, leads to the same equation of motion in equation (4.147) for $\omega_i' = \omega_{\rm res}'$. For the example shown in Fig. 4.27, one can easily show that $\mathbf{s}_1$ is right on resonance. Thus, it undergoes complete flavor transformation with the trajectory exactly as the motion of an anharmonic oscillator.

Finally, one can verify that the general motion for any test NFIS can be described by

$$\mathbf{r}_i = \frac{1}{\tilde{\omega_i'}^2 + \mu'\mathsf{E}'} \begin{pmatrix} \pm\tilde{\omega_i'}\sqrt{2\mu'\mathsf{E}'(1-\cos\theta_{\rm res})} \\ \pm\mu'\mathsf{E}'\sin\theta_{\rm res} \\ \tilde{\omega_i'}^2 + \mu'\mathsf{E}'\cos\theta_{\rm res} \end{pmatrix}, \tag{4.150}$$

where $\tilde{\omega_i'} \equiv \omega_i' - \omega_{\rm res}'$ and the plus(minus) sign in the x and y components corresponds to the solution $\dot{\theta}_{\rm res} < 0$ ($\dot{\theta}_{\rm res} > 0$). In the form of equation (4.150), it clearly shows that the test NFIS with different ω_i form a resonance pattern for their z-component, centered at $\omega_{\rm res}'$ with the width $\Delta\omega' = 2\sqrt{\mu'\mathsf{E}'}$. We numerically confirm that this analytical result agrees with the resonance pattern (eg. see Fig. 4.28) very well.

4.3.3 Discussions and Summary

As we have seen in Fig. 2.2 in section 2.2, the ν_e and $\bar{\nu}_e$ spectra no longer dominate the ν_x spectra during the cooling phase. Thus, the flavor instability in the high density limit generally exists in the single-angle approximation due to the multiple spectra crossing as can be seen in Fig. 5.7 and Fig. 5.8. However, as pointed out in [26, 33], this early onset of flavor instability will be suppressed in the multi-angle approximation due to the dependence of the neutrino-neutrino term on the emission angle (see equation (4.90)).

Although the flavor instability in the multi-angle case can be formally derived as given by [26], how the flavor evolution history and the final survival/conversion probabilities would behave are beyond current analytical developments and cannot be approximated by the single-angle approximation. In addition, the time-evolution of both the neutrino emission and the supernova density profiles complicate the analytical treatment of collective oscillations. Thus, to accurately study the neutrino oscillations in supernovae and their effect on other physical processes, we have to rely on large-scale simulations as will be discussed in the next chapter.

Chapter 5

Neutrino Oscillations in an 18 Solar Mass Supernova Model

In chapter 4, we have learned that collective neutrino oscillations can be understood by simple analytical models in some cases, such as during the phase of the neutronization neutrino burst and the accretion phase with low matter density profile. However, we have also seen that the a typical neutrino spectra in the cooling phase cannot be treated easily by our analytical methods or even by the single-angle approximation. This is because the anisotropic nature of neutrino emission, the so-called "multi-angle" effects, which was only realized very recently, plays important but complicated role in the evolution of neutrino flavors during the cooling phase [26, 33, 62]. Besides, both the matter density profile and the emitted neutrino spectra are changing with time as the proto-neutron star cools. They will greatly affect the details of collective neutrino oscillations, such as where the flavor transformations start and the extent of spectra swapping as will be shown later. Therefore, to improve our understanding of the roles of neutrino flavor oscillations on nucleosynthesis in neutrino-driven winds [69,70] and the long-term neutrino signals [71], we need a more delicate model to combine the neutrino emission, the time-dependent matter density profile and the neutrino oscillations instead

of using some simple assumptions such as a particular emitted neutrino spectra, an universal matter density profile or the simplified scheme of collective oscillations. For example, in the case of the effect on nucleosynthesis in the neutrino-driven wind, a mass shell takes about 10 seconds from the ejection to where the heavy nuclei freeze out. In contrast, neutrinos which travel in the speed of light only need about a hundredth second to go through the same region. This means that each particular wind trajectory at different radii is exposed to the neutrino fluxes that are emitted at different time with different flavor evolution history!

Thus, to achieve a more self-consistent study of the effect of collective neutrino oscillations on nucleosynthesis in neutrino-driven winds and the neutrino signals, we adopt the time-dependent neutrino emission data and the matter density profiles from the 18 $M_\odot$ model in a supernova simulation with sophisticated neutrino transport [5]. We then simulate the neutrino flavor evolution through the relevant region for about 40 different time snapshots during the post-bounce time $1.0 \lesssim t_{\rm pb} \lesssim 10.0$ seconds to obtain the neutrino spectra modified by the oscillations as functions of radius and post-bounce time. The results of the oscillations are then used to study the effect on nucleosynthesis in the neutrino-driven wind and to calculate the neutrino signals in the IceCube detector.

The chapter is organized as follows. In section 5.1, we describe the models of supernova explosion and neutrino oscillations. We show our results of neutrino oscillations in section 5.2. There we discuss different behavior of collective neutrino oscillations due to the change of both neutrino spectra and the environment. We discuss the role of multi-angle effects in oscillations. We then discuss the effect of oscillations on neutrino capture rates on free nucleons in section 5.3. In section 5.4, we use the results of collective oscillations as the initial condition for the subsequent MSW flavor transformation and calculate the expected neutrino signal in the IceCube detector. At last, we give our discussions and summary in section 5.6.

5.1 The Supernova and Neutrino Oscillation Models

5.1.1 The Supernova Model

We explore neutrino-driven explosions of massive stars in spherical symmetry. In the following paragraphs, we will summarize main features of these explosions.

The supernova model, AGILE-BOLTZTRAN, is based on general-relativistic radiation hydrodynamics in spherical symmetry. It employes three-flavor Boltzmann neutrino transport. For details about the radiation hydrodynamics equations, including the numerical discretization, see [72] and references therein. For this study of collective neutrino flavor oscillations in supernovae, we analyze results published in [5]. There, the standard weak processes were considered which are listed in Table 1 of [5]. Furthermore, the baryon equation of state from [73] was used for matter which is in nuclear statistical equilibrium (NSE) with temperatures above 0.45 MeV. This equation of state is based on relativistic mean field approach and Thomas-Fermi approximation for heavy nuclei. It is considered a stiff equation of state which allows for maximum neutron star masses of 2.3 $M_\odot$. For matter with temperatures below 0.45 MeV, processes out of equilibrium are important where a nuclear reaction network for 20 nuclei was used for the energy generation. The baryon equation of state in that regime is calculated based on the ideal gas of heavy nuclei. On top of the baryons, contributions from electrons and positrons as well as photons and coulomb corrections are added following [74].

In the literature, several explosion mechanisms of massive stars have been explored: the magneto-rotational mechanism by [75], the dumping of acoustic energy by [76] and the standard scenario due to neutrino heating by [77]. Recently, it has been shown in [78] and [79] that a quark-hadron phase transition can lead to the formation of an additional shock wave that can trigger explosions. In this study, we explore standard neutrino-driven explosions, which can only be obtained in spherically-symmetric supernova simulations of the low-mass O-Ne-Mg-core. It is a combination of neutrino heating and energy deposition from nuclear burning processes on a short timescale on the order

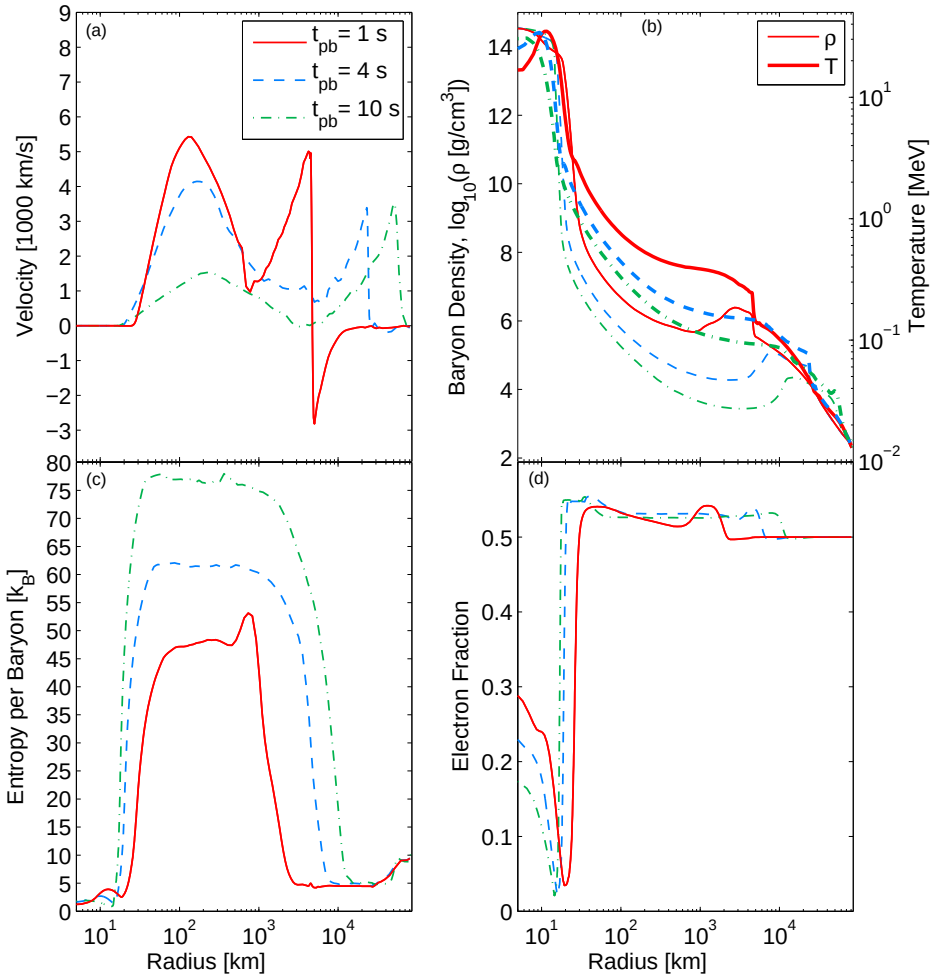

Figure 5.1: Radial profiles of selected hydrodynamic quantities of the 18 $M_\odot$ supernova explosion model under investigation, after the explosion has been launched.

of 30 ms post bounce, as was shown in [3] and [5]. The success of this model is due to the special structure of the progenitor with a very steep density gradient at the interface between C-O-layer and the hydrogen-rich envelop. More massive iron-core progenitors have an extended Si-S-layer surrounding the iron-core with much higher density. The post-bounce evolution leads to an extended accretion phase which can last for several 100 ms (depending on the progenitor).

In order to trigger the explosion for the 18 $M_\odot$ progenitor from [1] under investigation here, neutrino heating was enhanced in the gain region between the standing bounce shock and the neutrino spheres (see [5] for details). After the explosion has developed, a region of decreasing density and increasing entropy forms between the expanding explosion shock and the central proto-neutron star. It is illustrated in Fig. 5.1, showing radial profiles of selected quantities during the post-explosion evolution. This region is subject to continuous neutrino heating where a low-mass outflow develops, known as neutrino-driven wind (see the velocity profiles in Fig. 5.1 (a) between 50–1000 km). Relevant for possible nucleosynthesis is, next to the entropies per baryon which reach $\sim$ 100 k_B, the proton-to-baryon ratio which is given by the electron fraction Y_e. As shown in Fig. 5.1 (d) and discussed in [5], matter becomes generally proton-rich and stays proton-rich for more than 10 seconds. It is related to the increasing similarity of ν_e and $\bar{\nu}_e$ spectra, both of which become dominated by neutral-current processes. Due to final-state electron-blocking and the increasing nucleon-degeneracy, the importance of charged-current reactions reduces continuously after the onset of explosion. It may allow for nucleosynthesis under proton-rich conditions, in particular the νp process [80, 81]. For such a process, the final abundances of nuclei depend sensitively on Y_e of the wind and the $\bar{\nu}_e$ capture rate in the temperature range of $1\mathrm{GK} \lesssim T \lesssim 3\mathrm{GK}$. We will return to this important aspect of $Y_e > 0.5$ during the nucleosynthesis discussion further below.

Since the final production of nucleosynthesis in neutrino-driven winds depends on Y_e and $\bar{\nu}_e$ capture rate which may be altered by any change of neutrino or antineutrino spectrum close to the proto-neutron star, collective neutrino oscillations which typically

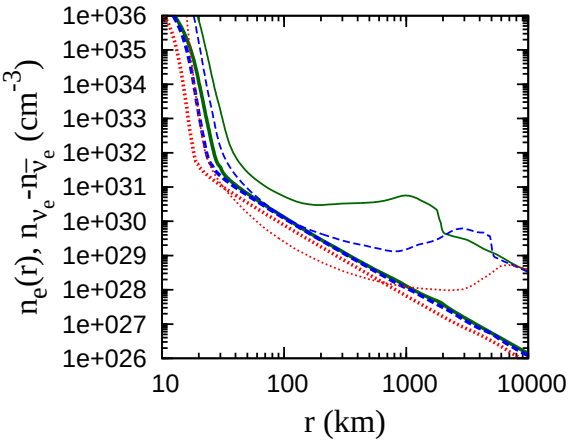

Figure 5.2: n_e (thin lines) and $n_{\nu_e} - n_{\bar{\nu}_e}$ (thick lines) as functions of radius for $t_{\rm pb} \approx 0.6$ (solid green), 1.0 (dashed blue), and 3.0 (dotted red) second.

occur within a few hundred kilometers above the proto-neutron star may have significant effects on the nucleosynthesis as recently studied in [69, 70]. However, as pointed out recently in [28, 62], if the electron number density is much larger than the difference of neutrino number densities of ν_e and $\bar{\nu}_e$, the collective oscillations will be strongly suppressed by the multi-angle effect due to the large dispersion of matter potential seen by neutrinos with different trajectories. In Fig. 5.2, we show both n_e and $n_{\nu_e} - n_{\bar{\nu}_e}$ for $t_{\rm pb} \approx 0.6$, 1.0, and 3.0 second. At $t_{\rm pb} \approx 0.6$ second, $n_e \gg n_{\nu_e} - n_{\bar{\nu}_e}$ at any given radius. However, At $t_{\rm pb} \approx 1.0$ second, the decrease of n_e is so fast that $n_e \approx n_{\nu_e} - n_{\bar{\nu}_e}$ around $r = 100$ km. At even later time, $n_e < n_{\nu_e} - n_{\bar{\nu}_e}$ for a few hundred kilometers above the neutrino sphere. Thus, we expect that collective neutrino oscillations would happen when $t_{\rm pb} \gtrsim 1.0$ second and have some impacts on the neucleosynthesis for mass elements ejected around and after that time.

For the analysis of possible collective neutrino-favor oscillations and the impact to nucleosynthesis, we map the simulation data defined on the adaptive mass-grid onto a refined Lagrangian mass-grid. In the following, we will refer to these as mass zones. We select several individual mass zones according to an expected maximum effect with

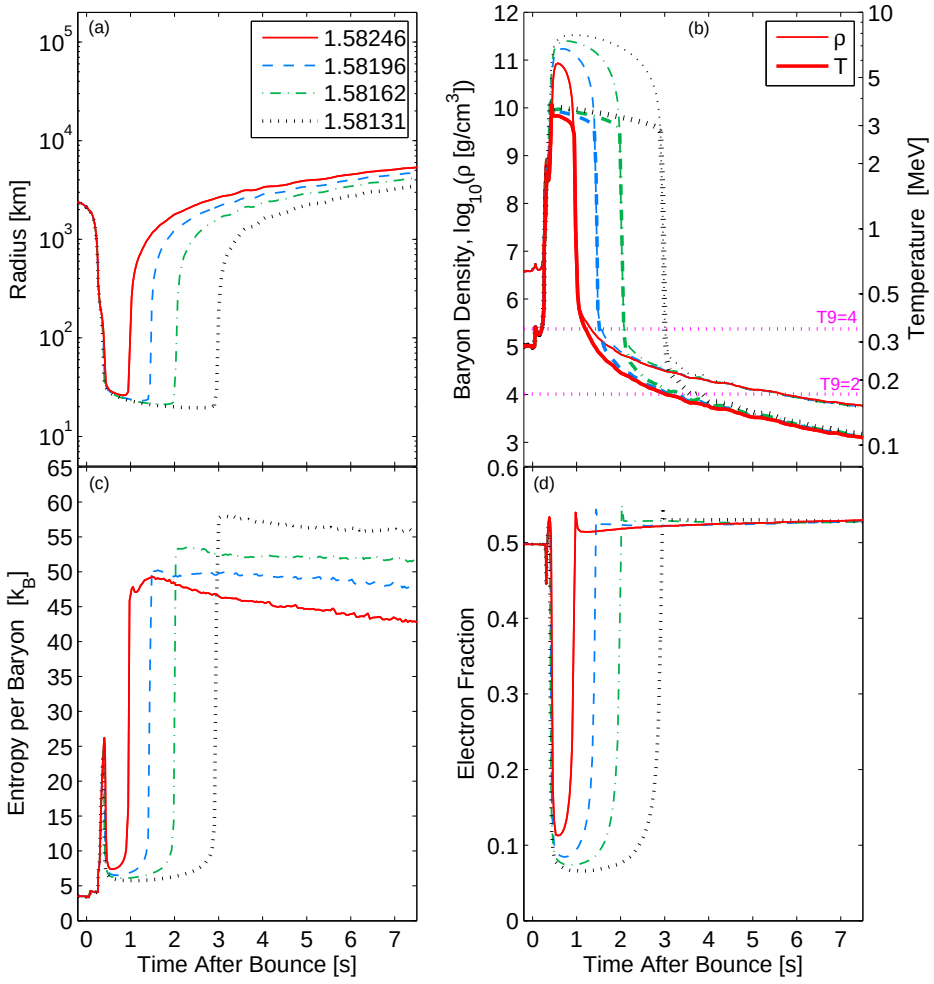

Figure 5.3: Post-bounce evolution of selected mass zones of the 18 $M_\odot$ supernova explosion model under investigation, during the early neutrino-driven wind phase after the explosion has been launched.

Table 5.1: Selection of mass zones.

label	$M_{\rm B}$[1] [$M_\odot$]	$t_{\rm ejection}$[2] [s]
1	1.58246	0.840
2	1.58196	1.253
3	1.58162	1.726
4	1.58131	2.526

respect to neutrino oscillations. These are given in table 5.1 and labelled according to the enclosed baryon mass and corresponding post-bounce times of ejection. Fig. 5.3 shows the corresponding evolution of selected hydrodynamic quantities for these mass zones. At the beginning of the core-collapse simulation, all selected mass zones belong to the Si-S-layer of the progenitor with $Y_e \simeq 0.5$, with temperatures ~ 0.3 MeV (see Fig. 5.3 (b)). At the end of collapse, the mass zones contract towards the center. The temperature rises and the composition becomes dominated by iron-group elements where electron captures reduce the proton-to-baryon ratio. At high temperatures of about 3 MeV at the proto-neutron star surface (see Fig. 5.3), heavy nuclei dissociate into free nucleons where electron captures reduce the proton-to-baryon ratio to $Y_e \simeq 0.1$. The later neutrino heating on timescales on the order of seconds, ejects these selected mass zones at 0.840 (solid red), 1.253 (dashed blue), 1.726 (dash-dotted green) and 2.526 seconds (black dotted), shown in Fig. 5.3 (a). During the rapid neutrino-driven wind expansion on a timescale on the order of 100 ms, density and temperature drop below 10^5 g/cm^3 and 0.35 MeV respectively, as well as the entropy per baryon rises from 5 $k_{\rm B}$ (at the proto-neutron star surface) up to 50–80 $k_{\rm B}$ (depending on the time of ejection).

Related to the evolution of mean neutrino energies and luminosities, illustrated in Fig. 5.4, is the proton-to-baryon ratio established during the neutrino-driven wind expansion. Before the explosion has been launched, which is the case at about 350 ms post bounce (indicated by the vertical arrow in the upper panel of Fig. 5.4), mass accretion dominates the neutrino luminosities. After the onset of explosion, mass accretion

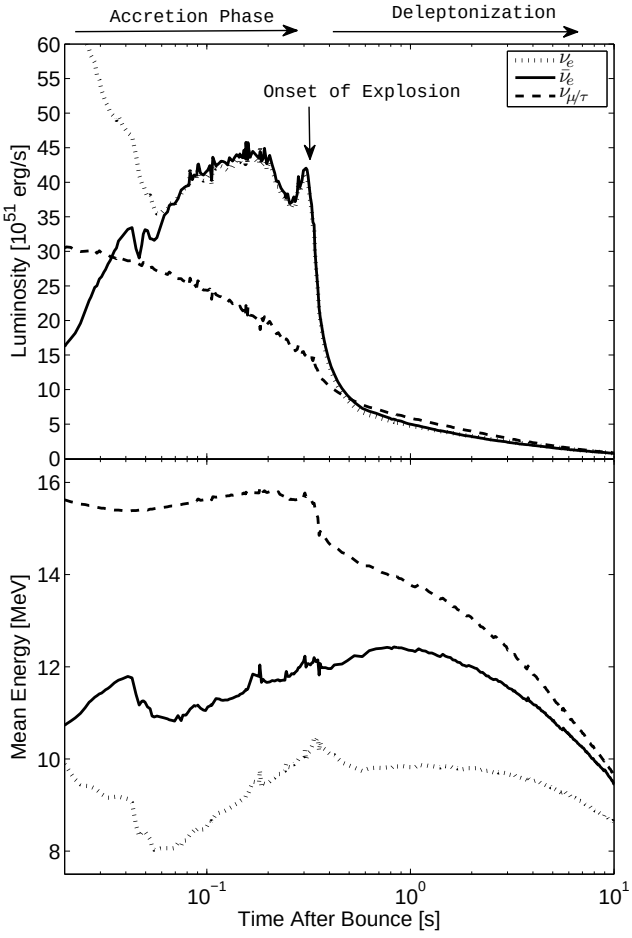

Figure 5.4: Evolution of neutrino luminosities and mean energies for the 18 $M_\odot$ supernova explosion model under investigation, sampled by an observer at infinity. Data are taken from [5].

vanishes and the luminosities are determined by diffusion during the proto-neutron star deleptonization. For similar ν_e and $\bar{\nu}_e$ luminosities, the small and reducing difference between $\langle E \rangle_{\nu_e}$ and $\langle E \rangle_{\bar{\nu}_e}$ favors generally proton-rich conditions, in particular since $\langle E \rangle_{\nu_e} - \langle E \rangle_{\bar{\nu}_e} < 4 \triangle$ (see [82] for a detailed discussion), where $\triangle = 1.2935$ MeV is the neutron-proton rest mass difference. This is the case for all times after the onset of explosion for the models discussed in [5].

5.1.2 Neutrino Oscillation Model

We model the neutrino flavor oscillations above the proto-neutron star similar to the "bulb model" in [53], in which all neutrinos are assumed to be free-streaming outward above a sharp neutrino sphere. However, the typical neutrino sphere R_ν which corresponds to the optical depth $\tau = 2/3$ does not represent such a sphere because significant amounts of neutrinos are still going inward as shown in Fig. 5.5. We thus define a "decoupling sphere" R_d where the neutrinos propagating inward are negligible (generally $\lesssim 2\%$) compared to outward ones. Note that in contrast to the isotropic emission assumed in the "bulb model", the angular distribution of neutrinos is typically forward peaked as shown in Fig. 5.5. We also show the red-shift corrected energy luminosity for different flavors as functions of radius in Fig. 5.5. It is clear that the luminosity is indeed near constant above R_d, indicating that neutrinos are nearly free-streaming.

In the assumed neutrino free-streaming region $r > R_d$, the coherent forwarding scattering of neutrinos on electrons and neutrinos along with the vacuum mixing cause neutrino flavor transformation. We write the flavor wavefunction of a neutrino as $\psi_\nu = (a_e, a_x, a_y)^T$ in the modified flavor basis where $(|\nu_e\rangle, |\nu_x\rangle, |\nu_y\rangle)^T = R_{23}^{-1}(\theta_{23})(|\nu_e\rangle, |\nu_\mu\rangle, |\nu_\tau\rangle)^T$ with R_{23} being the rotation matrix in the 2-3 subspace such that the neutrino mass hierarchies can be easily separated [83]. The evolution of neutrino flavor wavefunction as a function of the neutrino energy E, the cosine of propagation angle with respect to the radial direction $u = \cos\theta$, and the radius r, is then governed by the Schrodinger-like

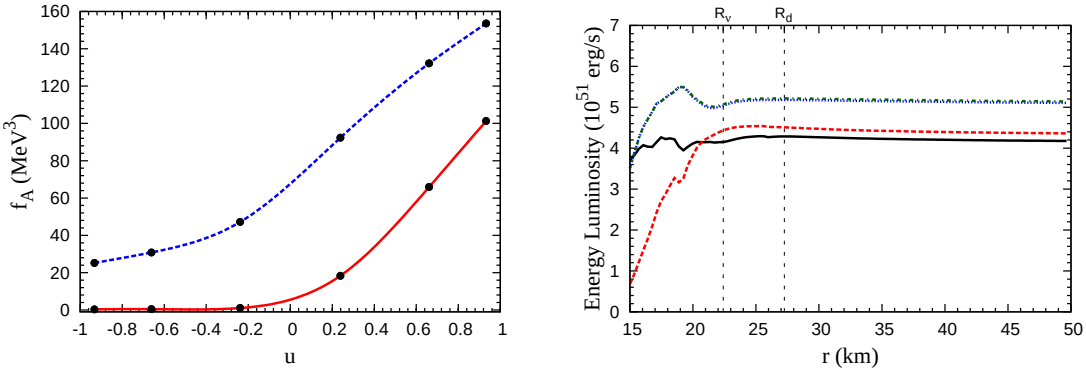

Figure 5.5: Left panel : Neutrino angular distributions for electron neutrinos $f_{A,\nu_e}(u,r) \equiv \int E^2 dE f_{\nu_e}(E,u,r)$ at $r = R_\nu$ (blue dashed) and $r = R_d$ (red solid) for $t_{\rm pb} = 1.025$ second. Right panel : Red-shift corrected luminosity of ν_e (black solid), $\bar{\nu}_e$ (red dashed), $\nu_{\mu,\tau}$ (blue dotted), and $\bar{\nu}_{\mu,\tau}$ (green dash-dotted) for the same $t_{\rm pb}$.

equation,

$$i\frac{d}{dt}\psi_\nu(E,u,r) = H_{\rm tot}\psi_\nu(E,u,r) = (H_{\rm v} + H_{\rm e} + H_\nu)\psi_\nu(E,u,r), \tag{5.1}$$

where $H_{\rm v}$, $H_{\rm e}$, and H_ν denote the potential from vacuum, electrons, and neutrinos, respectively. These potentials can be explicitly written down as,

$$\begin{aligned} H_{\rm v}(E) &= U\frac{M^2}{2E}U^\dagger, & (5.2)\\ H_{\rm e}(r) &= \sqrt{2}G_F n_e(r) diag(1,0,0), & (5.3)\\ H_\nu(u,r) &= \frac{\sqrt{2}G_F}{(hc)^3}\sum_\alpha \int E'^2 dE' du' d\phi' (1-uu')[f_{\nu_\alpha}(E',u',r)\rho_{\nu_\alpha}(E',u',r) \\ &\quad - f_{\bar{\nu}_\alpha}(E',u',r)\rho^*_{\bar{\nu}_\alpha}(E',u',r)], & (5.4) \end{aligned}$$

where $M = diag(m_1, m_2, m_3)$, $U = R_{13}(\theta_{13})R_{12}(\theta_{12})$, $n_e(r)$ is the electron number density, $\rho_\nu = |\nu\rangle\langle\nu|$, $f_{\nu_\alpha}(E,u,r)$ is the neutrino number distribution function per phase volume in both momentum and spatial space in the units of $(hc)^3$ and $\alpha = e, x, y$ denotes the initial flavor of neutrinos or antineutrinos. For the neutrino mixing parameters, we use the values in [84] with $\Delta m^2_{21} = m_2^2 - m_1^2 = 7.59 \times 10^{-5}$ eV^2, $|\Delta m^2_{31}| = |m_3^2 - m_1^2| = 2.43 \times 10^{-3}$ eV^2, $\sin^2 2\theta_{12} = 0.87$. We adopt $\theta_{13} = 0.1$ which is smaller than the value

from the most recent measurement [10], although the results of using the two values of θ_{13} agree with each other within 5% difference (see appendix C.1). Note that $\Delta m_{31} > 0$ represents the normal mass hierarchy (NH) and $\Delta m_{31} < 0$ represents the inverted mass hierarchy (IH).

Numerically, for neutrinos which decouple at R_d at a given post-bounce time $t_{\rm pb}$, we first map the the neutrino distribution function $f_{\nu_\alpha}(E, u, R_d)$ from [5] onto a uniform 2-D grid as a function of $E(R_d)$ and $v \equiv u(R_d)^2$. We then ray-trace the flavor evolution history of those neutrinos. Using $dt = udr = D(v,r)dr$, equation (5.1) becomes

$$i\frac{d}{dr}\psi_\nu(E,v,r) = \left[\frac{H_{\rm v}(E) + H_{\rm e}(r)}{D(v,r)} + H'_\nu(v,r)\right]\psi_\nu(E,v,r), \tag{5.5}$$

where

$$\begin{aligned} H'_\nu(v,r) &= \frac{\sqrt{2}\pi G_F}{(hc)^3}\frac{R_d^2}{r^2}\sum_\alpha \int E'^2 dE' dv' \left[\frac{1}{D(v,r)D(v',r)} - 1\right] &(5.6)\\ &\times \ [f_{\nu_\alpha}(E',v')\rho_{\nu_\alpha}(E',v',r) - f_{\bar\nu_\alpha}(E',v')\rho^*_{\bar\nu_\alpha}(E',v',r)], &(5.7)\end{aligned}$$

and $D(v,r) = \sqrt{1 - \frac{R_d^2}{r^2}(1-v)}$. The equation for $\bar\nu$ can be written down easily by taking $H_{\rm e} \to -H_{\rm e}$ and $H'_\nu \to -(H'_\nu)^*$.

For the matter potential $H_{\rm e}(r)$, since the velocity of the mass flow is generally much smaller than the velocity of neutrinos, we assume the density profile doesn't change during the time for neutrinos emitted at $R_d(t_{\rm pb})$ to travel through the interested region for collective neutrino oscillations to occur (typically less than 1000 kilometers).

In principle, we can then numerically integrate equation (5.5) as an initial value problem starting from $r = R_d$ for any given $t_{\rm pb}$. However, because of the very large potential close to R_d, it takes extremely fine grids to reach convergence and avoid numerical artifacts. Fortunately, due to the multi-angle suppression [33, 62] which will be discussed later, there is essentially no flavor conversion at least within $r \lesssim 100$ km for our simulated post-bounce time domain $1.0s \lesssim t_{\rm pb} \lesssim 10.0s$. Thus, we start most of our simulations from $r_0 \approx 2 \sim 3R_d$ and assume that all neutrinos are in pure flavor eigenstates at r_0 to reduce the computational efforts. In addition to the simulation

in the multi-angle approximation described above, we also perform the corresponding single-angle calculations for some time snapshots for the sake of comparison.

5.2 Numerical Results

In this section, we present the results of our simulation of neutrino oscillations in the collective region during the cooling phase for $1.0 \lesssim t_{\rm pb} \lesssim 10.0$ seconds. We focus on the inverted mass hierarchy because the collective oscillations in the normal mass hierarchy are all extremely suppressed in our simulation. We also note that due to the very large matter density in the collective region, flavor conversion only occurs in the 1-3 (e-y) sector.

To facilitate the discussion, we again define $\omega = |\Delta m^2_{31}|/2E$ for neutrinos and $\omega = -|\Delta m^2_{31}|/2E$ for antineutrinos as in previous chapters. We also define the effective normalized spectrum

$$g(\omega) = -\frac{1}{n^{\rm eff}_\nu(R_d)}\frac{\Delta m^2_{31}}{2\omega^2}\begin{cases} \bar{f}_{\nu_e}(E) - \bar{f}_{\nu_x}(E), & \text{for } \omega > 0, \\ \bar{f}_{\bar{\nu}_x}(E) - \bar{f}_{\bar{\nu}_e}(E), & \text{for } \omega < 0, \end{cases} \tag{5.8}$$

where $n^{\rm eff}_\nu = 2(\Phi_{\nu_e} - \Phi_{\bar{\nu}_e} - \Phi_{\nu_x} + \Phi_{\bar{\nu}_x})$, $\Phi_\nu = \int E^2 dE u du d\phi f_\nu(E, u, \phi)$ and $\bar{f}_\nu(E) = \int dv d\phi E^2 f_\nu(E, v)$. The effective matter potential and neutrino self-coupling potential here are defined to be

$$\lambda(r) = \sqrt{2} G_F n_e(r) \frac{R_d^2}{2r^2}, \tag{5.9}$$

$$\mu(r) = \sqrt{2} G_F n^{\rm eff}_\nu(R_d) \frac{R_d^4}{4r^4}, \tag{5.10}$$

which measure the multi-angle effects on collective oscillations [26]. Note that the above definition of $g(\omega)$, $\lambda(r)$ and $\mu(r)$ are different from previous chapters for convenience.

5.2.1 Flavor Conversion Probabilities and "Spectral Splits/Swaps"

We first show the angle-averaged survival probabilities of electron neutrinos and antineutrinos, namely $\langle P_{\nu_e\nu_e}\rangle_v$ and $\langle P_{\bar{\nu}_e\bar{\nu}_e}\rangle_v$, as functions of E and $t_{\rm pb}$ at $r = 500$ km in

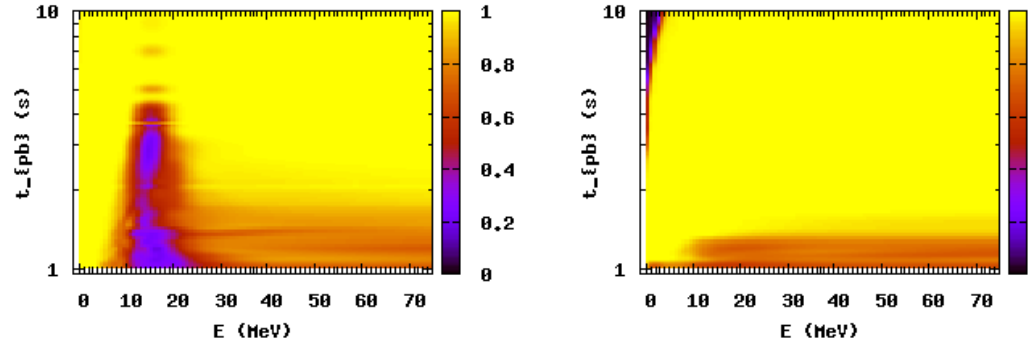

Figure 5.6: The angle-averaged neutrino survival probabilities $P_{\nu_e\nu_e}$ (left panel) and $P_{\bar{\nu}_e\bar{\nu}_e}$ (right panel) as functions of E and $t_{\rm pb}$ at $r = 500$ km.

Fig. 5.6, where the collective oscillations have already ceased. From Fig. 5.6, we could categorize the results of collective oscillations into four different regime in terms of the post-bounce time. For $t_{\rm pb} \lesssim 1.1$ second, large flavor conversion occurs for neutrinos with $E \gtrsim 5$MeV and all antineutrinos. For $1.1 \lesssim t_{\rm pb} \lesssim 2.0$ second, neutrinos with $E \gtrsim 8$ MeV and antineutrinos with $E \gtrsim 10$ MeV are affected by collective oscillations. For $2.0 \lesssim t_{\rm pb} \lesssim 5.0$ second, only neutrinos with $10 \lesssim E \lesssim 20$ MeV undergo collective oscillations. After $t_{\rm pb} \gtrsim 5.0$ second, collective oscillations are highly suppressed for all neutrinos and antineutrinos. Note that the flavor conversion for low energy electron antineutrinos at late time is purely due to the MSW potential.

We then show the same probabilities as functions of ω at $r = 500$ km for $t_{\rm pb} = 1.025$, 1.401, 3.007 and 5.0 seconds in Fig. 5.7. We also show the spectrum $g(\omega)$ (re-scaled) and the corresponding single-angle results in the same plot. Note that in the single-angle case, the probability is the sum of both final e and x flavors in order to be compared with the multi-angle results.

In Fig. 5.7, it clearly shows that although there are very distinct "spectral splits/swaps" in the single-angle simulations, these features are always smeared out or almost disappear in the multi-angle cases. Under single-angle approximation, spectral splits/swaps

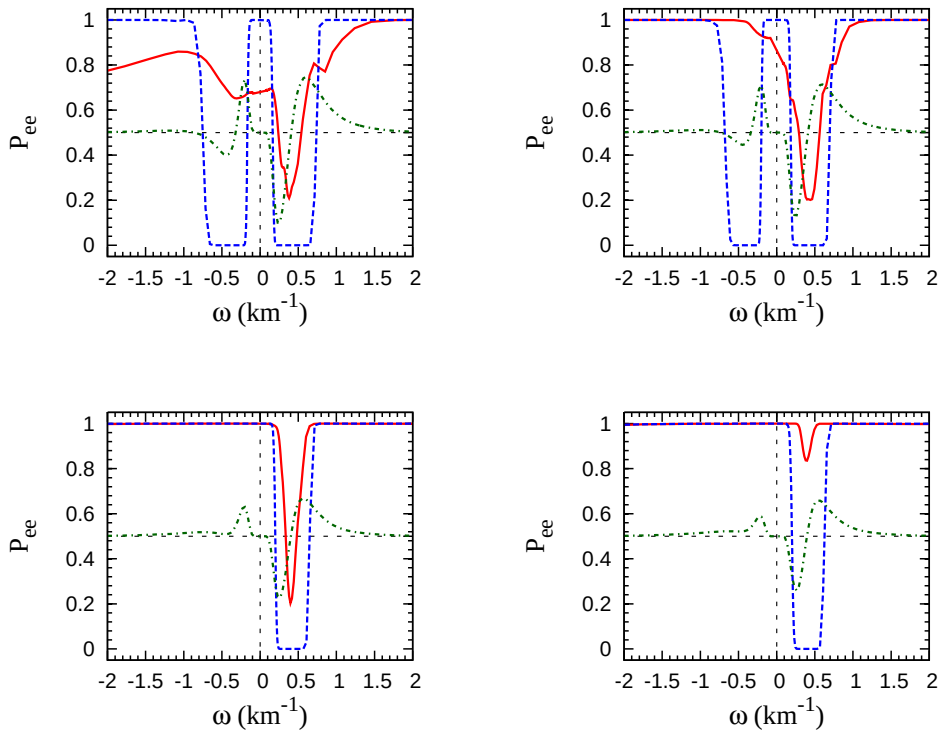

Figure 5.7: $\langle P_{\nu_e\nu_e}\rangle_v$ ($\omega > 0$) and $\langle P_{\bar{\nu}_e\bar{\nu}_e}\rangle_v$ ($\omega < 0$) at $r = 500$ km for multi-angle simulations (red solid) for $t_{\rm pb} = 1.025$ (top-left), 1.401 (top-right), 3.007 (bottom left) and 5.0 (bottom right) seconds. The corresponding single-angle results are shown in blue dashed line and $g(\omega)/15 + 0.5$ are shown in green dotted line.

could form around the "positive" spectral crossings [55] which correspond to where $g(\omega) = 0$ and $dg(\omega)/d\omega > 0$. However, because different angular trajectories see different potentials such that different parts of the spectrum are in resonance as discussed in section 4.2 (or see [46]), these splits in the energy spectrum are generally smoothed out in multi-angle cases by averaging over the angle.

We also note that the flavor conversion in the antineutrino sector only exists when there is an excess of $\bar{\nu}_e$ over $\bar{\nu}_x$ for $E \lesssim 18$ MeV at earlier time as shown in the top two panels of Fig. 5.7. At later time, when $\bar{\nu}_x$ complete dominate $\bar{\nu}_e$, only neutrino sector is affected by the collective oscillations as shown in the lower two panels of Fig. 5.7.

5.2.2 Flavor Conversion History and the Multi-angle Suppression

We show the angle-energy-averaged neutrino flavor conversion probabilities $\langle P_{\nu_e\nu_x}\rangle_{v,E}$, $\left\langle P_{\nu_e\nu_y}\right\rangle_{v,E}$, $\langle P_{\bar{\nu}_e\bar{\nu}_x}\rangle_{v,E}$ and $\left\langle P_{\bar{\nu}_e\bar{\nu}_y}\right\rangle_{v,E}$ as functions of radius for $t_{\rm pb} = 1.025$, 1.401, 3.007 and 5.0 seconds in Fig. 5.8. The growth of $\left\langle P_{\nu_e\nu_y}\right\rangle$ and $\left\langle P_{\bar{\nu}_e\bar{\nu}_y}\right\rangle$ generally indicates the 1-3 flavor conversion induced by Δm^2_{31} and the growth of $\langle P_{\nu_e\nu_x}\rangle$ and $\langle P_{\bar{\nu}_e\bar{\nu}_x}\rangle$ is associated with Δm^2_{21}. We also show the corresponding single-angle results in the same figure.

First, it is clear that the flavor instability which marks the rapid growth of the conversion probability in general exists right above the proto-neutron star in single-angle approximation for the whole cooling phase. This is because the multiple spectral crossings which are due to the similar luminosities and average energies of all flavors as shown in Fig. 5.4 (see section 4.3 for a simple discussion or [26] for detailed discussion). This instability causes the onset of large e-y flavor oscillations immediately above R_d and also trigger the early substantial onset of e-x flavor conversions as pointed out in [32, 35]. However, this instability is greatly suppressed by the multi-angle effects from both matter and neutrino-neutrino potential (see [26, 33, 62]). Thus, in the multi-angle simulations, large e-y flavor oscillations would not happen immediately above the neutrino sphere but at a few hundred kilometers and the e-x flavor oscillations are generally negligible.

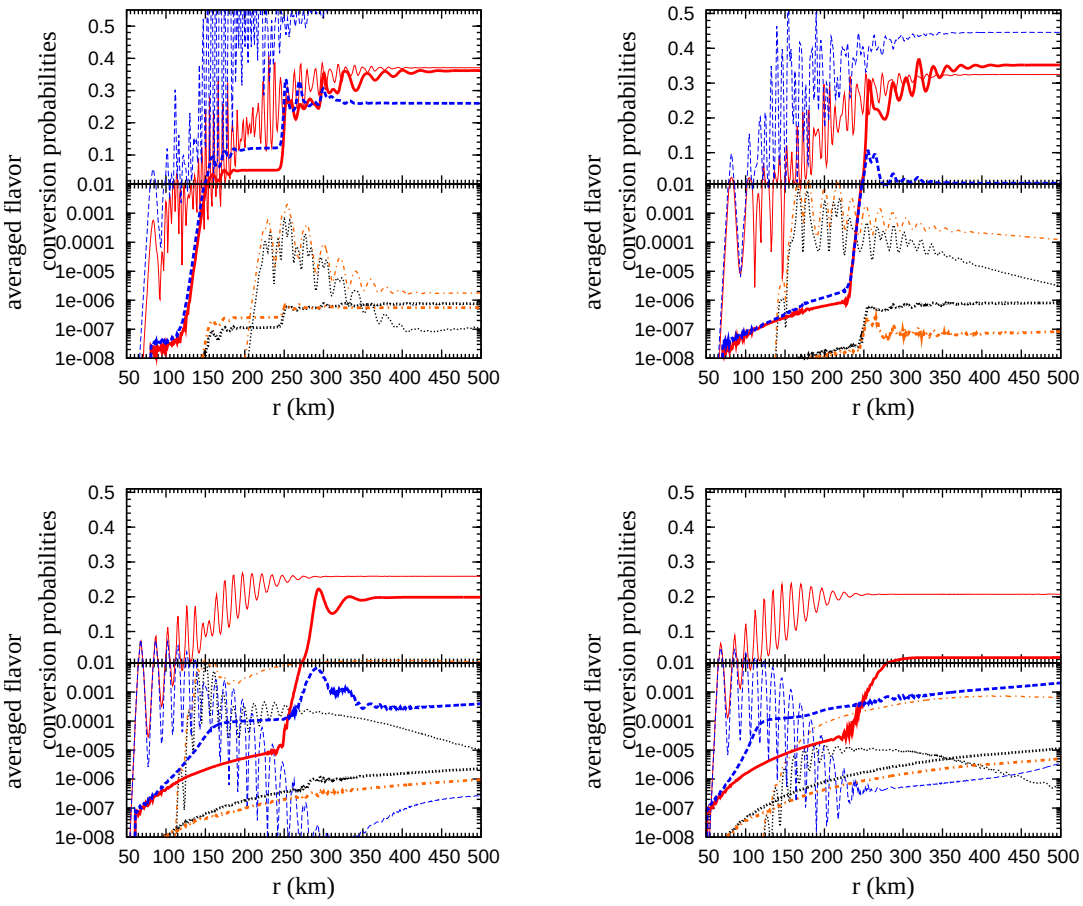

Figure 5.8: $\langle P_{\nu_e\nu_x}\rangle$ (black dotted), $\langle P_{\nu_e\nu_y}\rangle$ (red solid), $\langle P_{\bar{\nu}_e\bar{\nu}_x}\rangle$ (orange dash-dotted) and $\langle P_{\bar{\nu}_e\bar{\nu}_y}\rangle$ (blue dashed) for both single-angle (thin) and multi-angle (thick) simulations for $t_{\rm pb} = 1.025$ (upper left panel), 1.401 (upper right panel), 3.007 (bottom right panel), and 5.0 (bottom right panel) seconds.

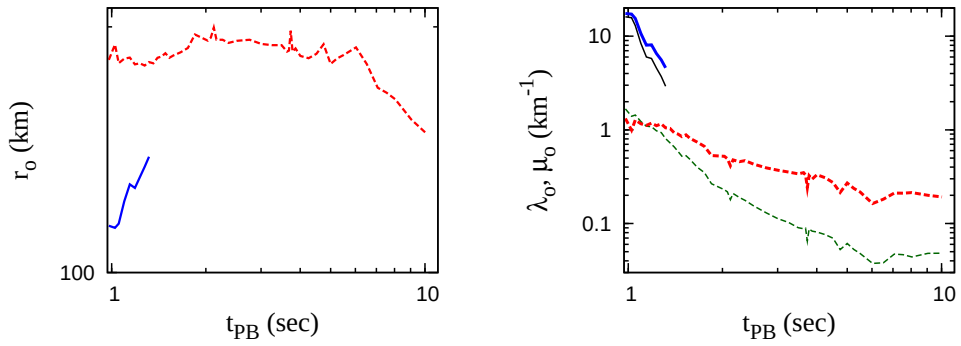

Figure 5.9: Left panel : r_o as a function of $t_{\rm pb}$. Right panel : λ_o (thin) and μ_o (thick) as functions of $t_{\rm pb}$. Solid lines and dashed lines represent two different instabilities.

The top-left panel of 5.8 represents the flavor evolution history for $t_{\rm pb} \lesssim 1.1$ second, where significant flavor conversion happens in both neutrino and antineutrino sectors. In this case, the flavor instabilities happen twice at $r \approx 120$ and 240 km. Note that the first instability affects more on the antineutrions and the second instability affects more on the neutrinos. For $t_{\rm pb} \gtrsim 1.1$ second, there is only one flavor instability at $200 \lesssim r \lesssim 250$ km. Also, the conversion probability grows slower to smaller value at later time such that fewer parts of the neutrino spectrum are affected as shown in Fig. 5.6.

We also plot the onset radius r_o for the flavor instability to occur and the corresponding $\lambda_o = \lambda(r_o)$ and $\mu_o = \mu(r_o)$ as functions of $t_{\rm pb}$ in Fig. 5.9. We see that at $t_{\rm pb} \approx 1.0$ second when the excess of $\bar{\nu}_e$ over $\bar{\nu}_x$ is still substantial (see Fig. 5.6), the instability at smaller radius happens around $\mu \approx \lambda \approx 10$ km^{-1}, which are much larger than the typical spread of the vacuum potential $|\Delta m^2_{31}|/2E \approx 0.6$ km^{-1} for $E \approx 10$ MeV. For the instability at larger radius, it exists for the whole cooling phase and generally happens at $\mu \approx |\Delta m^2_{31}|/2E$. However, at later time, this flavor instability occurs at even smaller μ because of the partial matter suppression that will be discussed in section 5.5.

5.3 Effect on Neutrino Capture Rates on Free Nucleons

In this section, we discuss the effect of neutrino oscillations on ν_e and $\bar{\nu}_e$ capture rates on free nucleons for different wind trajectories listed in table 5.1. We calculate the rates as functions of $t = t_{\rm pb} - t_0$ for those mass elements which are ejected at different t_0 as

$$\lambda_0(t) = \frac{2\pi c}{(hc)^3} \int \sigma_\nu(E) \frac{R_d^2}{r(t)^2} \frac{u_{R_d} f_{\nu_\alpha}(E, u_{R_d}, R_d, t)}{D(v, r(t))} dE du_{R_d}, \tag{5.11}$$

$$\lambda_c(t) = \frac{2\pi c}{(hc)^3} \sum_\alpha \int \sigma_\nu(E) \frac{R_d^2}{r(t)^2} \frac{u_{R_d} f_{\nu_\alpha}(E, u_{R_d}, R_d, t) P_{\alpha e}(E, u_{R_d}, r(t))}{D(v, r(t))} dE du_{R_d}, \tag{5.12}$$

where λ_0 and λ_c are the rates without and with neutrino oscillations. In the above equations, we use

$$\sigma_{\nu_e n} = 0.934 \times 10^{-43} \left(\frac{E_{\nu_e} + \Delta}{\rm MeV} \right)^2 \left[1 + 1.055 \times 10^{-3} \left(\frac{E_{\nu_e}}{\rm MeV} \right) \right] {\rm cm}^2, \tag{5.13}$$

$$\sigma_{\bar{\nu}_e p} = 0.934 \times 10^{-43} \left(\frac{E_{\bar{\nu}_e} - \Delta}{\rm MeV} \right)^2 \left[1 - 7.669 \times 10^{-3} \left(\frac{E_{\bar{\nu}_e}}{\rm MeV} \right) \right] {\rm cm}^2, \tag{5.14}$$

where $\Delta = m_n - m_p = 1.293$MeV, The cross-sections take into account weak magnetism and nucleon recoil but neglecting m_e in comparison with E_ν [85, 86].

We show $\lambda_0(t)$ and $\lambda_c(t)/\lambda_0(t)$ for $t_0 = 0.840$, 1.253, 1.726, and 2.526 second in Fig. 5.10. It shows that the effect of neutrino oscillations on the rates of neutrino capture on free nucleons is larger for the mass elements ejected earlier because flavor conversion becomes less significant at later time. Note that the effect on ν_e capture is larger than on $\bar{\nu}_e$ because the flavor conversions mostly happened in neutrino sector rather than in anti-neutrino sector. The effect on $\bar{\nu}_e$ capture basically diminishes after $t_0 \sim 1.253$ second while the effect on ν_e capture are in general non-negligible for $t_0 \lesssim 2.5$ second.

In addition, we show the nucleosynthesis-relevant temperature $T(t) = 1.0$, 0.6, 0.3, 0.2 and 0.1 MeV in the top axis of Fig. 5.10. It clearly shows that the effects of neutrino oscillations are important for $0.15 \lesssim T \lesssim 0.6$ MeV for ν_e and for $0.3 \lesssim T \lesssim 0.6$ MeV for $\bar{\nu}_e$. This indicates that collective oscillations do not hugely affect the heavy

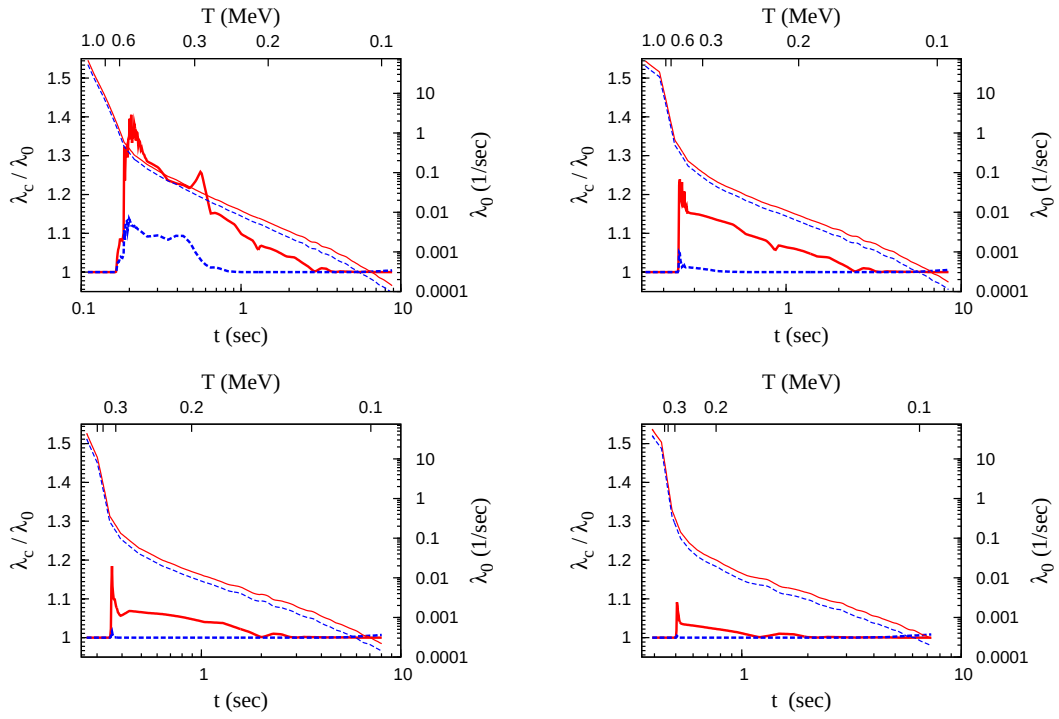

Figure 5.10: λ_0 (thin) and λ_c/λ_0 (thick) for ν_e (solid red) and $\bar{\nu}_e$ (dashed blue) for $t_0 = 0.840$ (top-left), 1.253 (top-right), 1.726 (bottom-left), and 2.526 (bottom-right) second.

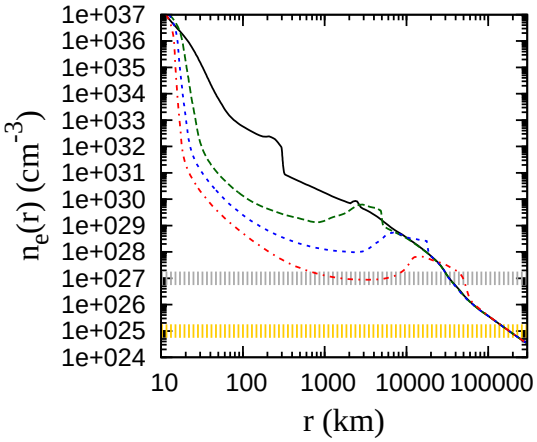

Figure 5.11: The electron number density n_e as a function of radius for different time snapshots $t_{\rm pb}$ = 200 ms(black solid), 1.0 s (green dashed) 3.0 s (blue dotted), and 10.0 s (red dotted-dash). The gray and yellow bands indicate the corresponding MSW resonance density for atmospheric and solar mass splitting, respectively.

element production in νp process because the production of elements in this process is proportional to the $\bar{\nu}_e$ capture rate on free proton for $0.1 \lesssim T \lesssim 0.3$ MeV. This conclusion is further confirmed by our nucleosynthesis calculation using the reaction network that was used in [70, 80].

5.4 Neutrino Signals in the IceCube Detector

After the collective oscillations, neutrinos then go through the subsequent MSW resonances in both atmospheric and solar scales at densities around $n_e \approx 10^{27}$ cm^{-3} and 10^{25} cm^{-3} as shown in Fig. 5.11. In this model, it turns out that both resonances are adiabatic, regardless of the presence of the multiple resonances due to the forward and reverse shocks at late time. Under adiabatic condition, one can easily show that the $\bar{\nu}_e$ energy spectrum after both resonances is [87]

$$\bar{f}^{(\rm f)}_{\bar{\nu}_e} = \begin{cases} c^2_{12}c^2_{13}\bar{f}^{(\rm i)}_{\bar{\nu}_e} + s^2_{12}c^2_{13}\bar{f}^{(\rm i)}_{\bar{\nu}_x} + s^2_{13}\bar{f}^{(\rm i)}_{\bar{\nu}_y}, & \text{for NH,} \\ s^2_{13}\bar{f}^{(\rm i)}_{\bar{\nu}_e} + s^2_{12}c^2_{13}\bar{f}^{(\rm i)}_{\bar{\nu}_x} + c^2_{12}c^2_{13}\bar{f}^{(\rm i)}_{\bar{\nu}_y}, & \text{for IH,} \end{cases} \tag{5.15}$$

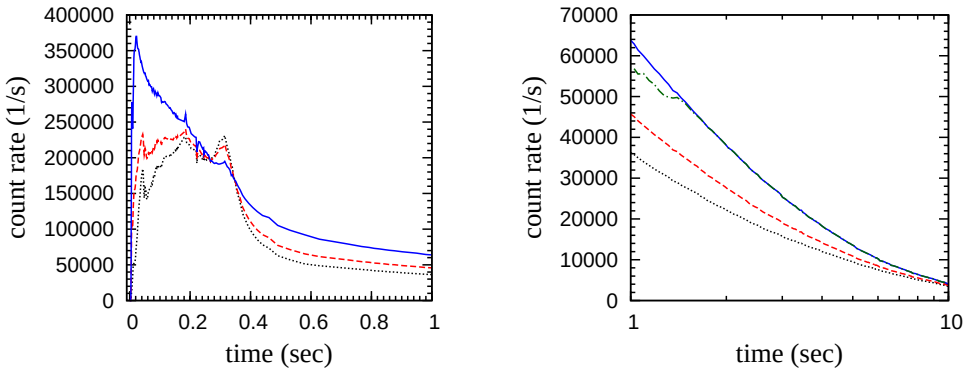

Figure 5.12: The event rate of $\bar{\nu}_e$ capture by protons in the IceCube detector as a function of time. The blue solid, red dashed, and black dotted line are for the case of IH, NH, and no oscillation. In the right panel, the green dash-dotted line shows the result that includes the effect of collective oscillations in IH.

where c_{ij} and s_{ij} stand for $\cos\theta_{ij}$ and $\sin\theta_{ij}$, $\bar{f}^{(\mathrm{i})}_{\bar{\nu}_\alpha}$ is the neutrino energy spectrum as defined in the previous section for α flavor before the MSW transition but after the collective oscillations.

We then calculate the event rate of $\bar{\nu}_e$ capture by protons per DOM in the IceCube detector by closely following the details in [12] :

$$R(t) = \frac{n_p L_n}{4\pi d^2} \int dE_{\bar{\nu}_e} \sigma_{\bar{\nu}_e p}(E_{\bar{\nu}_e}) N_\gamma(E_e) V_\gamma^{\mathrm{eff}} \tilde{f}^{(\mathrm{f})}_{\bar{\nu}_e}(E_{\bar{\nu}_e}), \tag{5.16}$$

where $n_p \approx 6.0 \times 10^{37}$ km^{-3} is the number density of protons, L_n is the number luminosity of $\bar{\nu}_e$, $d = 10$ kpc is the distance of the supernova, $\sigma_{\bar{\nu}_e p}$ is given in equation (5.13), $N_\gamma = 178 \frac{E_e}{\mathrm{MeV}}$ and $V_\gamma^{\mathrm{eff}} = 0.163$ m^3 are the number of Cherenkov photons and the effective volume of a single photon, $\tilde{f}^{(\mathrm{f})}_{\bar{\nu}_e}(E_{\bar{\nu}_e})$ is the normalized $\bar{\nu}_e$ energy spectrum when neutrinos leave the supernova. The total rates are multiplied by 5160, which is the current number of DOMs in IceCube. Note that we do not include the experimental factors such as the background rates, noise, and the efficiency in this simple calculation.

We show the result in Fig. 5.12. During the accretion phase as shown in the left panel, only the effect of MSW oscillations is included. This is because (1) the computational difficulty to achieve a self-consistent calculation of collective oscillations due to the

"neutrino halo" [31], and (2) the high matter density profile seems to suggest that the collective oscillations are suppressed even including the halo effect [44]. In this case, we see that the luminosity plateau during the accretion phase is still very robust for NH but is smoothed out for IH. This implies that it may be possible to test the unknown neutrino mass hierarchy from the signals. However, the possibility of extracting the onset of the shock revival may depend on the actual mass hierarchy of the neutrino mixing.

In the right panel, we show the expected signals during the cooling phase, including the effect of collective oscillations. The collective effect here is generally small and only visible for $t_{\rm pb} \lesssim 1.5$ second. This is anticipated because there is basically no collective flavor conversion for antineutrinos after $t_{\rm pb} \lesssim 1.5$ second as shown in Fig. 5.12.

5.5 Dependence on the Matter Density

In this section we discuss the effect of varying matter density on the results of collective oscillations. We manually lower the electron number density $n_e(r)$ above the neutrino sphere by a factor of two or five from the supernova simulation. The results of angle-energy-averaged neutrino flavor conversion probabilities $\left\langle P_{\nu_e\nu_y}\right\rangle_{v,E}$ as a function of radius for $t_{\rm pb} = 1.025$ and 5.0 seconds are shown in Fig. 5.13. Interestingly, the change of matter density has different effects on the two different flavor instabilities discussed in section 5.2.2. In the case of $t_{\rm pb} = 1.025$ second, the original higher n_e profile helps the flavor instability to start at a smaller radius. Also, this instability grows slower and stops when the overall flavor conversion is still small such that the second instability could occur. However, when the matter density n_e is lowered by a factor of two or five, the "first" instability starts at $r \approx 150$ km and grows largely such that no second instability occurs in these cases. We also show in Fig. 5.14 that sharp spectral swaps are formed when the density is lowered.

For $t_{\rm pb} = 5.0$ second, the onset of flavor conversion is pushed to larger radius and

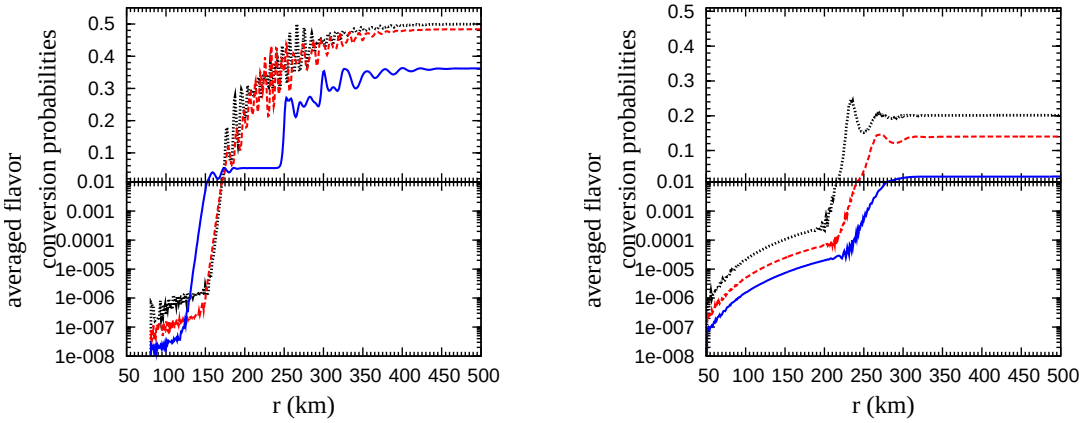

Figure 5.13: $\langle P_{\nu_e\nu_y} \rangle$ for $t_{\rm pb} = 1.025$ (left panel) and 5.0 (right panel) seconds with matter density of n_e (blue-solid), $0.5n_e$ (red-dashed) and $0.2n_e$ (black-dotted), where n_e is the density profile given by the supernova simulation.

grows slower to smaller value when the matter density is higher. As a result, fewer ν_e are converted to ν_y when n_e is larger. This behavior is generally true for most of the cooling phase when there is only one flavor instability at the larger radius. Note that the antineutrino spectrum is not affected by the change of n_e because the positive spectral crossing is in the neutrino spectrum only. We also note that larger n_e makes the local effective mixing angle smaller. This also reduces the degree of flavor conversion and is similar to the effect of choosing a tiny vacuum mixing angle. The different dependence on changing n_e of the two flavor instabilities suggests that those two instabilities are different kinds as discussed in [26].

For the normal mass hierarchy, the change of n_e does not have any visible effect on collective oscillations. This suggests that the suppression of oscillation in normal mass hierarchy is entirely due to the multi-angle effect from the neutrino-neutrino potential [33].

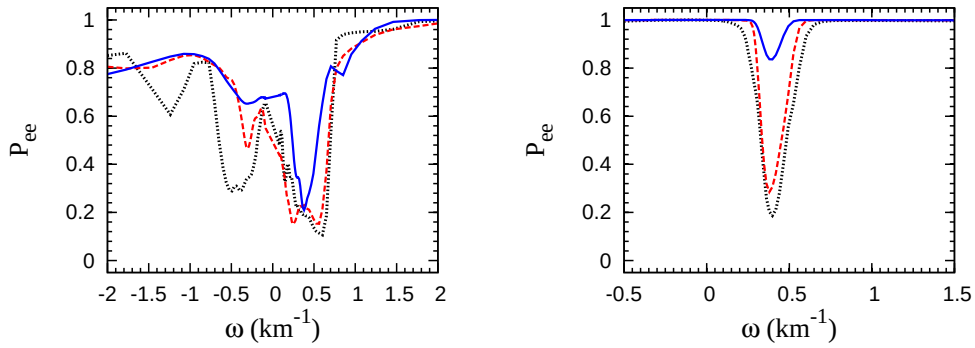

Figure 5.14: $\langle P_{\nu_e\nu_e}\rangle_v$ ($\omega > 0$) and $\langle P_{\bar{\nu}_e\bar{\nu}_e}\rangle_v$ ($\omega < 0$) at $r = 500$ km for $t_{\rm pb} = 1.025$ (left panel) and 5.0 (right panel) seconds with matter density of n_e (blue-solid), $0.5n_e$ (red-dashed) and $0.2n_e$ (black-dotted), where n_e is the density profile given by the supernova simulation.

5.6 Discussions and Summary

In this chapter, we numerically study the collective neutrino oscillations for the cooling phase between $1 \lesssim t_{\rm pb} \lesssim 10$ seconds using the neutrino emission and the density profiles from a state-of-the-art 18 $M_\odot$ supernova model. We show that the neutrino flavor evolution history and the survival probabilities are time-dependent because of the evolution of neutrino spectra and the supernova environment. In the early cooling phase, there exist two flavor instabilities and larger extent of flavor conversion could happen in the neutrino sector for the inverted mass hierarchy. However, the region of flavor conversion shrinks with time such that there is basically no flavor conversion for the antineutrino sector in most of the cooling phase we have studied. Furthermore, the collective neutrino oscillations eventually cease to occur at late cooling phase. As a result, we find little effect of oscillations on the neutrino capture rates on free nucleons such that the final production of heavy elements in the νp nucleosynthesis is not affected. We then include the MSW effect to calculate the event rate of $\bar{\nu}_e$ capture on protons in the IceCube detector. Although the effect of collective oscillations is small during the cooling phase, there is a strong possibility that the neutrino mass hierarchy could

be extracted from the neutrino signals during the accretion phase from the pure MSW effect.

The above results are based on the one-dimensional supernova model and the neutrino oscillation model with neutrino emitted from the energy-averaged neutrino spheres. However, many aspects of these models could be improved. One obvious example is the dependence on the matter density that we have shortly discussed which might be important in a realistic multi-dimensional supernova environment. Also, a more realistic treatment of neutrino decoupling which includes the energy-dependent neutrino spheres remains to be studied. Furthermore, the effect of the aforementioned neutrino "halo" [31], and the effect of the improved ν_e and $\bar{\nu}_e$ spectra from recently updated supernova models by including the mean-field potential of nucleons in the neutrino decoupling region [88, 89], are not included here. All those effects will have to be studied to provide us a more satisfactory understanding of neutrino oscillations and their effects on the related physical processes in supernovae.

Chapter 6

Conclusion

It is well-known from the nuclear-astrophysics side that neutrinos are a central piece of core-collapse supernova physics and participate in many physical processes that occur during the explosion. On the other hand, nearly all parameters of neutrino mixing but one sign of the mass-squared difference and the CP-violating phase have been measured by various experiments. This allows us to study more carefully the behavior of neutrino oscillations and their effects in supernovae.

In supernova environment with the active neutrino mixing scenario, three effects come in to shape the neutrino oscillations : the vacuum maxing, the neutrino-electron forward scattering, and the neutrino-neutrino forward scattering. The first two combined gives the famous MSW oscillations that occur in our Sun and the Earth. The third one couples the flavor evolution histories of different neutrinos to each other and is extremely important in the supernova context since the neutrino fluxes are very large near the proto-neutron star. As a result, collective neutrino oscillations happens at the innermost region of the supernovae prior to the MSW oscillations and might have significant effects on various processes such as the shock-revival and the nucleosynthesis in the neutrino-driven wind. However, due to the non-linear nature of the neutrino-neutrino coupling, the an-isotropic neutrino emission from the proto-neutron star, and

the time-evolving neutrino emission characteristics and the density profiles, it is a challenging task to understand the collective neutrino oscillations from both analytical and numerical points of view.

In this thesis, we have improved our understanding of this topic both analytically and numerically. In chapter 4, we use the "zeroth-order mean field" approximation to simplify this complicated problem. In zeroth-order, we assume that each part of the neutrino spectra between the spectra-crossing can be represented by a neutrino with the averaged vacuum frequency of the same part. This reduces the infinite degrees of freedom to merely a few numbers that can be analytically solved. We then study the detailed behavior of this simplified system and use the result to understand how the flavor evolution history of each neutrino with different energy and emission angle is. This model provides us a very good understanding of how the so-called "spectral splits/swaps" are formed in different phases of neutrino emission.

During the phase of the neutronization neutrino burst, using the zeroth-order mean field, we successfully explain that the formation of the spectral split is due to the non-adiabaticity of the zeroth-order mean field in the very steep density profile. Furthermore, we confirm that the low energy neutrinos centered around 3 MeV go through their MSW-like resonances non-adiabatically due to a bump of the density profile in the interface of the helium and hydrogen layers.

For the neutrino spectra with dominated ν_e and $\bar{\nu}_e$ compared with ν_x, which is similar to the neutrino emission during the accretion phase. We show that in the case of low matter density, the system in the zeroth-order mean field approximation acts as a gyroscope with precession and nutation. We calculate how this gyroscopic system evolves with radius in detail and find out that both precession and nutation of the gyroscope would induce different type of resonances for neutrinos. The formation of the spectral splits can then be explained by simply counting the number of resonances that a neutrino goes through as it propagates outward.

We then study the early onset of the neutrino flavor instability that occurs during

the cooling phase of neutrino emission under the single-angle approximation. We show that this instability generally exists for a system with more than two NFIS's. We then show that a three-NFIS system in the high density limit can be equivalently treated as a two-NFIS system in low density such that large flavor conversion could occur. We point out at last that a detailed numerical study is needed for studying neutrino oscillations in the cooling phase.

In chapter 5, we numerically study the collective neutrino oscillations in the cooling phase using the neutrino emission and the density profiles from a state-of-the-art supernova model. We show that due to the time evolution of neutrino spectra and the supernova environment, the neutrino flavor evolution history and the survival probabilities are time-dependent. This is very important when applying the results of neutrino oscillations to study the possible effects on the nucleosynthesis because the time scale for neutrinos to go through the region of oscillations is very different from the time scale for the wind. In this model, we find that collective neutrino oscillations only occur at very early cooling phase and the region of flavor conversion only exist mostly between roughly 8 and 20 MeV. As a result, the collective oscillations have little effect on the neutrino capture rates on free nucleons and the nucleosynthesis in the neutrino-driven wind. In addition, we calculate the expected event rates of $\bar{\nu}_e$ capture on protons in the IceCube detector. Although the effect of collective oscillations is small, there is a strong possibility that the neutrino mass hierarchy could be extracted from the neutrino signals during the accretion phase from the pure MSW effect.

At last, as we have already briefly mentioned at the end of chapter 5, there are many uncertainties and effects in the models of both supernovae and neutrino oscillations that need to be included. Although our understanding of neutrino oscillations in supernovae has been improved greatly in the last decade through numerous efforts, it is still far from complete. With its importance, we expect more theoretical works to be done in the near future such that we will be ready to welcome the first galactic supernova neutrino signals when they come!

References

[1] S.E. Woosley, A. Heger, and T.A. Weaver. The evolution and explosion of massive stars. *Rev.Mod.Phys.*, 74:1015–1071, 2002.

[2] Alexander Heger, C.L. Fryer, S.E. Woosley, N. Langer, and D.H. Hartmann. How massive single stars end their life. *Astrophys.J.*, 591:288–300, 2003, astro-ph/0212469.

[3] F.S. Kitaura, Hans-Thomas Janka, and W. Hillebrandt. Explosions of O-Ne-Mg cores, the Crab supernova, and subluminous type II-P supernovae. *Astron.Astrophys.*, 450:345–350, 2006, astro-ph/0512065.

[4] H.-Th. Janka, B. Mueller, F.S. Kitaura, and R. Buras. Dynamics of shock propagation and nucleosynthesis conditions in O-Ne-Mg core supernovae. 2007, 0712.4237.

[5] T. Fischer, S.C. Whitehouse, A. Mezzacappa, F.-K. Thielemann, and M. Liebendorfer. Protoneutron star evolution and the neutrino driven wind in general relativistic neutrino radiation hydrodynamics simulations. *Astron.Astrophys.*, 517:A80, 2010, 0908.1871.

[6] H. Thomas Janka. Explosion Mechanisms of Core-Collapse Supernovae. 2012, 1206.2503.

[7] A. Arcones and F.-K. Thielemann. Neutrino-driven wind simulations and nucleosynthesis of heavy elements. 2012, 1207.2527.

[8] Takashi Yoshida, Toshitaka Kajino, Hidekazu Yokomakura, Keiichi Kimura, Akira Takamura, et al. Neutrino Oscillation Effects on Supernova Light Element Synthesis. *Astrophys.J.*, 649:319–331, 2006, astro-ph/0606042.

[9] Projjwal Banerjee, W.C. Haxton, and Yong-Zhong Qian. A Long, Cold, Early r-process? Neutrino-induced Nucleosynthesis in He Shells Revisited. *Phys.Rev.Lett.*, 106:201104, 2011, 1103.1193.

[10] J. Beringer et al. Review of Particle Physics (RPP). *Phys.Rev.*, D86:010001, 2012.

[11] Georg G. Raffelt. New opportunities with supernova neutrinos. *Nucl.Phys.Proc.Suppl.*, 217:95–100, 2011.

[12] R. Abbasi et al. IceCube Sensitivity for Low-Energy Neutrinos from Nearby Supernovae. *Astron.Astrophys.*, 535:A109, 2011, 1108.0171.

[13] Kate Scholberg. Supernova Neutrino Detection. 2012, 1205.6003.

[14] R. Davis. A review of the Homestake solar neutrino experiment. *Prog.Part.Nucl.Phys.*, 32:13–32, 1994.

[15] K. Hirata et al. Observation of a Neutrino Burst from the Supernova SN 1987a. *Phys.Rev.Lett.*, 58:1490–1493, 1987.

[16] R.M. Bionta, G. Blewitt, C.B. Bratton, D. Casper, A. Ciocio, et al. Observation of a Neutrino Burst in Coincidence with Supernova SN 1987a in the Large Magellanic Cloud. *Phys.Rev.Lett.*, 58:1494, 1987.

[17] L. Wolfenstein. Neutrino Oscillations in Matter. *Phys.Rev.*, D17:2369–2374, 1978.

[18] S.P. Mikheev and A. Yu. Smirnov. Resonance Amplification of Oscillations in Matter and Spectroscopy of Solar Neutrinos. *Sov.J.Nucl.Phys.*, 42:913–917, 1985.

[19] G. M. Fuller, R. W. Mayle, J. R. Wilson, and D. N. Schramm. Resonant neutrino oscillations and stellar collapse. *Astrophys.J.*, 322:795–803, 1987.

[20] James T. Pantaleone. Neutrino oscillations at high densities. *Phys.Lett.*, B287:128–132, 1992.

[21] G. Sigl and G. Raffelt. General kinetic description of relativistic mixed neutrinos. *Nucl.Phys.*, B406:423–451, 1993.

[22] A.B. Balantekin and H. Yuksel. Neutrino mixing and nucleosynthesis in core-collapse supernovae. *New J.Phys.*, 7:51, 2005, astro-ph/0411159.

[23] George M. Fuller and Yong-Zhong Qian. Simultaneous flavor transformation of neutrinos and antineutrinos with dominant potentials from neutrino-neutrino forward scattering. *Phys.Rev.*, D73:023004, 2006, astro-ph/0505240.

[24] Huaiyu Duan, George M. Fuller, and Yong-Zhong Qian. Collective neutrino flavor transformation in supernovae. *Phys.Rev.*, D74:123004, 2006, astro-ph/0511275.

[25] Huaiyu Duan, George M. Fuller, and Yong-Zhong Qian. Collective Neutrino Oscillations. *Ann.Rev.Nucl.Part.Sci.*, 60:569–594, 2010, 1001.2799.

[26] Arka Banerjee, Amol Dighe, and Georg Raffelt. Linearized flavor-stability analysis of dense neutrino streams. *Phys.Rev.*, D84:053013, 2011, 1107.2308.

[27] Sovan Chakraborty, Tobias Fischer, Alessandro Mirizzi, Ninetta Saviano, and Ricard Tomas. No collective neutrino flavor conversions during the supernova accretion phase. *Phys.Rev.Lett.*, 107:151101, 2011, 1104.4031.

[28] Sovan Chakraborty, Tobias Fischer, Alessandro Mirizzi, Ninetta Saviano, and Ricard Tomas. Analysis of matter suppression in collective neutrino oscillations during the supernova accretion phase. *Phys.Rev.*, D84:025002, 2011, 1105.1130.

[29] John F. Cherry, Meng-Ru Wu, J. Carlson, Huaiyu Duan, George M. Fuller, et al. Density Fluctuation Effects on Collective Neutrino Oscillations in O-Ne-Mg Core-Collapse Supernovae. *Phys.Rev.*, D84:105034, 2011, 1108.4064.

[30] John F. Cherry, Meng-Ru Wu, J. Carlson, Huaiyu Duan, George M. Fuller, et al. Neutrino Luminosity and Matter-Induced Modification of Collective Neutrino Flavor Oscillations in Supernovae. *Phys.Rev.*, D85:125010, 2012, 1109.5195.

[31] John F. Cherry, J. Carlson, Alexander Friedland, George M. Fuller, and Alexey Vlasenko. Neutrino scattering and flavor transformation in supernovae. *Phys.Rev.Lett.*, 108:261104, 2012, 1203.1607.

[32] Basudeb Dasgupta, Alessandro Mirizzi, Irene Tamborra, and Ricard Tomas. Neutrino mass hierarchy and three-flavor spectral splits of supernova neutrinos. *Phys.Rev.*, D81:093008, 2010, 1002.2943.

[33] Huaiyu Duan and Alexander Friedland. Self-induced suppression of collective neutrino oscillations in a supernova. *Phys.Rev.Lett.*, 106:091101, 2011, 1006.2359.

[34] John F. Cherry, George M. Fuller, J. Carlson, Huaiyu Duan, and Yong-Zhong Qian. Multi-Angle Simulation of Flavor Evolution in the Neutrino Neutronization Burst From an O-Ne-Mg Core-Collapse Supernova. *Phys.Rev.*, D82:085025, 2010, 1006.2175.

[35] Alexander Friedland. Self-refraction of supernova neutrinos: mixed spectra and three-flavor instabilities. *Phys.Rev.Lett.*, 104:191102, 2010, 1001.0996.

[36] S. Galais, J. Kneller, and C. Volpe. The neutrino-neutrino interaction effects in supernovae: the point of view from the matter basis. *J.Phys.G*, G39:035201, 2012, 1102.1471.

[37] Sebastien Galais and Cristina Volpe. The neutrino spectral split in core-collapse supernovae: a magnetic resonance phenomenon. *Phys.Rev.*, D84:085005, 2011, 1103.5302.

[38] Alessandro Mirizzi and Ricard Tomas. Multi-angle effects in self-induced oscillations for different supernova neutrino fluxes. *Phys.Rev.*, D84:033013, 2011, 1012.1339.

[39] Alessandro Mirizzi and Pasquale D. Serpico. Instability in the Dense Supernova Neutrino Gas with Flavor-Dependent Angular Distributions. *Phys.Rev.Lett.*, 108:231102, 2012, 1110.0022.

[40] Alessandro Mirizzi and Pasquale Dario Serpico. Flavor stability analysis of dense supernova neutrinos with flavor-dependent angular distributions. 2012, 1208.0157.

[41] Y. Pehlivan, A.B. Balantekin, Toshitaka Kajino, and Takashi Yoshida. Invariants of Collective Neutrino Oscillations. *Phys.Rev.*, D84:065008, 2011, 1105.1182.

[42] Georg G. Raffelt. N-mode coherence in collective neutrino oscillations. *Phys.Rev.*, D83:105022, 2011, 1103.2891.

[43] Srdjan Sarikas, Georg G. Raffelt, Lorenz Hudepohl, and Hans-Thomas Janka. Suppression of Self-Induced Flavor Conversion in the Supernova Accretion Phase. *Phys.Rev.Lett.*, 108:061101, 2012, 1109.3601.

[44] Srdjan Sarikas, Irene Tamborra, Georg Raffelt, Lorenz Hudepohl, and Hans-Thomas Janka. Supernova neutrino halo and the suppression of self-induced flavor conversion. *Phys.Rev.*, D85:113007, 2012, 1204.0971.

[45] Ninetta Saviano, Sovan Chakraborty, Tobias Fischer, and Alessandro Mirizzi. Stability analysis of collective neutrino oscillations in the supernova accretion phase with realistic energy and angle distributions. *Phys.Rev.*, D85:113002, 2012, 1203.1484.

[46] Meng-Ru Wu and Yong-Zhong Qian. Resonances Driven by a Neutrino Gyroscope and Collective Neutrino Oscillations in Supernovae. *Phys.Rev.*, D84:045009, 2011, 1105.2068.

[47] H.A. Bethe. Supernova mechanisms. *Rev.Mod.Phys.*, 62:801–866, 1990.

[48] Stirling A. Colgate and Montgomery H. Johnson. Hydrodynamic Origin of Cosmic Rays. *Phys.Rev.Lett.*, 5:235–238, 1960.

[49] Stirling A. Colgate and Richard H. White. The Hydrodynamic Behavior of Supernovae Explosions. *Astrophys.J.*, 143:626, 1966.

[50] T. Fischer, G. Martinez-Pinedo, M. Hempel, and M. Liebendorfer. Neutrino spectra evolution during proto-neutron star deleptonization. *Phys.Rev.*, D85:083003, 2012, 1112.3842.

[51] C.W. Kim, W.K. Sze, and Shmuel Nussinov. ON NEUTRINO OSCILLATIONS AND THE LANDAU-ZENER FORMULA. *Phys.Rev.*, D35:4014, 1987.

[52] Sergio Pastor, Georg G. Raffelt, and Dmitry V. Semikoz. Physics of synchronized neutrino oscillations caused by selfinteractions. *Phys.Rev.*, D65:053011, 2002, hep-ph/0109035.

[53] Huaiyu Duan, George M. Fuller, J Carlson, and Yong-Zhong Qian. Simulation of Coherent Non-Linear Neutrino Flavor Transformation in the Supernova Environment. 1. Correlated Neutrino Trajectories. *Phys.Rev.*, D74:105014, 2006, astro-ph/0606616.

[54] Gianluigi L. Fogli, Eligio Lisi, Antonio Marrone, and Alessandro Mirizzi. Collective neutrino flavor transitions in supernovae and the role of trajectory averaging. *JCAP*, 0712:010, 2007, 0707.1998.

[55] Basudeb Dasgupta, Amol Dighe, Georg G. Raffelt, and Alexei Yu. Smirnov. Multiple Spectral Splits of Supernova Neutrinos. *Phys.Rev.Lett.*, 103:051105, 2009, 0904.3542.

[56] K. Nomoto. Evolution of 8-10 solar mass stars toward electron capture supernovae. I - Formation of electron-degenerate O + NE + MG cores. *Astrophys.J.*, 277:791–805, February 1984.

[57] K. Nomoto. Evolution of 8-10 solar mass stars toward electron capture supernovae. II - Collapse of an O + NE + MG core. *Astrophys.J.*, 322:206–214, November 1987.

[58] Huaiyu Duan, George M. Fuller, and Yong-Zhong Qian. A Simple Picture for Neutrino Flavor Transformation in Supernovae. *Phys.Rev.*, D76:085013, 2007, 0706.4293.

[59] Basudeb Dasgupta, Amol Dighe, Alessandro Mirizzi, and Georg G. Raffelt. Spectral split in prompt supernova neutrino burst: Analytic three-flavor treatment. *Phys.Rev.*, D77:113007, 2008, 0801.1660.

[60] Huaiyu Duan, George M. Fuller, J. Carlson, and Yong-Zhong Qian. Flavor Evolution of the Neutronization Neutrino Burst from an O-Ne-Mg Core-Collapse Supernova. *Phys.Rev.Lett.*, 100:021101, 2008, 0710.1271.

[61] Huaiyu Duan, George M. Fuller, and Yong-Zhong Qian. Stepwise spectral swapping with three neutrino flavors. *Phys.Rev.*, D77:085016, 2008, 0801.1363.

[62] A. Esteban-Pretel, A. Mirizzi, S. Pastor, R. Tomas, G.G. Raffelt, et al. Role of dense matter in collective supernova neutrino transformations. *Phys.Rev.*, D78:085012, 2008, 0807.0659.

[63] Steen Hannestad, Georg G. Raffelt, Gunter Sigl, and Yvonne Y.Y. Wong. Self-induced conversion in dense neutrino gases: Pendulum in flavour space. *Phys.Rev.*, D74:105010, 2006, astro-ph/0608695.

[64] Huaiyu Duan, George M. Fuller, J. Carlson, and Yong-Zhong Qian. Analysis of Collective Neutrino Flavor Transformation in Supernovae. *Phys.Rev.*, D75:125005, 2007, astro-ph/0703776.

[65] Georg G. Raffelt and Alexei Yu. Smirnov. Self-induced spectral splits in supernova neutrino fluxes. *Phys.Rev.*, D76:081301, 2007, 0705.1830.

[66] Huaiyu Duan, George M. Fuller, and Yong-Zhong Qian. Symmetries in collective neutrino oscillations. *J.Phys.G*, G36:105003, 2009, 0808.2046.

[67] Georg G. Raffelt and Alexei Yu. Smirnov. Adiabaticity and spectral splits in collective neutrino transformations. *Phys.Rev.*, D76:125008, 2007, 0709.4641.

[68] Georg G. Raffelt. Self-induced parametric resonance in collective neutrino oscillations. *Phys.Rev.*, D78:125015, 2008, 0810.1407.

[69] Huaiyu Duan, Alexander Friedland, Gail C. McLaughlin, and Rebecca Surman. The influence of collective neutrino oscillations on a supernova r-process. *J.Phys.G*, G38:035201, 2011, 1012.0532.

[70] G. Martínez-Pinedo, B. Ziebarth, T. Fischer, and K. Langanke. Effect of collective neutrino flavor oscillations on νp-process nucleosynthesis. *European Physical Journal A*, 47:98, August 2011, 1105.5304.

[71] Jerome Gava, James Kneller, Cristina Volpe, and G.C. McLaughlin. A Dynamical collective calculation of supernova neutrino signals. *Phys.Rev.Lett.*, 103:071101, 2009, 0902.0317.

[72] M. Liebendoerfer, O.E.B. Messer, A. Mezzacappa, S.W. Bruenn, C.Y. Cardall, et al. A Finite difference representation of neutrino radiation hydrodynamics for spherically symmetric general relativistic supernova simulations. *Astrophys.J.Suppl.*, 150:263–316, 2004, astro-ph/0207036.

[73] H. Shen, H. Toki, K. Oyamatsu, and K. Sumiyoshi. Relativistic equation of state of nuclear matter for supernova and neutron star. *Nucl.Phys.*, A637:435–450, 1998, nucl-th/9805035.

[74] F. X. Timmes and D. Arnett. *Astrophys. J. Suppl.*, 125:277, 1999.

[75] J.M. LeBlanc and J.R. Wilson. A Numerical Example of the Collapse of a Rotating Magnetized Star. *Astrophys.J.*, 161:541, 1970.

[76] Adam Burrows, Eli Livne, Luc Dessart, Christian Ott, and Jeremiah Murphy. A new mechanism for core-collapse supernova explosions. *Astrophys.J.*, 640:878–890, 2006, astro-ph/0510687.

[77] Hans A. Bethe and R. Wilson, James. Revival of a stalled supernova shock by neutrino heating. *Astrophys.J.*, 295:14–23, 1985.

[78] I. Sagert, T. Fischer, M. Hempel, G. Pagliara, J. Schaffner-Bielich, et al. Signals of the QCD phase transition in core-collapse supernovae. *Phys.Rev.Lett.*, 102:081101, 2009, 0809.4225.

[79] T. Fischer, I. Sagert, G. Pagliara, M. Hempel, J. Schaffner-Bielich, et al. Core-collapse supernova explosions triggered by a quark-hadron phase transition during the early post-bounce phase. *Astrophys.J.Suppl.*, 194:39, 2011, 1011.3409.

[80] C. Frohlich, Gabriel Martinez-Pinedo, M. Liebendorfer, F.-K. Thielemann, E. Bravo, et al. Neutrino-induced nucleosynthesis of A>64 nuclei: the nu p-process. *Phys.Rev.Lett.*, 96:142502, 2006, astro-ph/0511376.

[81] Jason Pruet, R.D. Hoffman, S.E. Woosley, H.-T. Janka, and R. Buras. Nucleosynthesis in early supernova winds. 2. the role of neutrinos. *Astrophys.J.*, 644:1028–1039, 2006, astro-ph/0511194.

[82] Y.Z. Qian and S.E. Woosley. Nucleosynthesis in neutrino driven winds: 1. The Physical conditions. *Astrophys.J.*, 471:331–351, 1996, astro-ph/9611094.

[83] Basudeb Dasgupta and Amol Dighe. Collective three-flavor oscillations of supernova neutrinos. *Phys.Rev.*, D77:113002, 2008, 0712.3798.

[84] K. Nakamura et al. Review of particle physics. *J.Phys.G*, G37:075021, 2010.

[85] C.J. Horowitz and Gang Li. Charge conjugation violating interactions in supernovae and nucleosynthesis. *Phys.Rev.Lett.*, 82:5198, 1999, astro-ph/9904171.

[86] P. Vogel and John F. Beacom. Angular distribution of neutron inverse beta decay, anti-neutrino(e) + p $\rightarrow$ e+ + n. *Phys.Rev.*, D60:053003, 1999, hep-ph/9903554.

[87] Amol S. Dighe and Alexei Yu. Smirnov. Identifying the neutrino mass spectrum from the neutrino burst from a supernova. *Phys.Rev.*, D62:033007, 2000, hep-ph/9907423.

[88] G. Martinez-Pinedo, T. Fischer, A. Lohs, and L. Huther. Charged-current weak interaction processes in hot and dense matter and its impact on the spectra of neutrinos emitted from proto-neutron star cooling. 2012, 1205.2793.

[89] Luke F. Roberts and Sanjay Reddy. Medium modification of the charged current neutrino opacity and its implications. 2012, 1205.4066.

[90] F.P. An et al. Observation of electron-antineutrino disappearance at Daya Bay. *Phys.Rev.Lett.*, 108:171803, 2012, 1203.1669.

Appendix A

Supplemental Calculation for Neutrino Gyroscope

A.1 Parameters of the Neutrino Gyroscope at a specific μ

In addition to the procedure given in Sec. 4.2.2, the parameters of the neutrino gyroscope at a specific μ can be obtained using the "pure-precession" ansatz (see also discussion in [64]), which assumes that $\mathbf{s}_1$ and $\mathbf{s}_2$ associated with the gyroscope always stay in the same plane as $\mathbf{H}_\nu = -\hat{\mathbf{e}}_z^{\mathrm{I}}$ and precess with the same angular velocity $\dot{\phi}_p \hat{\mathbf{e}}_z^{\mathrm{I}}$. More specifically, we can use the Euler angles in Frame I to write

$$\mathbf{s}_1 = \frac{1}{2}(\sin\theta_1 \sin\phi_1 \hat{\mathbf{e}}_x^{\mathrm{I}} - \sin\theta_1 \cos\phi_1 \hat{\mathbf{e}}_y^{\mathrm{I}} + \cos\theta_1 \hat{\mathbf{e}}_z^{\mathrm{I}}), \tag{A.1}$$

$$\mathbf{s}_2 = \frac{1}{2}(\sin\theta_2 \sin\phi_2 \hat{\mathbf{e}}_x^{\mathrm{I}} - \sin\theta_2 \cos\phi_2 \hat{\mathbf{e}}_y^{\mathrm{I}} + \cos\theta_2 \hat{\mathbf{e}}_z^{\mathrm{I}}). \tag{A.2}$$

The ansatz assumes that $\dot{\theta}_1 = \dot{\theta}_2 = 0$, $\dot{\phi}_1 = \dot{\phi}_2 = \dot{\phi}_p$, and $\phi_2 - \phi_1 = \pi$ (the last relation can be seen from the initial configuration at the neutrino sphere with $\mathbf{s}_1 = -\mathbf{s}_2 = \hat{\mathbf{e}}_z^{\mathrm{f}}/2$ corresponding to $\theta_1 = 2\tilde{\theta}_\nu$ and $\theta_2 = \pi - 2\tilde{\theta}_\nu$). Using this ansatz along with conservation of S_z and Eqs. (4.24) and (4.25), we obtain

$$\cos\theta_1 + \alpha \cos\theta_2 = (1-\alpha)\cos 2\tilde{\theta}_\nu, \tag{A.3}$$

$$\dot{\phi}_p \sin\theta_1 = \mu_{\rm v} \sin\theta_1 + \frac{\alpha\mu}{2}\sin(\theta_1+\theta_2), \tag{A.4}$$

$$\dot{\phi}_p \sin\theta_2 = -\mu_{\rm v} \sin\theta_2 + \frac{\mu}{2}\sin(\theta_1+\theta_2). \tag{A.5}$$

For any specific μ, the above equations can be solved to give θ_1, θ_2, and $\dot{\phi}_p$. Then we can calculate the corresponding σ, Q, and θ_p using θ_1 and θ_2. The above procedure gives σ, Q, θ_p, and $\dot{\phi}_p$ for the gyroscope at a specific μ that are indistinguishable from those obtained by the procedure discussed in Sec. 4.2.2.

A.2 Initial Conditions for the Neutrino Gyroscope

The initial conditions for the neutrino gyroscope at the neutrino sphere are

$$\mathbf{S}(0) = \frac{1-\alpha}{2}\hat{\mathbf{e}}_z^{\rm f}, \tag{A.6}$$

$$\mathbf{Q}(0) = \frac{1+\alpha}{2}\hat{\mathbf{e}}_z^{\rm f} + \frac{\mu_{\rm v}}{\mu}\mathbf{H}_{\rm v}. \tag{A.7}$$

Noting that $\mathbf{H}_{\rm v} = -\sin 2\tilde{\theta}_{\rm v}\hat{\mathbf{e}}_x^{\rm f} - \cos 2\tilde{\theta}_{\rm v}\hat{\mathbf{e}}_z^{\rm f} = -\hat{\mathbf{e}}_z^{\rm I}$, we obtain from the above equations

$$S_z = \frac{1-\alpha}{2}\cos 2\tilde{\theta}_{\rm v}, \tag{A.8}$$

$$Q = \left[\left(\frac{1+\alpha}{2} - \frac{\mu_{\rm v}}{\mu}\cos 2\tilde{\theta}_{\rm v}\right)^2 + \left(\frac{\mu_{\rm v}}{\mu}\sin 2\tilde{\theta}_{\rm v}\right)^2\right]^{1/2}, \tag{A.9}$$

$$\sigma = \frac{1-\alpha}{2Q}\left(\frac{1+\alpha}{2} - \frac{\mu_{\rm v}}{\mu}\cos 2\tilde{\theta}_{\rm v}\right). \tag{A.10}$$

In terms of the dynamic variables θ and ϕ, the initial conditions for the neutrino gyroscope can be chosen as $\dot{\theta}_0 = 0$, $\phi_0 = 0$, and

$$\cos\theta_0 = \frac{1}{Q}\left(\frac{1+\alpha}{2}\cos 2\tilde{\theta}_{\rm v} - \frac{\mu_{\rm v}}{\mu}\right), \tag{A.11}$$

$$\dot{\phi}_0 = \mu_{\rm v}\frac{1-\alpha}{1+\alpha}, \tag{A.12}$$

where the subscript "0" indicates the initial moment $t = 0$ and Eq. (A.12) is obtained from Eq. (4.26) at $t = 0$. For a constant μ, the precession frequency at $\theta = \theta_p$, where

$V_{\rm eff}(\theta)$ reaches its minimum, is given by Eq. (4.42) as

$$\dot{\phi}_p = \frac{\mu\sigma \pm \sqrt{(\mu\sigma)^2 - 4\mu\mu_{\rm v}Q\cos\theta_p}}{2\cos\theta_p} \approx \begin{cases} (\mu\sigma/\cos\theta_p) - (\mu_{\rm v}Q/\sigma), \\ \mu_{\rm v}Q/\sigma, \end{cases} \tag{A.13}$$

where the approximate equalities apply for $\mu_{\rm v}/\mu \ll 1$ with the upper and lower expressions corresponding to the plus and minus signs in front of the square root, respectively. It can be shown that the upper expression of $\dot{\phi}_p$ is unphysical as it cannot satisfy conservation of S_z. For the physical value of $\dot{\phi}_p \approx \mu_{\rm v}Q/\sigma$, conservation of S_z gives

$$\theta_p \approx 2\tilde{\theta}_{\rm v}\left[1 + \frac{2(1+\alpha)}{(1-\alpha)^2}\frac{\mu_{\rm v}}{\mu}\right]. \tag{A.14}$$

The above expression of θ_p is to the first order in $\mu_{\rm v}/\mu$ and $\tilde{\theta}_{\rm v}$. To the same order, we have

$$\theta_0 \approx 2\tilde{\theta}_{\rm v}\left(1 + \frac{2}{1+\alpha}\frac{\mu_{\rm v}}{\mu}\right). \tag{A.15}$$

The amplitude of nutation around $\theta = \theta_p$ is then

$$\eta = \theta_p - \theta_0 \approx \frac{16\alpha\tilde{\theta}_{\rm v}}{(1+\alpha)(1-\alpha)^2}\frac{\mu_{\rm v}}{\mu}. \tag{A.16}$$

The number density of ν_e at the neutrino sphere is

$$n_{\nu_e}(R_\nu) = \frac{L_{\nu_e}}{4\pi R_\nu^2\langle E_{\nu_e}\rangle} = 1.66\times10^{32}\left(\frac{L_{\nu_e}}{10^{51}\ {\rm erg/s}}\right)\left(\frac{10\ {\rm km}}{R_\nu}\right)^2\left(\frac{10\ {\rm MeV}}{\langle E_{\nu_e}\rangle}\right)\ {\rm cm}^{-3}. \tag{A.17}$$

For $\mu = 2\sqrt{2}G_F n_{\nu_e}(R_\nu)$,

$$\frac{\mu_{\rm v}}{\mu} = 5.92\times10^{-6}\left(\frac{\delta m^2}{3\times10^{-3}\ {\rm eV}^2}\right)\left(\frac{10\,{\rm MeV}}{E}\right)\left[\frac{10^{32}\ {\rm cm}^{-3}}{n_{\nu_e}(R_\nu)}\right]. \tag{A.18}$$

Taking $\tilde{\theta}_{\rm v} = 10^{-5}$, $\delta m^2 = 3\times10^{-3}$ eV^2, $2\mu_{\rm v}/\delta m^2 = 1/9$ MeV^{-1}, $\alpha = 2/3$, and $n_{\nu_e}(R_\nu) = 1.66\times10^{32}$ cm^{-3}, we have $\eta \approx 2.28\times10^{-9}$.

A.3 The Neutrino Gyroscope at the Critical Point

The critical point at $\mu = \mu_{\rm cr}$ separates the evolution of the neutrino gyroscope into two regimes: the sleeping-top regime with essentially pure precession but little nutation at

$\mu \gtrsim \mu_{\rm cr}$ and the other with both precession and nutation at $\mu < \mu_{\rm cr}$. As $\theta \ll 1$ in the sleeping-top regime, we derive $\mu_{\rm cr}$ assuming $\tilde{\theta}_{\rm v} = 0$. Let the gyroscope start with $\theta = 0$ at a constant μ. Its fixed parameters are

$$S_z = \sigma = \frac{1-\alpha}{2}, \tag{A.19}$$

$$Q = \frac{1+\alpha}{2} - \frac{\mu_{\rm v}}{\mu}, \tag{A.20}$$

$$E_{\rm gyro} = \frac{\mu}{2}\sigma^2 + \mu_{\rm v} Q. \tag{A.21}$$

The motion of the gyroscope is governed by

$$\frac{\dot{\phi}}{\mu}\sin^2\theta = \sigma(1-\cos\theta), \tag{A.22}$$

$$\frac{1}{2\mu}(\dot{\theta}^2 + \dot{\phi}^2\sin^2\theta) = \mu_{\rm v} Q(1-\cos\theta), \tag{A.23}$$

which are obtained by rewriting Eqs. (4.34) and (4.36). Assuming that $\theta > 0$ is allowed, we can find $\theta_{\rm max}$, the maximum value of θ, by setting $\dot{\theta} = 0$ in Eq. (A.23). Combining the resulting equation with Eq. (A.22), we obtain

$$\cos\theta_{\rm max} = \frac{\mu\sigma^2}{2\mu_{\rm v} Q} - 1. \tag{A.24}$$

It can be seen that when $\mu\sigma^2 \geq 4\mu_{\rm v} Q$, the above equation has no solution for $\theta_{\rm max} > 0$. Thus, the gyroscope remains in its initial vertical position ($\theta = 0$) for $\mu\sigma^2 \geq 4\mu_{\rm v} Q$. For a gyroscope starting at $\mu \gg \mu_{\rm v}$, this condition corresponds to $\mu \geq \mu_{\rm cr}$, where

$$\mu_{\rm cr} \equiv \frac{4\mu_{\rm v}}{(1-\sqrt{\alpha})^2}. \tag{A.25}$$

Expanding $S_z = (1-\alpha)\cos 2\tilde{\theta}_{\rm v}/2$ to the leading order in $\tilde{\theta}_{\rm v}$, we obtain the pure-precession solution at $\mu = \mu_{\rm cr}$ from Eqs. (4.42), (4.50), (4.52), and (4.53) (setting $\eta = 0$ in the last equation):

$$\sigma_{\rm cr} \approx \sigma^{(0)}\left[1 - \frac{(1-\sqrt{\alpha})^2}{8\sqrt{2\alpha}}\theta_{p,{\rm cr}}^3\right], \tag{A.26}$$

$$Q_{\rm cr} \approx Q^{(0)}\left[1 + \frac{(1-\sqrt{\alpha})^2}{4\sqrt{2\alpha}}\theta_{p,{\rm cr}}^3\right], \tag{A.27}$$

$$\theta_{p,\mathrm{cr}} \approx \frac{2\sqrt{2}\alpha^{1/6}}{(1+\sqrt{\alpha})^{2/3}}\tilde{\theta}_{\mathrm{v}}^{2/3}, \tag{A.28}$$

$$\dot{\phi}_{p,\mathrm{cr}} \approx \dot{\phi}_p^{(0)}\left(1-\frac{\theta_{p,\mathrm{cr}}}{\sqrt{2}}+\frac{1+\alpha}{4\sqrt{2}}\theta_{p,\mathrm{cr}}^2\right), \tag{A.29}$$

where $\sigma^{(0)} = (1-\alpha)/2$, $Q^{(0)} = (1+\alpha)/2 - \mu_{\mathrm{v}}/\mu_{\mathrm{cr}}$, and $\dot{\phi}_p^{(0)} = \mu_{\mathrm{cr}}\sigma^{(0)}/2$. For $\alpha = 2/3$ and $\tilde{\theta}_{\mathrm{v}} = 10^{-5}$, we have $\theta_{p,\mathrm{cr}} \approx 8.24 \times 10^{-4}$, which agrees with the numerical result very well. Using the above results at the critical point and Eq. (4.41), we obtain

$$\omega_{n,\mathrm{cr}} \approx \frac{\sqrt{3}}{2}\mu_{\mathrm{cr}}\sigma^{(0)}\theta_{p,\mathrm{cr}}. \tag{A.30}$$

We note that the behavior of the precession and nutation frequencies at the critical point as shown in Fig. 4.16 is unique to the IH. In contrast, both the precession and nutation frequencies increase smoothly with μ for the NH.

Appendix B

Supplemental Calculation for Neutrino Flavor Instability

B.1 Linearized Matrix and Characteristic Equation

Suppose now we have n NFIS's. By writing $(S_\perp, \theta, \vec{\theta}_i, \phi_s, \phi, \vec{\phi}_i) \equiv \mathbf{x} = \mathbf{x}_p + \boldsymbol{\xi} = \mathbf{x}_p + (\boldsymbol{\eta}, \boldsymbol{\zeta}) \equiv (S_{\perp p}, \theta_p, \vec{\theta}_{ip}, \phi_{sp}, \phi_p, \vec{\phi}_{ip}) + (\eta_s, \eta, \vec{\eta}_i, \zeta_s, \zeta, \vec{\zeta}_i)$, it's straightforward but tedious to show that the form $\dot{\boldsymbol{\xi}} = A(\mathbf{x}_p)\boldsymbol{\xi}$ of equation (4.103)-(4.108) become $\dot{\boldsymbol{\eta}} = A_1\boldsymbol{\zeta}$ and $\dot{\boldsymbol{\zeta}} = A_2\boldsymbol{\eta}$ with

$$A_1 = \begin{pmatrix} -Qs_pC - \sum_i q_i s_{ip} C_i & Qs_pC & q_3 s_{3p} C_3 & \cdots & q_n s_{np} C_n \\ \mu S_{\perp p} C & -\mu S_{\perp p} C & 0 & \cdots & 0 \\ \mu S_{\perp p} C_3 & 0 & -\mu S_{\perp p} C_3 & \cdots & 0 \\ \vdots & \vdots & \vdots & \vdots & \vdots \\ \mu S_{\perp p} C_n & 0 & 0 & \cdots & -\mu S_{\perp p} C_n \end{pmatrix}, \quad \text{(B.1)}$$

$$A_2 = \begin{pmatrix} \frac{Qs_pC+\sum_i q_i s_{ip} C_i}{S_{\perp p}^2} & -\frac{Qc_pC}{S_{\perp p}} & -\frac{q_3 c_{3p} C_3}{S_{\perp p}} & \cdots & -\frac{q_n c_{np} C_n}{S_{\perp p}} \\ -\frac{\mu c_p C}{s_p} & \frac{\mu S_{\perp p} C}{s_p^2} & 0 & \cdots & 0 \\ -\frac{\mu c_{3p} C_3}{s_{3p}} & 0 & \frac{\mu S_{\perp p} C_3}{s_{3p}^2} & \cdots & 0 \\ \vdots & \vdots & \vdots & \vdots & \vdots \\ -\frac{\mu c_{np} C_n}{s_{np}} & 0 & 0 & \cdots & \frac{\mu S_{\perp p} C_n}{s_{np}^2} \end{pmatrix}, \tag{B.2}$$

where s and c are abbreviations for $\sin\theta$ and $\cos\theta$ while the subscript p denotes the pure-precession solution given by equations (4.109)-(4.111).

Since A is block diagonalized with 0 in the diagonal blocks, its eigenvalues must be in the form of $\pm\lambda_i$ which implies that there is no damping solution. Furthermore, the special structure of A_1 results that there are two zero eigenvalues, which may corresponds to the existence of two conserved quantities of the system. As a result, we write the reduced characteristic equation (which exclude the two zero eigenvalues) of the linearized system in this form :

$$\sum_{i=0}^{n-1} a_i \lambda^{2i} = 0. \tag{B.3}$$

The roots of this equation can then tell us whether the n-NFIS system is stable or not around its pure-precession solutions.

B.2 Instability Critiria in Three-NFIS system

For a system with three NFIS's which are labeled by $\alpha_1 = 1$, $\gamma_1 = 1$, $\alpha_2 = a$, $\gamma_2 = -1$, $\alpha_3 = b$ and $\gamma_3 = \gamma > 1$, in the limit where $\mu \to \infty$ and $\theta_{\rm v} \to 0$, the reduced characteristic equation is :

$$\lambda^4 + \lambda^2 \frac{1}{S_\perp^2}\left(\frac{(\mu S_\perp^2 + dQ\theta^2)^2}{\theta^2} + 2q_3 Q\theta\theta_3 dd_3 + \frac{(\mu S_\perp^2 + d_3 q_3 \theta_3^2)^2}{\theta_3^2}\right) + \frac{\mu^2(\mu S_\perp^2 + dQ\theta^2 + d_3 q_3 \theta_3^2)^2}{\theta^2\theta_3^2} = 0, \tag{B.4}$$

where $d(d_3)$ equal 1 or -1 if $\cos\theta(\cos\theta_3) \approx 1$ or -1. Note that we use $CC_3 = dd_3$ in deriving the above equation.

If we consider zeroth-order terms which are proportional to μ^2 with $\theta \approx \theta_3 \approx -\frac{S_\perp}{S_z}$ only, this equation becomes $\lambda^4+\lambda^2 2\mu^2 S_z^2+\mu^4 S_z^4 = 0$. The discriminant Δ_3 ($\equiv b^2-4ac$ of $ax^2+bx+c=0$) of the quadratic equation of λ^2 is zero and $\lambda = \pm i\mu S_z = \pm i\omega_n(\mu \to \infty)$. Thus, we have to include the higher-order terms to see if Δ_3 is larger or smaller than 0. If $\Delta_3 > 0$, it only contributes a small correction to the zeroth-order solution and the stability of the system remains. However, if $\Delta_3 < 0$ in the leading-order such that $\lambda^2 \approx -\mu^2 S_z^2 \pm \frac{i}{2}\sqrt{|\Delta_3|}$, the positive real part of λ will drive the system to be unstable. The full expression of Δ_3 is

$$\begin{aligned}
\Delta_3 &= \frac{1}{S_\perp^4\theta^4\theta_3^4}[\mu^2 S_\perp^4(\theta-\theta_3)^2 + Q^2\theta^4\theta_3^2 + q_3^2\theta^2\theta_3^4 \\
&\quad -2\mu S_\perp^2\theta\theta_3(\theta-\theta_3)(dQ\theta - d_3q_3\theta_3) + 2q_3Q\theta^3\theta_3^3 dd_3] \\
&\times [\mu^2 S_\perp^4(\theta+\theta_3)^2 + Q^2\theta^4\theta_3^2 + q_3^2\theta^2\theta_3^4 + 2\mu S_\perp^2\theta\theta_3(\theta+\theta_3) \\
&\quad (dQ\theta + d_3q_3\theta_3) + 2q_3Q\theta^3\theta_3^3 dd_3]. \qquad \text{(B.5)}
\end{aligned}$$

From equation (B.5), one immediately sees that we have to keep the lowest order of $\theta - \theta_3 \approx \frac{\gamma S_\perp}{\mu S_z^2}$ inside the first brackets since it cancels out the μ dependence. Inside the second brackets, we can safely keep the term which is proportional to μ^2 only. After simplification, we derive

$$\begin{aligned}
\Delta_3 &\approx 4\mu^2[(Q+dd_3q_3)^2 + 2rS_z(dQ - d_3q_3) + r^2S_z^2] \qquad \text{(B.6)} \\
&= 4\mu^2[(dQ - d_3q_3 + rS_z)^2 + 4Qq_3dd_3]. \qquad \text{(B.7)}
\end{aligned}$$

It's clear that Δ_3 may become negative only when $dd_3 < 0$ which means that $\mathbf{r}$ and $\mathbf{r}_3$ must be anti-aligned. Note that the mass hierarchy doesn't affect the criterion of the stability since d, d_3 and S_z all change signs when the mass hierarchy changes.

We then replace Q, q_3, S_z in terms of the initial parameters a, b and γ to derive the general condition for the initial synchronized pure-precession to be unstable in a three-spin system as follows :

$$[a(\gamma-1)-2b]^2 - 2a(\gamma^2-1) - 4b(\gamma+1) + (\gamma+1)^2 < 0. \qquad \text{(B.8)}$$

Appendix C

Supplemental Calculation for Neutrino Oscillations in an 18 Solar Mass Supernova Model

C.1 Update of θ_{13}.

Recent measurement of $\bar{\nu}_e$ disappearance at Daya Bay shows the neutrino mixing angle $\sin^2 2\theta_{13} = 0.092 \pm 0.016 \pm 0.005$ [90]. This gives a central value $\theta_{13} = 0.152$ which is larger than the value we adopted in Chap. 5. We thus perform some additional simulations to investigate the effect of this change. The only significant change in the collective region is the local effective mixing angle before the flavor instability occurs as shown in the left panel of Fig. C.1. Before the instability, $\langle P_{\nu_e\nu_y} \rangle$ is proportional to $\sin^2 2\theta_{13}$ such that the case with larger θ_{13} has higher $\langle P_{\nu_e\nu_y} \rangle$. However, through the whole collective region, the matter density is still so high that the effective mixing angle only plays the role of providing the initial perturbation for instability to happen. Thus, the flavor instability occurs at the same place and the flavor evolution afterwards are not greatly influenced by this change of θ_{13}.

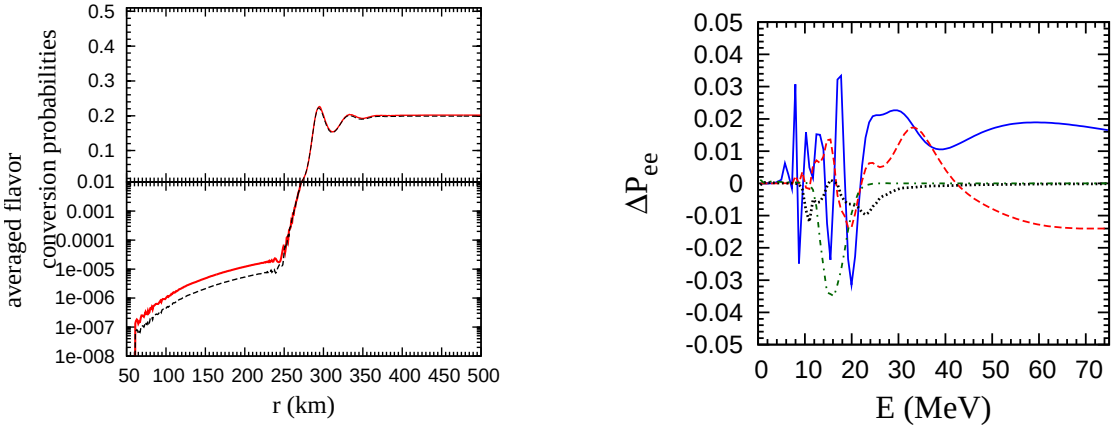

Figure C.1: Left panel : $\langle P_{\nu_e\nu_y} \rangle$ with $\theta_{13} = 0.152$ (red solid) and 0.1 (black dashed) for $t_{\rm pb} = 3.007$ second. Right panel : $\Delta P_{ee} \equiv \langle P_{\nu_e\nu_e} \rangle_v(\theta_{13} = 0.152) - \langle P_{\nu_e\nu_e} \rangle_v(\theta_{13} = 0.1)$ for $t_{\rm tv} = 1.025$ (blue solid), 1.401 (red dashed), 3.007 (black dotted) and 5.0 (green dashed-dotted) seconds at $r = 500$ km.

We also show in the right panel of Fig. C.1 the change of averaged survival probability of ν_e at $r = 500$ km for different $t_{\rm pb}$. There we can clearly see that the effects of this mixing angle are all smaller than 4%. Thus, our results of collective flavor oscillations are not influenced by the new constraint of θ_{13}.